National Science Foundation #ATM-9118963

EVOLUTION OF BALANCED FLOW IN A SIMULATED MESOSCALE CONVECTIVE COMPLEX

by Peter Q. Olsson

William R. Cotton, P.I.

Colorado State University

DEPARTMENT OF ATMOSPHERIC SCIENCE

PAPER NO. 570

EVOLUTION OF BALANCED FLOW IN A SIMULATED MESOSCALE CONVECTIVE COMPLEX

by

Peter Q. Olsson

Department of Atmospheric Science

Colorado State University

Fort Collins, C0 80523

Research Supported by

National Science Foundation

under Grant #ATM-9118963

November 28, 1994

Atmospheric Science Paper No. 570

ABSTRACT

EVOLUTION OF BALANCED FLOW IN A SIMULATED MESOSCALE CONVECTIVE COMPLEX

MCCs, a phenomenon occuring worldwide, by definition share certain structural and temporal features. Beyond the definition criteria, however, MCCs typically show a common organizational structure and evolution which cannot be directly attributed to the environment in which they evolve. This suggests that their evolution is governed by a set of physical laws which apply similarly to ensemble convective heating in a variety of mesoscale environments.

In the middle latitudes, MCCs represent the extreme case of a large-amplitude energetic perturbation to the background environment. While substantial transients and observed, a separate class of non-radiating, balanced motions also evolve. These motions, and the altered thermal structure which balances them, are conveniently contained in a single quantity, the PV.

The work described herein is an effort to understand the evolution of these balanced motions. To this end, a primitive equation (PE) numerical simulation of an MCC was performed. To isolate the balanced flow, a diagnostic system based on nonlinear balance is derived and discussed. This system is used to invert the PV and recover the rotational component of the balanced motion and the balanced mass field. A further application of the NLB approximation results in a diagnostic equation for the vertical velocity and, as well, a method for diagnosing the horizontal divergent motions which are "slaved" to it by the constraint of continuity.

The PE simulation discussed herein agrees well with observations and produces many of the features frequently associated with MCCs including mesoscale convectively-induced vortices in the lower troposphere and a large anticyclone at upper levels. The nondivergent component of the PE model winds is found to consist, to a great degree, of balanced flow. More surprisingly, the storm-induced divergent model winds also remain reasonably balanced, though certainly less so than the nondivergent flow. The good agreement between model and balanced upward vertical mass flux suggests that the bulk of the three-dimensional unbalanced divergent motion may be attributed to gravity waves. The greatest disparity between the model and balanced circulations is found in the downward vertical motion, suggesting that the process of mass adjustment due to convective heating is largely dominated by unbalanced fast-manifold processes.

Peter Quentin Olsson
Department of Atmospheric Science
Fort Collins, CO 80523
Spring 1995

ACKNOWLEDGEMENTS

Any task of such a scope as a dissertation necessarily involves the efforts of several people beyond the author. While some of these persons are destined to anonymity, I would like to acknowledge several individuals for their direct and indirect contributions to this mammoth task.

Firstly, I would like to thank my advisor, Dr. William R. Cotton, for his support, faith and encouragement during the several years required to bring this project to fruition. Similarly, my committee members, Dr. Michael Montgomery and Dr. Wayne Schubert are thanked for generously sharing their extensive knowledge of balanced dynamics, both in the classroom and in illuminating discussions *in camera.* I would also like to thank Dr. Robert Walko for his invaluable assistance in using and modifying the RAMS model, and for the several lengthy discussions and thorough explanations of the physics upon which the model is based. Similarly, I thank Dr. Michael Weissbluth for his help and advice in the use of the cumulus parameterization of his designing. I also thank Rolf Hertenstein for the several conversations and discussions of meteorological nature we have had through the years, especially those concerning potential vorticity and its relationship to mesoscale convection. Appreciation is extended to Scott Randell and Michael Meyers for their input at various times during the preparation of this manuscript, and to Donna Chester for keeping the computing machinery up and running.

I would like to acknowledge two persons involved in my earlier university education, Dr. George Tuthill and Dr. Richard T. Robiscoe of the Physics Department at Montana State University, for their significant contributions to my education as a mathematician and a scientist, and for their encouragement to pursue a career in scientific research.

Finally I would like to thank those persons who supported me emotionally, spiritually and financially during my tenure as a graduate student: Cynthia Rakowski, my children Kirsten and Wolfgang, and last and most importantly, my cherished wife Ute.

This research was funded by the National Science Foundation under grant ATM-9118963.

TABLE OF CONTENTS

Chapter 1: Introduction

"... [W]e might say that the atmosphere is a musical instrument on which one can play many tunes. High notes are sound waves, low notes are long inertial waves, and nature is a musician more of the Beethoven than of the Chopin type. He much prefers the low notes and only occasionally plays arpeggios in a treble and then only with a light hand. The oceans and the continents are the elephants in Saint-Seans' Animal Suite, marching slow cumbrous rhythm, one step every day or so. Of course there are overtones; sound waves, billow clouds (gravity waves), inertial oscillations; but these are [relatively] unimportant..."

- Jule Charney 1947

1.1 Introduction

The above quotation appeared in a letter from Jule Charney to Phillip Duncan Thompson (Thompson 1983) in support of Charney's position in an ongoing debate between the two scientists regarding initialization problems with early numerical weather prediction models. Charney's point was that the atmosphere is, to a large degree, a gently forced system and that the "overtones" are merely noise, which confuses, as Charney puts it, "the true music of the atmosphere." The primitive equations (PE), upon which many numerical models are based, allow for all these overtones. The problem which perplexed Charney and Thompson was this: How to start the symphony (initialize the model) without exciting too much noise (overtones) in the later movements? As we have since found out, our understanding of these high frequency and low frequency aspects of the atmosphere have significance well beyond the initialization of operational forecast models.

Placed in the more modern context of atmospheric science in the 1990s, Charney might refer to the slowly evolving atmosphere "composed in the Beethoven style" as being balanced, in contrast to the turbulent, rapidly changing elements therein, "having the Chopin style", as being unbalanced. It would be interesting to hear from Charney how he would characterize the mesoscale convective complex (MCC) in this musical allegory. Later in his letter to Thompson, Charney states:

> ... [T]he energy that goes into an atmospheric disturbance depends on the initial mode of excitation. A forced perturbation of long period produces a disturbance of long period.

While the cloud-scale elements which produce an MCC (i.e., individual convective cells) are of the timescale of several minutes (Cotton and Anthes 1989) the larger, mesoscale effect of perhaps hundreds of such transient contiguous events, recurring for several hours over an area of a several thousand square kilometers certainly constitutes a significant "forced perturbation of long period".

Several studies of gravity waves forced by deep convection on the cloud scale (e.g. Bretherton and Smolarkiewicz 1989; Nicholls et al. 1991) and on the mesoscale (Mapes 1993; Nicholls et al. 1991) demonstrate the importance of gravity waves in maintaining mass balance between convective updrafts and the compensating subsidence. In some circumstances, (e.g. an atmosphere at rest) these waves may effectively radiate away a significant amount of the energy perturbation. In a background state of positive relative vorticity, the same diabatic heating can result in a more balanced vortical flow (Schubert et al. 1980). Observational evidence indicates that in several cases, long-lived mesoscale vortices are associated with the MCCs, particularly at mid-latitudes (Menard and Fritsch 1989; Brandes 1990; Bartels and Maddox 1991; Johnson and Bartels 1992; Fritsch et al. 1994). Perhaps Charney would agree that the MCC is in the style of Rachmaninoff: a substantial measure each of the treble and the base. The higher frequency gravity waves, while definitely in evidence, typically do not contribute directly to the longevity and intensity of the MCC (Jiang and Raymond 1994), though two dimensional modeling studies (Tripoli and Cotton 1989) have indicated gravity waves may play a more central role in some cases. It is the low frequency bass which seems to be most related to the mesoscale organization of the MCC and that component which leaves the lasting impression on the atmosphere. This balanced, lower frequency or slow manifold component of the MCC is the focus of this dissertation.

1.2 Common Characteristics of the MCC/MCS

Since Maddox (1980) first defined the MCC, much research has been focused on both observational studies and numerical simulations of MCCs and other smaller, yet dynamically similar Mesoscale Convective Systems (MCSs). See Table 1.1 for a summary of the criteria used to define the MCC[1]. These organized convective systems are seen worldwide, but there do seem to be preferred locations. Recent surveys, based mostly on satellite data, show that large populations of MCCs are favored in the central plains of the United States (Maddox 1980; Augustine and Howard 1988, 1991), the central plains of South America (Velasco and Fritsch 1987), central Africa (Laing and Fritsch 1993a), the central Indian subcontinent, (Laing and Fritsch 1993b) and China (Miller and Fritsch 1991). From the above mentioned studies of MCC climatology, a picture of the favored MCC environment has emerged:

- MCCs tend to develop over land, or near (within about 250 km) a continental land mass.
- MCCs most frequently develop to the lee (in the sense of the predominant mid-tropospheric flow) of significant mountain ranges. For example, favored locations are to the lee of the Rocky Mountains in N. America, east of the Andes in S. America (Velasco and Fritsch 1987), west of the N. African mountains in the Sahel, east of the South African escarpment (Laing and Fritsch 1993a), and to the east of the Himalayan Massif (Miller and Fritsch 1991).

---

1 It should be apparent from perusing the definitions given in Table 1.1 that the MCC definition is rather ad hoc, as it is based on appearance from satellite imagery and lacks a more dynamically based definition. In this dissertation the term MCC will be used rather more loosely, to include MCSs whose behavior resembles that of the MCC but which might not exactly satisfy the duration or size criteria specified in Table 1.1. The term mesoscale convective system does not have a rigorous definition. Zipser (1982) defines the MCS as a cloud and precipitation system that includes a group of cumulonimbus clouds during most of its lifetime.

Criteria	Description
Minimum Size	Continuous cold cloud shield (IR temperature ≤ 52°C) must have an area ≥ 50,000 km^2
Duration	Minimum size definition must be met or exceeded for a period ≥ 6 h.
Shape	Minor axis/major axis ≥ 0.7 at time of maximum areal extent of the -52° C continuous cloud shield.
Definitions:	
First storms	When the initial storms of the MCC first appear on the satellite imagery.
Initiation	Time when minimum size criterion is first realized.
Termination	First time when minimum size criterion is no longer satisfied.
Maximum extent	Time when the continuous cold cloud shield (IR temperature ≤ 52°C) is at its maximum size.

Table 1.1. *Mesoscale convective complex criteria and definitions (from Augustine and Howard 1991)*

- MCCs most frequently occur under, or along the periphery of a synoptic scale mid-tropospheric ridge (Maddox 1983; Velasco and Fritsch 1987; Augustine and Howard 1991).
- Strong low-level thermodynamic forcing (positive advection of equivalent potential temperature, θ_e), usually in the form of a poleward flowing low-level jet (LLJ), is frequently present in the MCC growth region (Maddox 1983; Velasco and Fritsch 1987; Cotton et al. 1989; Augustine and Howard 1991).
- The favored MCC region seems to migrate poleward during the warm season, often accompanying the poleward migration of the jet stream (Augustine and Howard 1988, 1991; Laing and Fritsch 1993a; Maddox 1983). It is interesting to note that the end of the MCC season in most regions occurs at the most poleward location. That is, the favored location does not seem to move southward with the jet during the latter part of the warm season. Also, tropical regions do not see a significant migration in the favored location, probably because the seasonal insolation does not vary significantly.
- The ripe MCC environment generally has large values of convective available potential energy (CAPE) in excess of 10^3 J kg^{-1}(Maddox 1983; Cotton et al. 1989).

- The favored MCC environment is one which has, climatologically, a low albedo, i.e., a relatively cloud free region (Velasco and Fritsch 1987).
- MCCs, especially over the Great Plains of the United States tend to occur in a precursor region of mesoscale convergence and upward motion (Maddox 1983; Cotton et al. 1989).

A worthy point to note is that several geographical regions which tend to experience very frequent deep convection are not necessarily likely spots for MCC generation. For example, the rain forests of the Amazon Basin, and the Gulf of Thailand have widespread convection and yet experience small populations of MCCs (Velasco and Fritsch 1987, Laing and Fritsch 1993b). This would indicate that the MCC is not just the chance occurrence of clustered convection, but more a distinct and organized mesoscale system.

Composite climatological studies of MCCs in the U.S. have also been undertaken (Maddox 1983; Cotton et al. 1989; Augustine and Howard 1991) and show many of the same features already discussed. The presence of a mean short-wave trough was seen by Maddox (1983) in his composite of 10 storms, though this feature was not found by Cotton et al. This may be because Cotton et al. sampled only storms occuring in the months of June, July, and August, specifically to minimize the effects of transient baroclinic forcing. Also, a considerably larger sample size (90 cases) was used and most likely resulted in the filtering of smaller wavelength features.

The climatological and composite studies have also led to a common picture of the behavior of the MCC as a storm system. The following features are noted:

- The storm duration tends to be between 9 and 12 hours. MCCs in central South America tend to be somewhat larger and longer lived than in other midlatitude locations (Velasco and Fritsch 1987).
- The first thunderstorms which may be attributed to the development of the MCC occur in the late afternoon, near the end of the diurnal heating cycle. Thus, the MCC itself tends to be predominantly, though certainly not exclusively, a nocturnal phenomenon.
- In favored MCC regions a significant percentage of warm season precipitation derives from nocturnal MCCs (Bleeker and Andre 1951).

- The storm tracks of MCC centroids tend to have an anticyclonic curvature, most likely due to their favored location on the periphery of a broad ridge (Velasco and Fritsch 1987; Augustine and Howard 1988, 1991).
- MCCs tend to have some component of motion along the gradient of the low level θ_e (Laing and Fritsch 1993b, Merritt and Fritsch 1984) and often have strong low-level warm advection (Maddox 1983; Wetzel et al. 1983)

One of the main actions of deep convection is to transport mass vertically. While the upward transport occurs locally, the compensating subsidence generally occurs over a much greater region (Mapes 1993). One of the most noticeable features in the mature to dissipating MCC is the huge divergent outflow anvil. Cotton et al. (1989) found that the region of detrainment near the tropopause displayed increasingly larger values of integrated divergence as the storm matured and dissipated. Maddox (1983) found a similar collective divergence tendency in the MCC environment during the mature and dissipating stages, with average large scale divergence values greater than $5 \times 10^{-5}\ s^{-1}$ at 200 mb.

The water substance detrained from the cloud at this near tropopause level of maximum divergence tends to remain in the upper atmosphere for extended periods (Bosart and Sanders 1981). Since its source is typically the boundary layer, the MCC acts as an efficient agent in moistening a large region of neighboring upper troposphere and in readjusting the θ_e profile (McAnelly and Cotton 1989). Remnant cirrus clouds can be tracked coherently for several days following their generation in an MCC (Wetzel et al. 1983; Fritsch et al. 1994).

The great size of MCCs would suggest that the effect on the surrounding larger scale environment could be substantial. As noted by Laing and Fritsch (1993b) the preferred nocturnal occurrence of MCCs provides a special impact on the radiation budget. The optically thick stratus anvils of MCCs have a much different long-wave radiative signature than the more cirrus-like anvil remnants of daytime convection (Stephens and Webster 1980). The substantial and widespread rainfall associated MCCs (McAnelly and Cotton 1986, 1989; Kane et al. 1987) dramatically alters surface conditions. The resulting gradients in soil moisture can lead to the generation of significant mesoscale boundary layer circulations (Segal and Arrit 1992), providing a focusing mechanism for future convective systems.

1.3 Gross Circulation Features of the MCC

The MCC may also alter the dynamical environment of the larger scale circulation in which it is embedded. One of the more striking features present in many MCC case studies is the existence of a mesoscale convective vortex (MCV) (e.g. Leary and Rappaport 1987; Zhang and Fritsch 1988; Menard and Fritsch 1989; Brandes 1990; Johnson and Bartels 1992; Fritsch et al. 1994), usually observed in the mature-to-decaying MCC or MCS.

In the Doppler radar study by Johnson and Bartels (1992), an MCV was observed in the mature stage to dissipating stages of a rather small MCS. This MCV extended from 3.5 km to 8 km above ground level (AGL) and was about 100 km across. Brandes (1990), using a data set composited from rawinsonde and Doppler radar measurements, observed the generation of an MCV which developed at about 3 km AGL during the mature stage of an MCS and evolved in the dissipating stages into a closed circulation extending from the surface to approximately 6 km AGL. Doppler-radar-derived relative vorticity measurements performed in the mature stage of this MCS found values greater than 15 times the local planetary vorticity. This case was somewhat unusual in that the MCV was very long-lived, being first observed during the earlier stages of upscale growth of the parent MCS. Fritsch et al. (1994) document the existence of an extraordinarily long-lived MCV. This vortex was apparently generated by an MCS which formed just east of the Rocky Mountains. The storm was tracked over a period of 3 days and during this period the mesoscale convective activity associated with the MCV experienced 5 discrete cycles of regeneration and decay.

Bartels and Maddox (1991) examined satellite images over the United States for the period 1981-1988 to obtain a climatology of MCVs discernible from satellite information alone. They were able to positively identify 20 MCVs out of the population of storms examined. This is a relatively small percentage (about 5%) of the storm population, but the presence of some form of MCV might be more ubiquitous than this study indicates. The cloud signature of an MCV at mid-levels might be obscured by higher level convective anvil debris. Also, the remnant vorticial circulation might be extant in a cloud-free environment, rendering it unobservable from satellite imagery. (For example, the MCV documented by Doppler radar in Johnson and Bartels 1992, was not identified in the satellite study of Bartels and Maddox.) Bartels and Maddox found that the parent storms of MCVs found in their studies, while all having a quasi-circular cloud shields, showed significant diversity in longevity, size and cloud top thermal structure.

Some authors state that the MCV is in some sense an inherent part of the MCC circulation. For example, Velasco and Fritsch (1987) hypothesize:

> "... The development (to varying degrees) of a latent-heat-driven, mesoscale warm-core vortex... may very well be the feature which makes an MCC an MCC."

In Menard and Fritsch (1989), the authors state in their introduction:

> "Growing evidence suggests that MCCs exhibit three principal forms of mesoα-scale circulations: 1) an upper tropospheric cold core anticyclone,; 2) *a midlevel warm core tropospheric vortex and;* 3) a lower tropospheric outflow occasionally with a trailing mesolow." (emphasis mine)

While these case studies indicate a long-lived vortex at mid-levels, and large values of cyclonic vorticity *do* seem to be a ubiquitous feature of MCCs, it appears that the existence of a *vortex* (as opposed to a flow with large cyclonic vorticity) probably exists in only a subset of the MCC population. Fortune et al. (1992) made a case study of MCCs which had a wave-cyclone type of cloud-shield appearance. They examined many hours of radar data during the mature and dissipating stages of several MCCs (the period in which the MCV has been most frequently documented) but did not find closed cyclonic circulations in these cases. The lack of radar coverage documenting the internal circulations of a significant number of MCCs throughout their entire life-cycles, and in particular their mature and dissipating stages, makes it difficult to ascertain just what percentage of these storms *did not* posses a significant closed cyclonic circulation. There is certainly strong evidence that midlevel cyclonic vorticity is enhanced in most MCCs (Cotton et al. 1989). The mechanisms by which this occurs will be investigated in greater detail in subsequent chapters.

It is likely that certain conditions favor the development of the MCV. Menard and Fritsch (1989), and Fritsch et al. (1994) note that weak vertical shear in the middle troposphere, commonly the case in the large scale MCC environment, is required to maintain a coherent vortex structure for a significant period of time. Johnson and Bartels (1992) indicate that in their study, the development of the MCV was linked to the passage of a propagating shortwave trough, but note that this mechanism may not be essential to MCV production.

As seen in the above quote by Menard and Fritsch, another significant dynamic feature of the MCC is an upper level cold anticyclonic circulation. Johnson and Bartels (1992) noted a pronounced change from cyclonic to anticyclonic vorticity with height in their case with the vorticity becoming anticyclonic above 10 km AGL. Brandes (1990), in his study of the MCV-bearing MCS observed a sharp transition to anticyclonic vorticity and divergent flow at about 8 km AGL. Cotton et al. (1989) saw a net decrease in composite vorticity at upper levels (above about 400 mb) with a sharp minimum (maximum in *anticyclonic* vorticity) developing at about 200 mb. This feature is best documented in the United States population of MCCs, as upper atmospheric soundings for other MCC-favored regions (e.g. South America, Africa, and India) are either too infrequent and widely spaced to permit adequate sampling, or are not archived for the periods in which MCC climatologies have been compiled. It seems reasonable to assume that this upper tropospheric vorticity minimum is a feature common to most MCCs worldwide. The origins of this feature will be discussed from the PV standpoint in Chapter 2.

In addition to the midlatitude cases discussed above, climatological studies indicate that MCCs also occur in the lower latitudes. Velasco and Fritsch (1987) found 115 tropical MCCs in their 2 year study of MCCs in the Americas. These storms tended to have shorter lifetimes, but showed the midlatitude nocturnal bias and seasonal correlation between daily insolation and likelihood of occurrence. Velasco and Fritsch concluded that tropical MCCs are about as common as higher latitude MCCs, at least in the Americas. In their study of MCCs in the Western Pacific, Miller and Fritsch (1991) found that, unlike the midlatitude population, the seasonal distribution of the low-latitude MCCs in their study period had a less distinct maximum near the summer solstice; the distribution being more uniform throughout the warm season. Though the region in which this study was conducted was mostly oceanic and quite active convectively, Miller and Fritsch commented that over 80% of the MCCs observed had their genesis either over or within 250 km of a significant land mass.

Maddox (1983) found several similarities between his composite midlatitude MCC and observations from tropical cloud clusters (e.g. Riehl et al. 1973), mentioning the similarity in divergence profiles between the mature MCC and the developing tropical supercluster which also had a similar mid- and upper-tropospheric vertical thermal structure: warm core from 500mb to 250 mb, and cold core above. The storms also had apparently similar environments, namely, a weak vertical shear above the boundary layer and very little positive vorticity advection. Wetzel et. al (1983), in their case study of an MCC outbreak involving several storms, compared their cases to the tropical storm study of McBride and Zehr (1981) and also found several similarities in the divergence and temperature perturbation profiles.

Cotton et al. (1989) however, stressed several differences between their findings and those from the tropical convective cluster observations of Tollerud and Esbensen (1985). They observed a much deeper convergent layer and more persistent upper level divergence in the midlatitude composite. They also found significant differences in the evolution of the vorticity fields. The midlatitude composite exhibited a trend towards increasing midlevel vorticity throughout the life cycle whereas the GATE tropical cloud clusters of Tollerud and Esbensen showed a significant decrease in vorticity near 700 mb in the dissipating stage. In light of the preceding discussion of MCVs, this may provide evidence that while appearances are similar between tropical and midlatitude MCCs, the governing dynamics might not be so similar. It should be noted however, that Tollerud and Esbensen had used different criteria in selecting their storm population, and hence included some storms smaller that those studied by Cotton et al. (1989).

Velasco and Fritsch (1987) also discuss the possibility that the tropical MCC may not be dynamically similar to the higher latitude MCC. They state:

> "... [T]hough the MCCs at very low latitudes fulfill the satellite definition requirements, their cold cloud shields are often qualitatively different from systems at higher latitudes. Specifically they exhibit more irregularities in their shape and give the visual impression that they are more like an agglomeration of big thunderstorms than a well-organized nearly symmetric mesoscale circulation."

Obviously, these tropical MCC type storms exist in a background environment of weak planetary vorticity and the convergence of vorticity filaments by the convergent low-level inflow will be concomitantly smaller. The importance of this vorticity convergence will be seen in the later discussion of the balanced dynamics of MCCs.

Whether or not the midlatitude and tropical MCCs are dynamically similar, the tropical MCC does have a dynamic impact on its larger scale environment. Velasco and Fritsch observed that MCCs in tropical regions may propagate into favorable genesis regions and develop into more intense tropical storms. Of the 114 low latitude MCCs in their study, 5 developed into named tropical storms during the 2 year period. Laing and Fritsch (1993b) mentioned that a few MCCs originating over the Indian subcontinent developed into tropical depressions over the Arabian Sea and Bay of Bengal. Similarly, Laing and Fritsch

(1993a) saw three continental West African MCCs develop into tropical cyclones over the eastern Atlantic Ocean.

An MCV generated within an MCC has been suggested (Fritsch et al. 1994) as a mechanism to enhance tropical cyclogenesis. Building on the concept of a tropical cyclone as a Carnot engine (Emanuel 1986; Rotunno and Emanuel 1987), Fritsch et al. argue that a pre-existing MCV can provide the trigger or "starter vortex" necessary to exceed a threshold level of ocean/air surface energy transfer. Once started, this surface energy flux can result in vortex amplification, resulting in a deepening tropical cyclone. In addition to enhancing the surface energy transfer, the MCV has a warm core structure similar to that of a tropical cyclone and provides an enhanced inertial stability which makes the diabatic heating more efficient at producing balanced, rotational flow (see Chapter 2).

1.4 Are MCCs Balanced Systems?

The foregoing discussion has been presented in support of the hypothesis that the MCC is a distinct type of storm which is ubiquitous to several regions of the world, with a characteristic environment, behavior and life-cycle. While some authors have observed some form of middle or upper tropospheric shortwave or baroclinic forcing in association their case studies (Leary and Rappaport 1987; Johnson and Bartels 1992), others (Cotton et al. 1983, Wetzel et al. 1983) have seen MCC development without any apparent shortwave interaction.

It is likely that a significant percentage of MCCs are associated, *in some manner*, with weak large scale forcing. This interaction may play a peripheral or secondary role, for example providing the initial focusing of convection along shallow surface cold fronts (Wetzel et al. 1983) or along drylines (Johnson et al. 1989), providing mesoscale lifting/ convergence and sustaining low-level θ_e advection (Maddox 1983); all actions which can initiate and maintain deep convection. Since it is absent in several cases, *large scale mid-*

and upper tropospheric forcing is evidently not an essential ingredient in the creation and maintenance of the MCC as a distinct mesoscale circulation.[2]

Wetzel et al. (1983) and Maddox (1983) found that MCCs do not achieve a significant amount of latitudinal thermal advection and hence do not act to decrease a temperature gradient. In fact, Wetzel et al. found a weak up-gradient storm-driven thermal transport. Most large-scale dynamic theories for disturbance growth (e.g. baroclinic instability) gain energy at the expense of decreasing gradients in the mean environment. The favored environment for MCCs, however, has almost no significant gradient of any consequential dynamic quantity, further suggesting that large scale dynamic processes or instabilities are not essential to the organization of the MCC. Wetzel et al. hypothesize that significant baroclinicity may instead produce a more linear or squall line type of mesoscale convective storm structure. Fritsch et al. (1994) observed an MCV which went through several convective regeneration periods and spawned numerous MCSs. They found an almost vertical warm core structure to the vortex, in contrast to baroclinic systems which have a significant tilt.

The driving force for the MCC seems to be conditional instability, with CAPE (Moncrieff and Miller 1976) the energy reservoir being tapped and released (Fritsch et al. 1994). The lack of significant external forcing indicates that the storm to some degree "organizes itself". The ensemble energy release, on the thunderstorm scale, of hundreds of convective cells is used by the incipient MCC to organize mesoscale flows which can enhance further latent heat release (in the stratiform anvil) and contain energy which would, on a smaller dynamic scale, be dispersed as gravity waves. Thus the MCC acts as a "balanced system" in the same sense as a hurricane or extra-tropical cyclone and evolves, to a large degree, in

2 This balanced forcing may, however, play a crucial development in *some* of the features noted in particular MCC events, in particular MCVs, tornados, (Augustine and Howard 1988, 1991), and derechos (Johns and Hirt 1987).

accordance with an approximated subset of the primitive equations which excludes fast-manifold (propagating gravity wave) behavior.

The next chapter will discuss the historic and current thinking about MCCs as balanced systems and consider MCC evolution in the potential vorticity framework.

Chapter 2: MCCs, Balanced Models and PV

2.1 A Dynamical Definition of the MCC

In the preceding chapter, the term "mesoscale convective complex" was defined from its appearance and duration on IR satellite images (see Table 1.1). Not surprisingly, this definition, while easily applied in identifying MCCs from past and current satellite image archives, is inadequate in identifying the unique characteristics that may dynamically define the MCC. One problem with the current, and fairly arbitrary, definition is that storms slightly smaller or of less duration, but dynamically similar, to MCCs are excluded from climatologies and composite studies.

Cotton et al. (1989) proposed a dynamic definition based on a Rossby radius argument using a form of the Rossby radius (Schubert and Hack 1982; Frank 1983) which accounts for locally enhanced vorticity (for example in an MCV):

$$\lambda_R = \frac{C_N}{(\zeta + f)^{1/2}(2VR^{-1} + f)^{1/2}} \tag{2.1}$$

where ζ is the relative vorticity, V the tangential velocity at some radius R, f the coriolis parameter, and C_N the phase speed of the Nth mode pure gravity wave. The quantity in the denominator of (2.1) is the square root of the inertial stability parameter (Schubert and Hack 1982). For systems smaller than λ_R, the energy (here in the form of CAPE) released in the deep convection excites gravity waves, which effectively radiate energy from the system. For systems larger than λ_R, more of the released energy is confined locally to within the MCS, and is projected into the rotational flow.

Ooyama (1982), offers a complementary interpretation of the Rossby radius, as follows: motions which have a scale greater than λ_R are quasi-horizontal and are nearly in geostrophic balance. The vertical motion which does occur is that secondary circulation required to adjust from one horizontal balanced state to another. By contrast, motions whose scale is less than λ_R are more three-dimensional and are not balanced with the pressure field. These two regimes are often referred to as geostrophic, (two-dimensional) and three-dimensional turbulence, respectively (Tennekes 1978). Geostrophic turbulence operates under an important constraint: kinetic energy cascade into smaller scales is largely prohibited. In three-dimensional turbulence (scales $< \lambda_R$), energy rapidly cascades to smaller scales. Because of this, one would expect disturbances operating in the two differing regimes to evolve quite differently.

As discussed in Chapter 1, a defining feature of MCCs is the development of a strong positive vorticity maximum in the lower and middle troposphere. Thus, Cotton et al. (1989) argue, as the MCC matures and develops this maximum, it achieves a state of greater inertial stability, enhancing the stability parameter, and hence, decreasing λ_R. This implies that during its evolution, the MCC (at least in some cases) passes from a state of three-dimensional turbulence (an ensemble of fully three-dimensional turbulent convective elements) to a state of geostrophic turbulence where energy is trapped in the larger scales. Here the vertical motion fields and associated secondary horizontal divergent circulations are those which maintain the balanced primary circulations. The inertial stability thus becomes the horizontal analog of the static stability. It provides a measure of the horizontal restoring force resisting lateral displacements, as the static stability provides a measure of the force resisting displacements in the vertical. The enhanced inertial stability is often referred to as "stiffening" (Ooyama 1982; Schubert and Hack 1982) since the inertial stability is analogous to Hooke's spring constant: larger values acting like stiffer springs.

This argument is supported by the findings of Schubert et al. (1980). Using a linearized axisymmetric vortex model, they found that convective-type heating in a basic state with no relative vorticity produced a response dominated by inertia-gravity waves, with very little energy going into the rotational spectrum of modes. When the basic state was one in which the inner region had positive relative vorticity, and hence a greater inertial stability, the heating became much more efficient in producing a balanced vorticial flow. In the former case, energy was radiated away, whereas in the latter case the energy was confined to the storm scale circulations. Schubert and Hack (1982), again using an axisymmetric model, showed that increasing the inertial stability in the presence of convective heating results in a decrease in the strength of the forced secondary circulation. This is consistent with a mature MCC, which is characterized by more slantwise flow branches and stratiform precipitation, rather than the more upright cumulus convection seen in the genesis stage.

Clearly, inertial stability provides a tremendously important constraint on the motions excited in the atmosphere as a response to thermal forcing. Unfortunately, the theoretical studies just mentioned used idealized geometries (i.e., axisymmetry) and other approximations and simplifications such as ideal vortex structure and linearization which may lead to analytic solutions, but whose applicability to the fully three-dimensional MCC is not well defined. Many, if not most MCCs have a linear structure in the leading edge of the convection. Several studies (e.g., Leary and Rappaport 1987; Johnson et al 1990; Fortune et al. 1992; Nachamkin et al. 1994) have observed circulations internal to the MCC which were clearly not radially symmetric. Those systems which contain MCVs are more appropriate candidates for this type of analysis, but these appear to be only a special subset of the MCC population. Regrettably, no fully three-dimensional theory of inertial stability exists for the general case. Nonetheless, enhanced local rotational effects are certainly important and will be considered in greater detail in later chapters.

To apply (2.1) to their composite MCC, Cotton et al. (1989), lacking an obvious choice for the radius of curvature, chose R to be ~320 km, corresponding to the radius of the cloud shield with temperature $\leq$ -30°C. Another problem arises in specifying the appropriate gravity-inertia phase speed, C_N, to use in this calculation, since the Brunt-Väisälä frequency shows considerable temporal and spatial variation. Also, the subscript N refers to the vertical mode of the wave, with a separate phase speed and hence seperate λ_R for each vertical mode. This phase speed can vary from ~3 $\rightarrow$ 300 m s^{-1} (Schubert et al. 1980), giving a wide range of values for the different λ_R. Cotton et al. chose a value of 30 m s^{-1} based on results of a two-dimensional simulation by Tripoli and Cotton (1989). Using these values at a latitude of 40°, they computed λ_R = 300 km for the composite MCC. This λ_R was slightly smaller than their cloud shield radius R, of about 320 km. They also found that the computed value varied by less than 4% over the lifetime of the storm, concluding that the inertial stability of midlatitude MCCs is dominated by the coriolis parameter, f. (This result would probably not be expected in an MCV-bearing MCC). These results lead to the following dynamically-based definition for an MCC:

> "A mature MCC represents an inertially stable mesoscale convective system which is nearly geostrophically balanced and whose horizontal scale is comparable to or greater than λ_R."

In support of this definition, Cotton et al. cite observational studies (e.g., McAnelly and Cotton 1986, 1989) showing that as it matures, the system becomes less divergent and the vertical motion less pronounced. This is in agreement with Ooyama's (1982) reasoning that the balanced dynamically large system is more characteristically two-dimensional. Other researchers have found similar values for the Rossby radius (e.g., Johnson and Bartels 1992).

The result of Cotton et al. might be somewhat biased by the use of poorly resolved data and composited data in the calculations. For example, they found a maximum composite value for ζ of about 10^{-5} s^{-1} in their study (see their Fig. 16). Other individual case studies have found much larger values of relative vorticity. Johnson and Bartels (1992), using an averaging area of about 100 km^2, found a average value of $\zeta \sim 10^{-4}\ s^{-1}$, giving an absolute vorticity twice as large as the local coriolis parameter.

Chen and Frank (1993) demonstrate another manner in which λ_R may be reduced, namely by reducing the numerator in (2.1). To see how this happens, it is illustrative to rewrite the numerator replacing the phase speed C_N, with the product of the Brunt-Väisälä frequency N, which obeys:

$$N^2 = g\frac{\partial ln\theta}{\partial z} = \frac{g}{T}\left(\frac{dT}{dz} + \Gamma_d\right), \qquad \textbf{(2.2)}$$

and a suitable scale height, that is $C_N \rightarrow NH$ (Frank 1983). Γ_d in (2.2) represents the dry adiabatic lapse rate.

Now, since $\lambda_R \propto N$, it is apparent that reducing the static stability N, decreases λ_R. Chen and Frank hypothesized that in a saturated environment, the moist Brunt-Väisälä frequency, N_m,

$$N_m^2 = g\frac{\partial ln\theta_e}{\partial z} = \frac{g}{T}\left(\frac{dT}{dz} + \Gamma_m\right) \qquad \textbf{(2.3)}$$

pertains (Durran and Klemp 1982), and therefore the Rossby radius will have a smaller value. This arises because Γ_m, the moist or saturated (pseudo-)adiabatic lapse rate in (2.3) is significantly smaller than Γ_d in (2.2) which represents the dry or unsaturated adiabatic lapse rate. Also, $\partial T/\partial z$ tends to be smaller in the saturated environment.

Using a primitive equation (PE) model to simulate an idealized MCV, they found that the value of Brunt-Väisälä frequency decreased by a factor of 2 when computed in a saturated, rather than dry, atmosphere. Using a value of $\zeta = 2f$ for an average relative vorticity, and a tangential wind of 10 m s^{-1} at R = 100 km, they calculated a value of 47 km for λ_R, compared to a pre-MCC value of 277 km in the surrounding environment.

This result has questionable applicability to the real MCC however, because the initial conditions were highly biased towards MCV formation. In particular, the initial parameterized convection was co-located with a very strong short-wave in the middle troposphere with positive relative vorticity extending to the surface. This is in sharp contrast to Cotton et al. (1989) who found that the composite large scale MCC environment was largely barotropic with a background of anticyclonic vorticity. Also, the initial cumulus forcing in this experiment, a straight and uniform convective line 300 km long, was on a scale much larger than that experienced by most incipient MCCs. (Recall that the environmental Rossby radius was 288 km, indicating that the initial forcing was on a balanced scale.) Still, they did demonstrate that, at least in this idealized case, MCC-induced dynamic Rossby radius contraction can occur.

2.2 Balanced Models and the Concept of Balance

Considering the attention which has been focused on MCSs, both observationally and from the modeling standpoint, it is somewhat surprising that so little attention has been given to these phenomena in the context of balanced weather systems. This is perhaps because convective systems have traditionally been considered as rather transient phenomena, occuring with times scales too short, and on spatial scales too small, to fit into the general notion of the balanced paradigm. Also, the strong, deep convective vertical motions imply a finite nonhydrostatic contribution to the flow. The results discussed in the previous section would suggest however, that for at least part of their life cycle, especially in the mature and dissipating stages, many MCCs display a structure which certainly may be characterized as balanced.

2.2.1 Balance: what do we mean?

The term "balance" as used in the literature of atmospheric science has become so widespread and has so many meanings and connotations that its use is frequently more confusing than enlightening. For that reason we will define balance, as used in this dissertation, to have the following meaning: *A balanced system satisfies (at least to a large degree) a diagnostic relationship which functionally relates the horizontal winds to a thermodynamic variable, such as pressure or geopotential.*[1] In other words, a balanced system has a known relationship between the mass and wind fields.

Balanced weather systems in some sense satisfy, and can be described by, a suitable approximation to the primitive equations of motion. Such an approximated or filtered equation set admits solutions to only a subset of the motions observed in the real atmosphere described by the full primitive equations (PE). In particular, propagating gravity waves are not contained in the balanced equation solution space. In such a balanced system, the balance approximation leads to predictive equations for the nondivergent horizontal winds and the (balanced) mass field. In addition, this system of equations contains a relationship, *consistent with the balance approximation*, which diagnoses divergent horizontal circulations. These secondary circulations are then coupled to vertical motion through continuity.

2.2.2 Balanced Models

The ultimate success and utility of any balanced model can be determined by the degree to which the fluid motions being examined satisfy the underlying assumptions and approximations of the balance condition. Therefore, it is important to choose a balanced model appropriate to the problem being considered. It has been observed, however, that balanced models frequently perform surprisingly well in situations which violate to a considerable degree the assumptions made in the balance condition. Quasigeostrophic (QG) theory

1. Several authors (e.g., Cotton et al.'s (1989) dynamic definition of MCC quoted here earlier) refer to this state as "geostrophic" balance. Geostrophic balance, however, has a rigorous definition which, while reasonably correct in the case of weakly-curved streamlines, generally does not approximate the balance found in sharply-curved flows. Therefore, this potentially misleading nomenclature will not be used here, even though it has become firmly entrenched in the literature.

(Charney 1948) has been found to perform quite well in situations where geostrophic balance may be a poor approximation. Often the errors of balanced models (as compared to PE models or observed weather systems) are a matter of magnitude, with qualitative if not quantitative agreement. Partly because of the relative success of balanced models in unexpected situations, efforts have been made recently to provide new and different scaling arguments justifying the use of existing balanced systems, and also to derive more exact balance approximations for specific situations.

The traditional assumptions used in deriving the various approximate equation systems are seldom justified when considering MCSs. This is perhaps the primary reason that long-lived MCSs have not been considered as balanced systems. The most common approach to deriving an appropriate system of balanced equations (Charney 1955, 1962; Lorenz 1960; Charney and Stern 1962; McWilliams and Gent 1980) is to scale the primitive equations and then consider them as an expansion or power series in some small parameter, typically the Rossby Number, $R_0 = V/fL$. (Here V and L are characteristic velocity and horizontal length scales respectively). Using this approach, various balanced systems are obtained as truncations of the power series, with increasing accuracy resulting from the retention of increasingly higher order terms. For many mesoscale phenomena, and in particular MCSs, R_0 is of order one. Here an expansion in R_0 is clearly not justified as the power series only slowly converges, or indeed may diverge.

In recent years, alternative approaches have been used to obtain a balanced system. Riley et al. (1981) and Lilly (1983) used a scaling appropriate to a large Rossby number but small Froude number, $F = V/NH$, to derive a system of two-dimensional balanced equations. McWilliams (1985) provided a derivation of the nonlinear balance equation system (NLB) which is, under certain circumstances, uniformly valid for all values of R_0. He demonstrated that for systems which are not "geometrically tall", i.e., systems which have an aspect ratio $H/L < 1$, the NLB system has errors scaling as F^2. More recently, Raymond

(1992) considered NLB specifically in the context of midlatitude MCSs. Raymond's approach was to scale the divergence equation using a parameter which is essentially the ratio of horizontal divergence to absolute vorticity. Raymond found that NLB is an adequate approximation to the exact divergence equation when this ratio is suitably small, even for infinite R_0 (no background rotation).

2.3 MCCs and PV thinking

Central to the use and understanding of balanced models is the potential vorticity. Most models make use of some approximation to the Ertel Potential Vorticity (EPV) (Ertel 1942) which is defined as:

$$q = \frac{1}{\rho}(\vec{\xi} \cdot \nabla \theta) \tag{2.4}$$

Actually, the term "potential vorticity" has become somewhat confusing, with various approximations to the EPV and other PV like quantities, all being termed potential vorticity.[2] Here the term PV will be used to mean that quantity referred to by (2.4) or *minor* approximations to same, such as the hydrostatic approximation.

As discussed in several papers, perhaps most notably that of Hoskins et. al. (1985, hereafter HMR), the PV has the useful property of being a conserved quantity in frictionless adi-

2. Actually, one of the more confusing aspects in the history of PV thinking came about with the release of a review paper by Hoskins et al. (1985) titled: "*On the Use and Significance of Isentropic Potential Vorticity Maps*". While the word "isentropic" was meant to modify the word "maps", i.e., plots of PV displayed on isentropic surfaces, it was commonly taken to modify the words "potential vorticity". This misunderstanding, derived from a very influential land mark paper, has led to the acronym "IPV" for *I*sentropic *P*otential *V*orticity. It is worth remembering that *PV is invariant with respect to the vertical coordinate which is used in its calculation.* IPV is not a special kind of PV. The term is still in common use, however as seen in this forecast discussion from the National Weather Service Office in Denver Colorado, issued on June 18, 1994:

IN THE EAST...I WILL CARRY ON TRENDS/CHANGES MADE BY SHORT-TERM
FCSTRS OF MENTNG PSBL SVR TSTMS MNLY NERN ZNS THIS EVE. IN LONGER TERM
...I MAY BUMP POPS UP FROM ISOLATED SUN BASED ON TREND OF NEW ETA AND
THE POSSIBILITY THAT THE AFOREMENTND IPV ANOMOLY CD STILL RESIDE OVR
STATE. DULONG

abatic flows. In the presence of nonconservative forcing, the source or forcing term in the PV equation still has a simple form and can be expressed as the divergence of a "non-advective flux" (Raymond 1992):

$$\frac{dq}{dt} = -\rho^{-1}(\nabla \cdot \vec{Y}) \qquad \textbf{(2.5)}$$

where ***Y***, the non-advective flux, is defined as:

$$\vec{Y} = -H\vec{\xi} + \nabla\theta \times \vec{F} \qquad \textbf{(2.6)}$$

with H the diabatic heating rate, ξ the vector absolute vorticity, and F is the horizontal friction force. When the motion is frictionless (F=0), and adiabatic (H=0), $Y \rightarrow 0$ and q is conserved.

Beyond its conservative properties, the special mathematical structure of the PV makes it an extremely important quantity to balanced model theories. PV is similar to the balance condition mentioned in the last section in that it is a function of the thermodynamic (or mass) fields *and* the wind field. This interrelationship, plus the simple conservation relationship (2.5), make PV an enormously useful (if not intuitive) quantity in balanced dynamical theory.

Note from (2.4) that the exact form of the PV is the product of three independently measured quantities: the density, vector vorticity and the gradient of potential temperature. This means that there are, in principle, an infinite number of ways in which these three quantities can be combined to equal the same value for the scalar q. Use of the hydrostatic approximation introduces a relationship between the vertical distribution of mass and the local density, which can equivalently be expressed as a relationship between density and the vertical gradient of potential temperature. This constraint reduces to two the number of independent quantities which must be specified to determine the PV.

With the introduction of a further balance condition or approximation, which in some manner relates the thermal and wind fields, the PV can be determined by the specification of only one quantity, usually the distribution of pressure or geopotential, from which the other pertinent quantities can be diagnosed. Combining the balance condition with the PV equation (or some approximation of same which is consistent with the assumptions made in the balance approximation) produces a so-called "invertibility principle" (HMR).

Using this invertibility principle with appropriate boundary conditions one can, at least in theory, extract all dynamical and thermodynamical fields of interest. In other words, the invertibility principle determines a (hopefully) unique combination of vorticity and potential temperature fields from the infinite number of possible combinations which satisfy the definition of PV. Within this framework, the prediction of one or two scalar fields (usually PV and, if diabatic effects are being considered, potential temperature) is sufficient to predict the time evolution of the fluid system. This is in contrast to PE models where time-dependent equations for each of the variables must be solved simultaneously.

HMR make a special point of emphasizing that the solution of the system via PV inversion is a *global*, versus local problem. In other words, no knowledge of the thermal or wind fields can be obtained from the value of PV at a single point. Rather, the inversion problem must be solved simultaneously over the whole domain, with the boundary conditions being an important part of the solution, even for points well into the interior. (As will be demonstrated later, this presents one of the problems in inverting the PV using observational or PE model data.)

Vertical profiles of PV are strongly influenced by the vertical thermal structure of the atmosphere. Figure 2.1 shows the PV, for an atmosphere at rest, ($q \approx \rho^{-1} f \partial\theta/\partial z$) associated with the standard atmosphere soundings for 15°, 45°, and 75°in the annual mean. The PV is here displayed in PVU, where 1 PVU = $10^{-6} m^2 s^{-1}$ °K kg^{-1}. These profiles show, at each latitude, a modest monotonic increase in the troposphere, and a dramatic increase in the

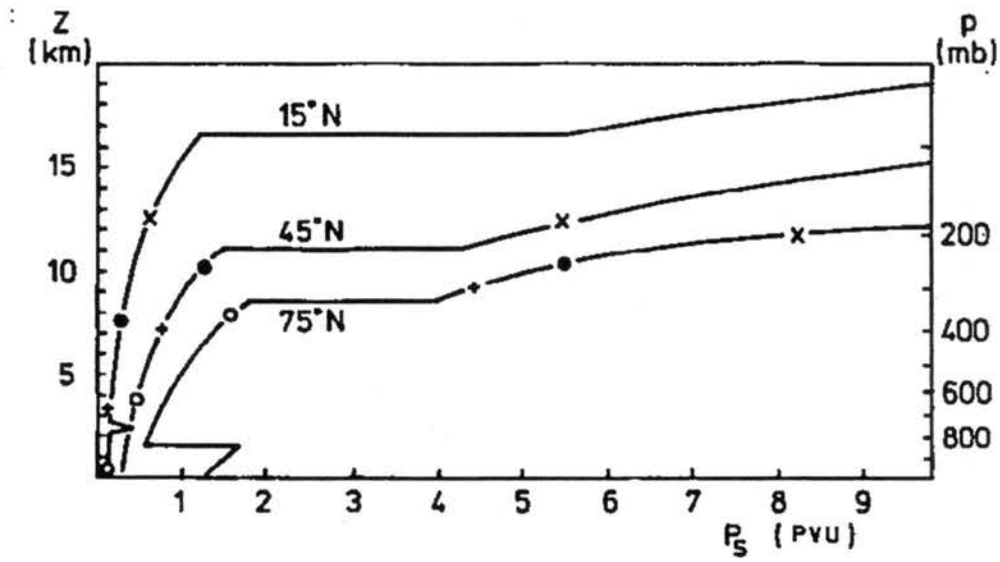

Fig 2.1. *The potential vorticity associated with standard atmosphere temperature profiles and zero relative vorticity. The profiles are the U.S. Standard Atmosphere 15 N annual, mid-latitude spring/autumn (labelled 45° N) and 75° N (cold.). The unit of PV here is the PVU where 1 PVU = $10^{-6} m^2 s^{-1}$ °K kg^{-1}. Note the sharp increase in PV at the tropopause. (Figure from HMR.)*

stratosphere. This almost discontinuous point in *dq/dz* is often used to define the tropopause (HMR). (An exception to the monotonic increase is seen in the lowest few km at 75° N, where the large values of PV are associated with the deep radiationally-induced temperature inversion. Above the boundary layer, the stability assumes more typical values, and in this transition region, *dq/dz* my be strongly negative.)

Due to its quasi-conservative nature, especially in the upper atmosphere where mixing ratios are weak and diabatic processes tend to be weak, PV found its initial use as a tracer, in particular for studies of troposphere/stratosphere interactions (Reed 1955, Reed and Danielsen 1959; Danielsen et al. 1987; Danielsen 1990). Danielsen et al. (1987) found strong correlations between PV and passive chemical tracer concentrations in their study of tropopause folds associated with rapidly deepening extra-tropical cyclones, with stratospheric PV values and ozone concentrations being observed as low as 600 mb.

2.3.1 The PV Impermeability Theorem

One of the more counterintuitive (and contentious) theorems advanced in connection with PV thinking was proposed by Haynes and McIntyre (1987) and further refined by Haynes and McIntyre (1990). This theorem and its implications sparked a debate (e.g., Danielsen 1990; Haynes and McIntyre 1990) though Haynes and McIntyre (1990) pointed out that this is, in large part, due to a disagreement in terminology. Without detailing the controversy, the general theorem, as put forth by Haynes and McIntyre (1987) is:

> "whether or not diabatic forces are acting, ... the following 2 statements hold exactly:
>
> *(i) There can be no net transport of Rossby-Ertel potential vorticity [substance] (PV[S]) across any isentropic surface.*(underlining mine)
>
> *(ii) PV[S] can neither be created or destroyed, within a layer bounded by 2 isentropic surfaces.*
>
> (On the other hand, PV[S] can be transported *along* such a layer, and can be created or destroyed at those places, if any, where the layer terminates laterally.)"

where the above are to taken be in the sense of mass-weighted integrals. Much of the controversy revolves around the use of the term PV. In their later paper, Haynes and McIntyre (1990) replace "PV" with "PV substance" (PVS) in their theorem above. (In the quote above, I have added "S" and "substance" in square brackets to reflect this important notational, and notional, change.)

In the context of a chemical tracer, the role that PV plays is that of a mixing ratio, an intensive quantity. A conceptual problem arises here, because there is no "PV substance" analogous to water vapor or ozone with which to rigorously define PV as a mixing ratio. For this reason, Haynes and McIntyre (1990) suggested the concept of PVS, an abstract substance which is conceptually conserved on a particle basis in the same sense as ozone or water substance. While there is no physical substance equatable with PVS and it has no physical importance, still it is a tautologically useful concept in this context.

If one considers a hypothetical closed container constructed of a membrane which is permeable to air but not to water-vapor, the amount of water-vapor in the container must remain constant. The mixing ratio of dry air mass to water vapor mass, however, will change as air diffuses into, or out of, the container. In the same context, replacing mixing ratio with PV and the membrane with isentropic surfaces, the PVS is conserved, while the PV (like the mixing ratio) changes as mass moves across the isentropic surfaces. The *mass integrated* PV (which is being here considered as a mixing ratio, r) *is* conserved:

$$\int_V \rho r dV = const,$$

even though the total mass bounded by the surface:

$$M = \int_V \rho dV ,$$

varies as mass is transported across the boundaries of the volume V. It is important to remember that the impermeability theorem applies to *potential temperature* surfaces and not constant height or pressure surfaces. These isentropic surfaces, and hence volumes or layers bounded by isentropic surfaces are displaced downward in a stratified atmosphere when diabatic heating occurs, conserving PVS but not (necessarily) mass. Another problem with the PV chemical-tracer analogy, of course, is that PVS is a signed quantity with dynamic sources and sinks, unlike a chemical tracer. This need not be a problem here, however, as PV dynamics implicitly assumes that inertial and static stability are assured (HMR), guaranteeing PV is positive-definite[3].

A consequence of the impermeability theorem is that the notional PVS particles move in just such a way that they never cross θ surfaces (Haynes and McIntyre 1990). Evidently, the advective flux of PV across θ surfaces is *exactly* cancelled by the nonadvective flux in (2.6).[4] This impermeability theorem for PVS will be useful when considering local PV changes in the face of diabatic processes.

3. It is important to note that in the southern hemisphere, the coriolis parameter, *f*, is negative. Here, the criterion for inertial stability is PV < 0.

2.3.2 *Mesoscale convection from the PV viewpoint*

It should be expected that the impermeability theorem, if valid, would reconcile with the more conventional viewpoint of PV thinking. In this section I will discuss convection from 2 PV viewpoints, that of (2.5), the time evolution equation for PV, and also from the standpoint of the impermeability theorem.

First, consider the local effect of diabatic heating on the structure of a potential temperature field which is horizontally uniform in an atmosphere at rest. Local heating bows isentropic surfaces downward and cooling pushes isentropic surfaces upward. This affects PV by modifying the static stability, as seen in Fig. 2.2. The cooling at the surface may be due to evaporative cooling or convergence-forced mesoscale ascent below the level of free convection in a fully developed MCS. The relative deformation from the initial positions of the various isentropic surfaces is related to the change in heating rate with height.

The dipole configuration seen in Fig. 2.2, with a positive PV anomaly in the midtroposphere, and a negative PV anomaly near the tropopause, is well documented and has been observed in several observational and modelling studies. Hertenstein and Schubert (1991), using special data collected during the OK-PRESTORM project, examined the PV distribution in two MCS events. One case consisted of a squall line without a well developed stratiform region of the type seen in the mature stage of an MCC. The second case was an MCC with a large quasi-circular trailing stratiform region.

In the storm with no stratiform region, cross sections orthogonal to the observed convective line revealed an undisturbed and reasonably uniform PV field ahead of the storm effected area. The region behind the squall line showed the dipole structure seen in Fig

4. Bretherton and Schär (1993) point out that the nonconservative flux of Haynes and McIntyre (1990) is unique only to a divergence-free vector, and demonstrate a choice for **Y** in (2.5) which leads to a particularly simple proof of the impermeability theorem. They then prove however, that the form of nonadvective flux given in (2.6) is a unique choice for the nonadvective flux which depends linearly on the local heating rate and fictional forces.

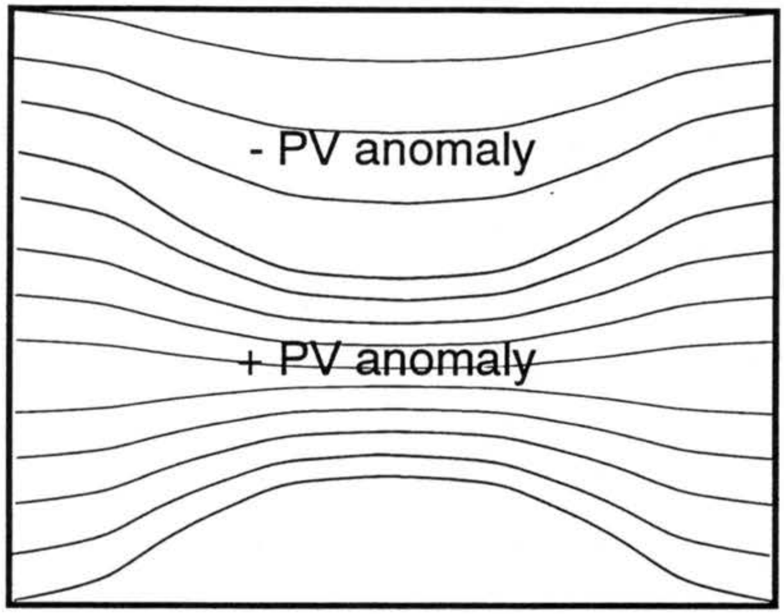

Fig 2.2. *A schematic view of a potential temperature field as it is modified by diabatic heating. The unperturbed basic state is one of constant stratification. The heat released in the middle and upper portions of the domain bows the θ surfaces downward. The enhanced stratification in lower half of the domain results in a positive PV anomaly, while the diminished stratification in the upper part of the domain results in a negative PV anomaly.*

2.2. The positive PV anomaly was confined to the lower half of the troposphere, with midtropospheric PV values remaining fairly similar to values ahead of the squall line. The negative PV anomaly, which appeared above the 320°K isentrope contained regions of negative PV and extended farther forward than positive anomaly located below it. This is probably due to both the stronger storm-relative winds at this height and the strong divergent outflow (Olsson and Cotton 1994).

In addition to a region of strong convection in the mature stages of an MCS, a trailing stratiform precipitation region is frequently observed (Houze et al. 1990). The diabatic structure associated with this feature is different from that in the deep convective region. Here the latent heat release is a maximum in the upper troposphere, with a strong cooling being forced by evaporation of the stratiform precipitation in the lower levels near the surface, as depicted in Fig 2.2.

In the MCC case of Hertenstein and Schubert, where a significant part of the precipitation derived from the stratiform region (Johnson and Hamilton 1988), the PV distribution was more complicated. Here, the positive PV perturbation was found in the midtroposphere, with negative perturbations near the ground and at the tropopause. Fritsch et al (1994) also observed a more three-tiered, or tripole structure in their long lived MCV case study, with a positive PV anomaly dominating the middle troposphere and negative anomalies just above the ground and at the tropopause. The strength of the positive anomaly at 525 mb doubled in a two day period as the flow associated with the MCV generated successive MCS events. Here again the upper-level PV minimum anomaly had about twice the horizontal extent (900 km) of the midlevel maximum (~450 km). This more complicated PV structure may arise partly from the superposition of two dipole structures like that seen in Fig. 2.2, with the shallower and broader stratiform dipole centered above and behind the deeper, but less horizontally extensive, convectively generated dipole.

While PV (in the particle sense) is conserved in adiabatic flows, moist convection is a diabatic process; one in which local PV changes due to both the advective and nonadvective fluxes may be considerable. One of the most obvious effects of convection is the upward transport of mass (but *not* PVS), often from the boundary layer up to the tropopause and perhaps even the lower stratosphere (see Fig 2.3). In a stably stratified environment, this requires transporting mass up the θ gradient (Raymond and Jiang 1990). From the standpoint of the impermeability theorem, this implies enriching the PV (in the same sense as a mixing ratio) in the lower layers while diluting PV in the detraining cloud top in a cumulus cloud, or the outflow anvil in an MCC. As convection progresses, this tends to create a positive anomaly of PV (compared to ambient values) in the lower troposphere and a negative anomaly in the upper troposphere. Hence, the impermeability theorem is in agreement with the dipole configuration seen in Fig. 2.2 and the observations from the squall line case in Hertenstein and Schubert (1991).

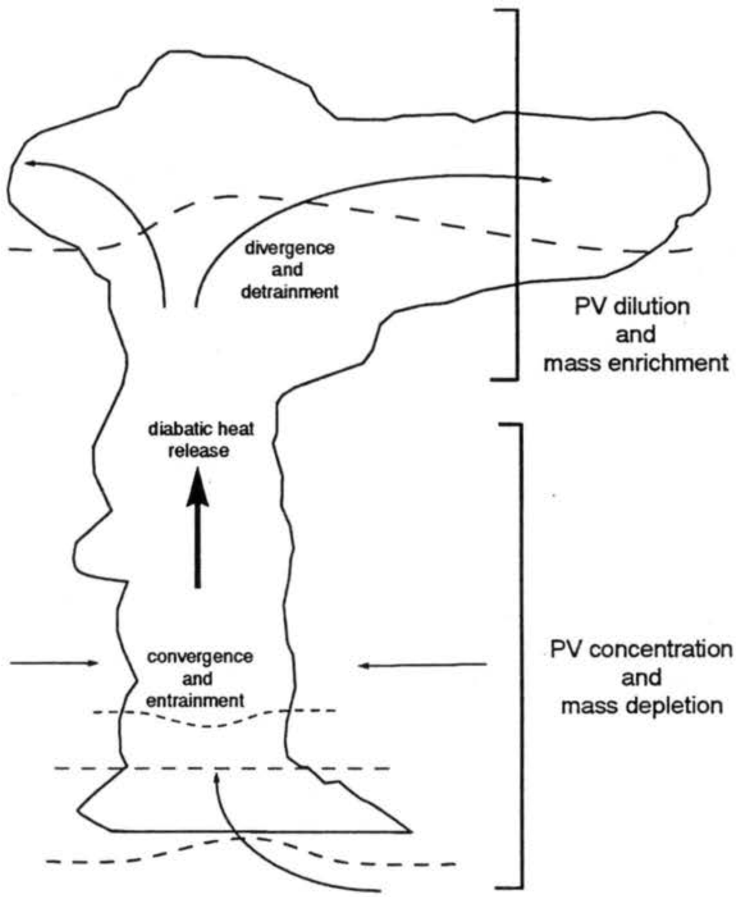

Fig 2.3. *A conceptual model of convection from the viewpoint of the impermeability theorem. The dashed lines represent isentropic surfaces, bowed downward in regions of heating and upward in regions of net cooling. In the region of the strong updrafts, convergence is occuring and mass is crossing θ surfaces. In the anvil region, mass, the PV is being diluted.*

2.3.3 The nonadvective flux of PV: vertical redistribution

Applying a more conventional approach to the PV redistribution caused by cumulus convection, let us consider (2.5). Expanding the substantial derivative gives[5]:

$$\frac{dq}{dt} = \frac{\partial q}{\partial t} + V \cdot \nabla q + w\frac{\partial q}{\partial z}$$

5. In referring to winds, the following convention will be used: V refers to the horizontal (vector) component of the wind, while full three-dimensional wind (including the vertical component) has the symbol U.

and assuming, for now, that PV is horizontally homogeneous, and the absolute vorticity vector is mostly vertical in orientation and varies only weakly with height, the approximate relationship:

$$\frac{\partial q}{\partial t} \approx (-\ )\, w\frac{\partial q}{\partial z} + \rho^{-1}\eta\frac{\partial H}{\partial z} \tag{2.7}$$

holds for frictionless flow. Here, w is the vertical velocity, and η the vertical component of absolute vorticity, which is positive in sign, i.e., the flow is assumed to be inertially stable.

In an environment with substantial vertical shear, the vorticity vector must have a significant horizontal component. The consequent horizontal nonadvective flux can only redistribute PV from one side of the storm to the other (Raymond and Jiang 1990), and has no effect on the vertical flux. Consideration of the horizontal nonadvective flux of potential vorticity in the context of MCSs will be deferred until Section 3.4.

In the early stages of convection, q is typically monotonically increasing with height (see Fig. 2.1) implying $\partial q/\partial z > 0$. This means that initially the vertical advection of q by the convective updrafts is negative everywhere, giving a negative tendency to PV at all levels. The diabatic contribution appears as the second term on the r.h.s. in (2.7) as the vertical divergence of the nonadvective flux. To interpret the effect of this term, it is helpful to consider the conceptual diagram in Fig. 2.4 which shows a typical vertical profile of the convective heating rate, H, in an MCS. A similar schematic profile has been observed in several studies of tropical and midlatitude mesoscale convective events (e.g., Yanai et al. 1973; Gamache and Houze 1982, 1985, Gallus and Johnson 1991).

There are two regions where the gradient of the heating is negative. The lower region results from evaporative cooling below cloud base, and its structure is highly dependent on the local thermodynamic conditions, such as the height of cloud base and the relative humidity between the cloud base and the surface. This cooling may be substantial in high

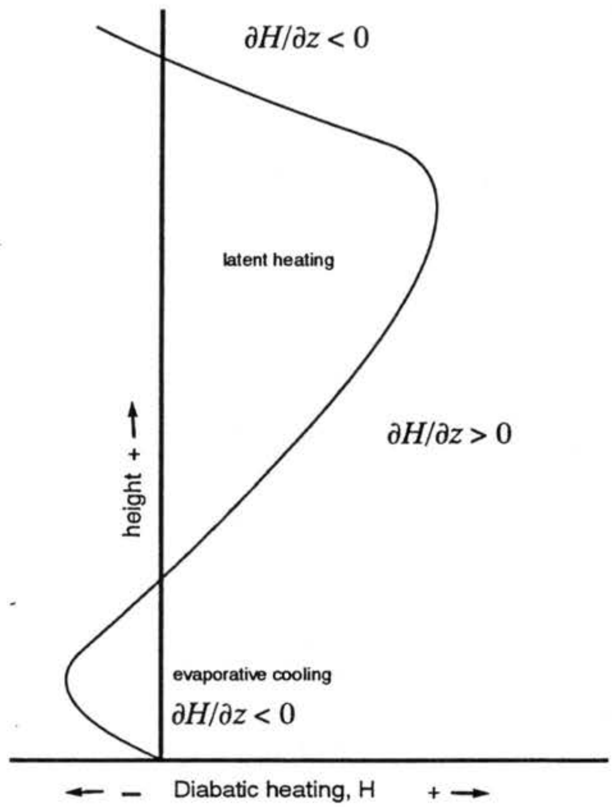

Fig 2.4. *Vertical profile of the diabatic heating rate typical of that measured in a mesoscale convective system. The cooling near the surface is due to evaporation.*

plains thunderstorms with high cloud bases (Bernstein and Johnson 1994, Wakimoto 1985), and almost nonexistent in a nearly saturated sounding typical of tropical conditions. The upper region of negative $\partial H/\partial z$ occurs above the region of maximum heating near the cloud top. This may be enhanced by radiative cooling (Stephens and Webster 1980; Tripoli and Cotton 1989).

Inspection of Fig. 2.4 shows that through much of the layer, the heating gradient is positive. Since we have assumed that η is positive, and ρ must be positive definite, the nonadvective flux provides a positive tendency throughout much of the atmosphere. Above the level of maximum heating, the nonadvective flux divergence provides a negative tendency.

The nonadvective tendency near the ground is harder to deduce, since this is the region where frictional effects are not insubstantial and (2.7) is not a valid approximation.

Combining the tendencies from both terms on the r.h.s of (2.7) we see that in upper- and lower-most regions of the troposphere, the advective and nonadvective fluxes work in concert, while in the middle troposphere, the two tendencies are of opposite sign. Since observations, such as those from the MCC case of Hertenstein and Schubert (1991) show a middle tropospheric maximum in PV, it seems that the nonadvective flux dominates. In the squall-line case of Hertenstein and Schubert pre-squall line values of PV in the midtroposphere were found. Perhaps here the advective and nonadvective fluxes almost cancel.

The above discussion is, strictly speaking, only valid during the initial stages of convection. Once the convection has significantly modified the environment, the baroclinic components of the PV (i.e., those terms proportional to $\partial\theta/\partial x$ and $\partial\theta/\partial y$) become increasingly important. Also, as the storm-induced flow evolves, the horizontal shear generally becomes greater, tilting the vorticity vector more out of the vertical. When these effects become significant, the conceptual model developed here becomes less applicable. As already shown, however, this vertical redistribution of PV on the mesoscale seems to agree quite well with observations and modeling results. Raymond and Jiang (1990) also discussed the heating/cooling associated with an MCC due to radiation and evaporation of precipitation. The evaporative effects should result in an upward flux of PV terminating abruptly at the base of the stratiform anvil, resulting in deposition of PV there. Radiation would partially compensate for this depostion since the base of the anvil would radiatively warm by absorption of upwelling long wave radiation (Stephens and Webster 1980), creating a downward flux away from the base. Raymond and Jiang estimated a value for PV modification of almost 2 PVU day^{-1} for a 2 km layer below the base of a tropical anvil, due to this radiative contribution alone. Radiation cools the cloud tops, causing an upward flux out of the cloud.

2.3.4 The nonadvective flux of PV: horizontal redistribution

As noted earlier, in the absence of frictional effects, the nonadvective flux of PV due to diabatic heating is:

$$\vec{Y}_{diabatic} = -H\vec{\xi}$$

the flux being antiparallel to the absolute vorticity vector. Raymond (1992) evaluated this nonadvective flux for the MCC, considering the situation where there is westerly shear in the lower troposphere in thermal wind balance (θ surfaces rising toward the north), and diabatic heating is occurring in a region of width d ($\perp$ to the shear) and of depth h. Since the slope of the vorticity vector, f/Σ ($\Sigma = \partial u_0/\partial z$, where u_0 is the basic state wind speed), is *upward* and to the *north*, the nonadvective PV flux in the heated region will be *downward* and to the *south*. The relative magnitudes of the aspect ratio of the heating anomaly h/d and the slope of the vorticity vector f/Σ determine whether the flux is vertical or horizontal. This is especially important in regions where $\Sigma > f$, i.e where the vorticity vector is oriented well out of the vertical. For $h/d >> f/\Sigma$, the transport is horizontal, from the cooler to warmer side of the heated region. This would be the case, for example, in the supercell thunderstorm environment. Raymond points out that the counter-rotating supercell thunderstorms occuring in this environment are typically explained as the result of tilting of vortex lines into the vertical, but can equally well be understood in terms of the horizontal nonadvective PV flux.

In the case of the MCC, more typically $h/d << f/\Sigma$, and the transport is mostly vertical, in agreement with observations. Even here though, an asymmetry normal to the shear would be expected. Raymond gives typical values of h and d as 10 km and 300 km, yielding $h/d = 1/30$. In a typical MCC environment, the shear is usually confined to the lowest layers where the low level jet is found, with more barotropic conditions above, though MCCs can occur in environments where substantial shear is found throughout the troposphere.

The total PV distribution due to both the advective flux and nonadvective flux will, of course, depend on a number of factors. These secondary effects become important only after a significant cloud mass has been created and a stratiform anvil has formed and usually act to reinforce the convective tendency to increase PV in the lower troposphere and decrease it aloft (Raymond and Jiang 1990).

With this conceptual model and the use of balanced dynamics it is now possible to consider how the MCC will act as a balanced system. In the next section we will consider the balanced storm scale circulations and how they can act to provide longevity, and even regeneration, to storm systems as they interact with themselves and the background environmental flow.

2.4 Balanced flows associated with MCCs

Raymond and Jiang (1990) extended "PV thinking" in relationship to midlatitude MCSs by studying the interaction of the PV dipole conceptual model with a background vertical shear profile. In this work, they assume that convection has already produced the PV structure as seen in Fig. 2.2. Further they assume:

- an evaporatively-induced cold pool exists at the surface,
- the large-scale environment has some large-scale baroclinicity in balance with the zonal wind,
- a low-level jet (LLJ; Pitchford and London 1962) exists,
- the PV distribution is not differentially advected by a sheared flow, and,
- the perturbation flow does not interact with the perturbation thermal field.

These features do seem to be present in a number of case and composite studies (e.g., Maddox 1983; Menard and Fritsch 1987; Cotton et al. 1989) making this theory generally applicable. Raymond and Jiang discuss two possibilities, relating to the mass perturbation and the wind perturbation associated with the lower (positive) PV anomaly.

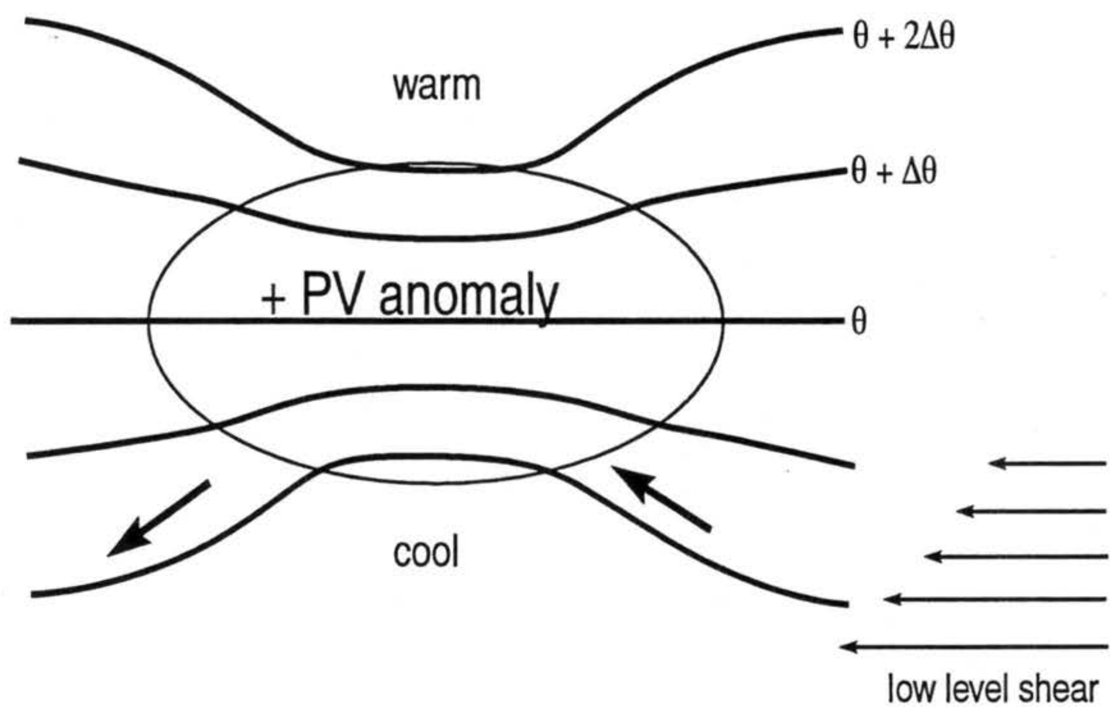

Fig 2.5. *A conceptual model of the low-level PV anomaly interacting with the ambient sheared flow. Here, the potential temperature field, perturbed from below by the evaporatively cooled air and warmed from above by the latent heating in the cloud, is squeezed or compressed, enhancing the static stability and PV. The strong low level flow follows the perturbed θ surfaces upward on the low-level inflow side and downward on the other side. Such adiabatic ascent may cause parcels to reach their level of free convection, amplifying the low-level*

In the first scenario, shown in Fig 2.5 the low-level flow approaching the PV anomaly ascends adiabatically as it follows the storm-perturbed θ surfaces upward. Since this sheared low-level jet often has a very high θ_e value (Maddox 1983), little upward motion may be necessary before the level of free convection (LFC) is reached, especially if negligible convective inhibition (CIN) is present.

The effectiveness of this mechanism in maintaining/regenerating convection depends on the ability of parcels to achieve positive buoyancy during the isentropic lifting process. This, in turn, depends on the strength of the cold pool which is manifested by upward deflected θ surfaces; a stronger cold pool implying greater upward deflection and more

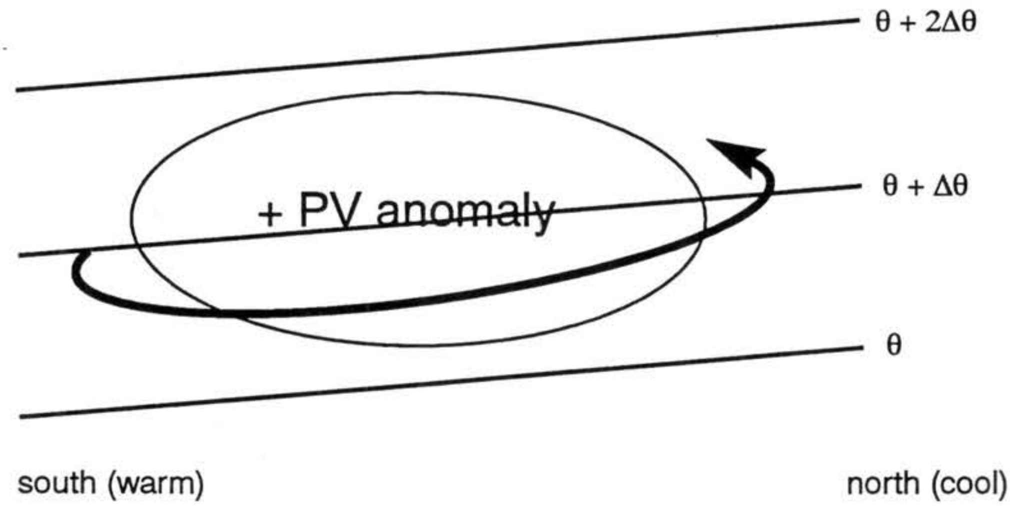

Fig 2.6. *In this diagram, perturbation vortical flow is assumed around the lower (+) PV anomaly. The tilted θ surfaces are assumed to by in thermal wind balance with the ambient westerly shear. Adiabatic perturbation flow will result in ascent on the downshear (east) side. (Figure adapted from Raymond and Jiang, 1990)*

lift. From Fig. 2.2 it is also seen that this is the region of greatest static stability, which will act to impede the upward acceleration of parcels. This mechanism was first proposed by Bosart and Sanders (1981) who suggested that advection of surface parcels over the evaporatively-cooled cold dome could cause lifting sufficient to induce deep convection above a stable boundary layer.

The second scenario proposed by Raymond and Jiang considers the wind, rather than the thermal, field associated with the PV anomaly. This implies the further assumption that a balanced state already exists, that is, that a significant portion of the PV anomaly is due to the relative vertical vorticity field. (Recall that the convection initially perturbs the θ field, *not* the vorticity. Presumably, as the system adjusts to some balanced state, the partitioning between the θ and vorticity fields is modified.) This vertical vorticity implies a storm-induced cyclonic circulation about the positive PV anomaly as in Fig 2.6. If the background wind field is in thermal wind balance, the ambient isentropic surfaces must slope (for example, with westerly shear, isentropic surfaces must tilt down to the south.) Adiabatic perturbation flow will result in ascent (descent) on the downshear (upshear) side. Again, the isentropic upglide may lift parcels until they become positively buoyant.

The importance of this mechanism in MCS enhancement is probably less significant in most situations. While *weak* westerly shear does typically exist in the MCS environment, it is usually small. The baroclinicity required for significant lifting would be larger than typically seen in the MCS environment. Also, the shear seen as a manifestation of the diurnally varying low-level jet is frequently *not* in thermal wind balance (Blackadar 1957; Pitchford and London 1962; McNider and Pielke 1981; Means 1990). Typically, no significant shear exists above this level (Cotton et al. 1989; Fritsch et al. 1994) until just below the tropopause.

It is interesting to note that the two mechanisms mentioned above produce maximum lifting at quite different locations in the existing storm. The vortex-induced flow along tilting isentropic surfaces would produce the greatest lifting for parcels circumnavigating the periphery of the PV anomaly. In contrast, the ambient flow, constrained to follow the perturbed θ surfaces, would experience the greatest lifting for parcel trajectories near the center of the anomaly. As shown by Schubert and Hack (1982), balanced heating near the center of an inertially stable warm core vortex can act most efficiently to amplify the pressure gradient required to maintain or strengthen the vortex.

Observational evidence gives some support to this theory. Fritsch et al. (1994) performed a trajectory analysis of their case and concluded that if parcels from the edge of the storm followed optimal paths into the center of the MCV, they would just achieve positive buoyancy. They also noted that in the several MCS regeneration cycles experienced by this MCV, the new convection initiated near the center of the vortex, rather than along its edges. New convection forced by surface convergence due to outflow from evaporatively-cooled downdrafts (Purdom 1980) is often cited as a prime mechanism for initiating new MCSs (Stensrud and Maddox 1988). In this case however, the new convection was far removed from the outflow-induced convergence region, where CAPE values were far higher, and deep convection more thermodynamically favorable. Fritsch et al. concluded that the barotropic shear profile made this storm more disposed toward back-feeding, where parcel trajectories were more favorable to the isentropic upglide mechanism. It is difficult to assess how important this mechanism would be in the general MCC case without further case studies and model simulations directly addressing this issue.

Raymond (1992) suggested some additional possibilities for both the interaction of environment with the perturbed PV associated with an MCS and the mutual interaction of the perturbed isentropic surfaces (self-advection) with the perturbation vortex. Using his "semi-balanced" model (basically NLB), he found that self-advection was largely responsible for the strongest upward motion in the middle troposphere when no background rotation was present. (With no planetary vorticity, i.e., f=0 and $R_0 \rightarrow \infty$, no thermal wind balance exists. Hence, there can be no tilted ambient θ surfaces balancing a shear profile.) With background rotation, however, the vertical motion associated with vortex-induced motion up and down tilted ambient θ surfaces (the second case discussed above from Raymond and Jiang 1990) was as large as all other effects combined, suggesting that this may be the predominant effect in the middle latitudes. Further, Raymond demonstrated that as the ambient shear deforms the PV anomaly, isentropic surfaces will become increasingly distorted, resulting in time-varying local vertical motion fields (see Fig 2.7). This also has the effect of decreasing the vertical depth of high static stability at any given point near the bottom of the anomaly.

In an actual MCC, all of these effects probably occur to some extent. The shearing of the PV anomaly is most likely to occur in an environment somewhat hostile to barotropic vortex formation. Fritsch et al. (1994) observed that their long-lived MCV remained almost vertically stacked for several days, and propagated in an environment with almost no shear.

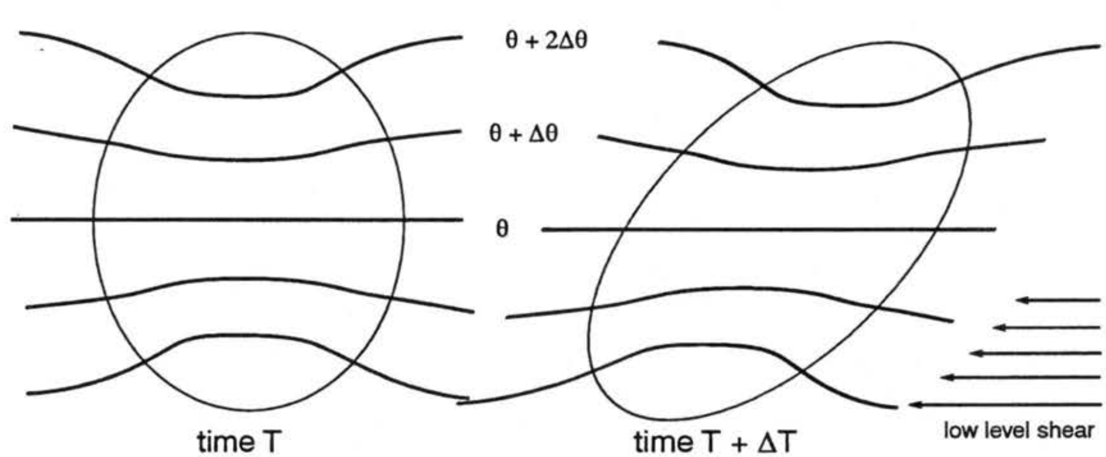

Fig 2.7. *If the horizontal shear is present through a deep enough layer, the developing PV field can become decreasingly distorted. This implies that, even in a reference frame moving with the centroid of the PV anomaly, adiabatic vertical motion may be induced locally.*

2.5 Balanced modeling of MCSs

One of the earliest studies of MCSs with a balanced model was that of Schubert et al. (1989). Here a two-dimensional semi-geostrophic (SG) model, formulated in isentropic-geostrophic coordinates, was used to study the effects of an imposed heating function resembling that which would be created by a infinitely long squall line[6]. A heating function, Gaussian in the horizontal, with a half-width of 40 km, and of half sine-wave shape in the vertical, with a maximum heating rate of 7° K h^{-1} was applied through troposphere of depth $\Theta_T - \Theta_B = 40°$ K. The heating function, designed to be representative of a quasi two-dimensional, linear MCS, was derived from case studies of midlatitude squall lines by Ogura and Chen (1977) and Ogura and Liou (1980). This heating function was propagated through a domain at a phase speed, $c_0 = 50$ km h^{-1}. The background state was of an atmo-

6. In this work, as well as Hertenstein and Schubert (1991), the invertibility principle, rather than being based on the potential vorticity, is based on the potential pseudo-density (Schubert and Alworth 1987), which is inversely proportional to PV. This is in agreement with Ertel's (1942) work, where he demonstrated the existence of a *family* of conserved functions, one of which was PV. Recently other authors have suggested other forms for PV-like quantities, such as Lait (1994), who derives a alternative form of PV which retains the conservative properties, while removing much of the density dependence.

sphere at rest with a constant potential vorticity. As would be expected from theory, the familiar dipole structure in PV was created in the region exposed to the heating.

A further study by Hertenstein and Schubert (1991), using the same model, considered an extension of the same problem. The heating function now included a contribution from a trailing stratiform region, which was more typical of that observed in an MCC (Cotton et al. 1989). Two PRE-STORM squall line cases were simulated, one with and one without a trailing stratiform region. The heating function for the no-stratiform case was the same as in Schubert et al. (1989), while the stratiform case had a smaller "convective" heating rate of 4°K hr^{-1}. The heating effects of the trailing stratiform region were simulated with a full sine wave function in the vertical, giving a maximum heating rate of +2° K hr^{-1} in the upper troposphere and -2° K hr^{-1} in the lower troposphere. The stratiform heating function lagged the convective line heating by 45 km, the negative heating in the lower troposphere modeling the effects of evaporative cooling. In both cases the propagation speed was 50 km hr^{-1} through a background state at rest. Unlike Schubert et al. which had a constant basic state PV (implying a constant static stability), Hertenstein and Schubert used a vertically varying static stability, $-\partial\theta/\partial p$ derived from the 45° N July average U.S. Standard Atmosphere. The resulting basic state PV field, monotonically increasing with height, was more realistic of midlatitude conditions (see Fig. 2.1).

In the stratiform case, the combination of a narrow leading edge convective heating function and a broader stratiform heating/evaporative cooling function resulted in a PV field with a mid-tropospheric maximum, and minima near the top and bottom of the domain. Hertenstein and Schubert concluded that with respect to the resultant PV anomaly, the stratiform heating, when present, dominated the more horizontally confined, though stronger, convective heating.

The results for both cases showed quite reasonable agreement with observations, especially considering the constraints of the 2-D SG model and the lack of ambient wind shear.

One difference between the simple squall line of Schubert at al. (1989), and the no stratiform case of Hertenstein and Schubert is the much greater horizontal extent of the negative upper PV anomaly. This is probably due to the more realistic static stability profile, and agrees with observations (Fritsch et al. 1994) and recent modeling studies (Olsson and Cotton 1994).

A limitation of two-dimensional simulations is the implicit partitioning of horizontal flow, rotational winds are orthogonal to the domain and divergent winds occur within the plane of the domain. Raymond and Jiang (1990) used the more exact nonlinear balance model in three dimensions to consider the effects of a convectively-generated PV anomaly similar to that observed in a midlatitude MCC. In contrast to the previously discussed modeling simulations, no diabatic heating was included. Rather this work focused on the evolution of the wind and thermal fields under the influence various existing (imposed) PV distributions and ambient vertical shear discussed in the previous section.

Raymond and Jiang used a basic state with westerly shear at low and mid levels, balanced by an appropriate θ field with isentropic surfaces sloping upward to the north. They advected two PV anomalies with horizontal radius of 200 km and vertical radius of 3 km for a simulation time of 80 ks, or about 1 day. The negative (upper) anomaly, centered at 10 km AGL had a value of -1.0 PVU while the positive (lower) anomaly was centered at 3 km AGL had a value of +0.3 PVU. The interaction of the storm-relative flow with the basic state thermal field induced large areas of weak vertical motion as the perturbation vortex flow northward moved up the ambient tilted θ surfaces. This adiabatic vertical motion had a maximum of about 1 cm s^{-1}. While this is a fairly weak motion, compared to convectively-induced vertical motions more than 3 orders of magnitude larger, trajectory studies indicated that it could account for more than 500 m of upward motion over the integration period. In a suitable thermodynamic environment this might be of sufficient magnitude to enhance the longevity of the storm.

The deep low-level shear profile used in this study was somewhat atypical for an MCV. Several case studies of MCV-producing MCCs (Menard and Fritsch, 1989; Bartels and Maddox 1991; Fritsch et al. 1994) stress the importance of very weak shear in producing the initial vortical circulation. Without such deep shear in their simulation however, the vortex-induced isentropic lifting would have been significantly less, as the thermal wind relationship would permit less tilting of θ surfaces. This simulation might be most applicable to the special case of an MCV generated in a barotropic environment which then propagates into a more baroclinic environment.

The large shear also makes Raymond's (1992) criterion for predominant vertical transport by the nonadvective PV flux, $h/d << f/\Sigma$, only marginally met. Raymond and Jiang used a value of $\Sigma = 2 \times 10^{-3}\ s^{-1}$ and $f = 10^{-4}\ s^{-1}$ in their NLB model simulation, yielding a value of $f/\Sigma = 1/20$, with $h/d = 1/30$. Also, the vertical extent of the assumed vortex, some 400 km across, is certainly larger than most observed MCVs. Still, Raymond and Jiang demonstrated the ability of balanced circulations associated with MCCs to cause mesoscale upward motion.

To study balanced flows at large Rossby number, Raymond (1992) extended his NLB model to include advection by the irrotational wind. Using this model, in which PV is the prognostic variable, he considered several idealized cases of forced and unforced flows with R_0 of order one and also cases with no background rotation (f=0, $R_0 \rightarrow \infty$). Again attention was focused on the vertical motions associated with interactions of PV anomalies with sheared ambient flow. In addition, Raymond considered the effects of viscous forces and diabatic heating, both of which modify PV through the nonadvective flux (see 2.6).

Raymond demonstrated the development, in a balanced model, of counter-rotating vortices in a strongly sheared supercell environment, by applying diabatic heating representative of the supercell thunderstorm to a basic state in thermal wind balance with a horizontally homogeneous basic state wind. He attributed the vortex generation to the southward transport of PV by the nonadvective PV flux and demonstrated that a similar mechanism can be responsible for the rear-inflow jet (e.g., Johnson and Hamilton 1987; Houze et al. 1990) often seen in squall lines and MCSs. This point is especially interesting since it presents, in the context of balanced dynamics, an explanation of an asymmetric storm-generated circulation feature internal to the MCC.

In what is probably the first attempt to truly simulate an idealized midlatitude MCC in three dimensions with a balanced model, Jiang and Raymond (1994) used the semi-balanced model of Raymond (1992) to simulate the later (stratiform precipitation) stages of a mature MCC. Their model included a stratiform heating/cooling parameterization based on diagnosed vertical motion. Attention was given to the diabatic heating in and below the broad stratiform precipitation area since this gives rise to the vertical motion in this region.

Jiang and Raymond preformed this simulation in two parts. For the first 12 hours, a convective heating function was applied to produce the ubiquitous PV dipole associated with a N-S oriented convective squall line. At the end of the convective period, the dipole had formed, but additionally, a significant horizontal flux had occurred, in agreement with Raymond (1992). Here, however, the resulting counter-rotating vortices are not symmetric since Jiang and Raymond included planetary vorticity in this simulation. Consequently, the midlevel cyclonic vortex was considerably larger than its anticyclonic counterpart, and dominated the flow. The resultant combination of these vortices was a southeasterly inflow jet at midlevels.

For the following 12 hours, the stratiform precipitation/evaporation was parameterized. The southeasterly jet, which had developed during the convective phase, amplified under the influence of diabatic heating as the nonadvective flux continued to act. This jet, traversing over the region of low level evaporative cooling, experienced adiabatic upglide as it followed the upward-bowed θ surfaces. The northward component of the flow additionally forced ascent due to the tilting up of the ambient θ surfaces in balance with the shear. The latent heat release within the stratiform cloud reduced the static stability of the ascending parcels, further enhancing the stratiform upward motion. Jiang and Raymond proposed that this balanced vertical motion is responsible for the longevity of long-lived MCCs.

The simulations were repeated using a variety of environmental shears. An analysis of the energetics found that ambient shear was correlated with the conversion of zonal available potential energy to eddy kinetic energy. An optimal shear value of $2 \times 10^{-3}\ s^{-1}$ was found. For lower shear values the lifting was inhibited, while for higher values, the constituent PV anomalies were sheared apart and the coherent balanced circulations could not function.

This work substantially furthered the understanding on MCCs as balanced systems. While this idealized simulation produced midlevel counter-rotating vortices, which do not seem to be observed in actual MCCs, the balanced dynamics which produced the midlevel southeasterly jet could still occur in a less organized manner, which might be masked by the inhomogeneitys always present in the real MCC environment. More importantly, this work has freed the conceptual balanced model of the of the MCC from the quasi-axisymmetric vortex framework (e.g., Raymond and Jiang 1990) by considering the 3-dimensional PV structure of the MCC.

In the next two chapters, a diagnostic method will be derived which permits the extension of balanced theory beyond idealized balanced model simulations. This technique permits the diagnosis of a balanced state by inverting the PV from a case-study PE simulation of a midlatitude MCC. Such a simulation can include a complex and varying initial state more typical of the large-scale MCC environment. This approach also minimizes the need for other approximations and parameterizations which may confuse the interpretation of the simulation results or compromise their integrity and physical basis.

Chapter 3: Diagnostic Use of the Nonlinear Balance System

3.1 Introduction

In the last chapter, we considered the evolution of the potential vorticity in the vicinity of strong convective heating. Assuming that the flow satisfies some balance criterion, (which may or may not be a valid assumption), it was shown how the modified mass and wind fields could be inferred from the altered PV distribution. It was then shown how these resultant flows could perhaps interact with the mass field to initiate and support a stable and long-lived MCC. Finally, a review was presented of several balanced model studies, which simulated how MCCs and MCC-like storms modify, and interact with, their environment.

Another intriguing application of balanced dynamics is their use as a diagnostic tool. In this chapter, we shall consider this approach and develop a balanced diagnostic system, based on the nonlinear balance approximation, which will be used to analyze the results of a PE simulation of an MCC case study.

3.2 A Consideration of Balance Approximations

The earliest conceived, and most basic, form of horizontal balance approximation is geostrophic balance:

$$f\vec{V}_g = \hat{k} \times \nabla_p \Phi \tag{3.1}$$

which defines the (2-dimensional) geostrophic wind $\mathbf{V}_g$, as a balance between the pressure gradient (height gradient in isobaric coordinates) and the coriolis force. While it has been known for over 150 years that large-scale flow on a rotating sphere was not governed solely by the pressure gradient, Gill (1982) credits Ferrel (1859) with being the first person to truly recognize and quantify the fact that planetary scale motions were governed, to a good approximation, by hydrostasis in the vertical and geostrophy in the horizontal. Ferrel recognized that geostrophic balance would not hold near the ground, where frictional effects were considerable, and at the equator where the vertical component of the coriolis force vanishes. He also argued that as the flows became more curved, the accuracy of geostrophy deteriorated.

Charney (1948) was first to incorporate the geostrophic wind and hydrostatic balance in a rational approximation to the primitive equations. He showed the geostrophic approximation to be valid for a stratified atmosphere when the Rossby Number is small and the flow only weakly divergent. This theory, the quasigeostrophic (QG) system, is probably the most well known and best understood balance theory, partly due to its simplicity. The QG system predicts the geostrophic wind and advects with the geostrophic wind[1]:

$$\frac{\partial \vec{V}}{\partial t} + \vec{U} \cdot \nabla \vec{V} \rightarrow \frac{\partial \vec{V}_g}{\partial t} + \vec{V}_g \cdot \nabla \vec{V}_g . \tag{3.2}$$

The vertical advection of the geostrophic wind is also neglected. Using (3.1), it may be seen that the ageostrophic wind $\mathbf{V}_a$, *does* appear in the coriolis term however, since

$$f\hat{k} \times \vec{V} + \nabla \Phi \approx f_o \hat{k} \times \vec{V}_a + \beta y \hat{k} \times \vec{V}_g \tag{3.3}$$

1. In this and subsequent discussions we will use **U** to indicate the 3-dimensional wind (u,v,w) and **V** to denote the 2-dimensional, horizontal wind $(u,v,0)$. The subscript "g" implies *geostrophic*, and "*a*", *ageostrophic*.

in the limit of small R_0 (Holton 1992). This is vitally important, since retention of this term permits convergence of the average coriolis force f_o, in the corresponding vorticity equation for the QG system:

$$\frac{\partial \zeta_g}{\partial t} = -\vec{V}_g \cdot \nabla (\zeta_g + f) + f_o \frac{\partial \omega}{\partial p}. \tag{3.4}$$

This allows a disturbance to "spin up" due to changes in the vertical velocity (ω) field, which may be forced, for example, by diabatic heating. The horizontal divergent flow, coupled to the vertical motion by the continuity equation,

$$\frac{\partial u}{\partial x} + \frac{\partial v}{\partial y} + \frac{\partial \omega}{\partial p} = 0, \tag{3.5}$$

comprises the secondary circulation necessary to maintain a consistent primary geostrophic and hydrostatic balance. The necessity of such secondary, ageostrophic winds was apparent even before the advent of QG theory. Rossby (1938) demonstrated that geostrophic motion tends to destroy geostrophic balance. Since a state of near geostrophic balance is typically observed on the larger scale, Rossby argued that a small component of ageostrophic motion must constantly exist in the real atmosphere.

In a frictionless, adiabatic environment, the QG system also conserves a PV-like quantity, variously known as absolute potential vorticity, (Charney 1948), and quasi-geostrophic pseudopotential vorticity (PPV, Davis and Emanuel 1991) which has the form:

$$q_p = \nabla^2 \Psi + f_o + \beta (y - y_o) + \frac{\partial}{\partial p}\left(\frac{f_o}{\sigma}\frac{\partial \Phi}{\partial p}\right), \tag{3.6}$$

where $\sigma(p)$, the static stability, is horizontally homogeneous. Holton (1992) refers to this PV-like quantity as a linearized form of the EPV in Eq. (2.4). Charney and Stern (1962) comment that PPV behaves on horizontal (constant pressure) surfaces approximately as EPV behaves on isentropic surfaces.

A weakness of this theory is the lack of horizontal variability in the static stability component of the PPV, and is perhaps the reason that this theory fails to work well in strong baroclinic situations like surface cold fronts (Hoskins 1990). Despite this deficiency in the QG system, and its invalidity in highly curved flows, quasigeostrophic theory has enjoyed considerable success, both in research and in the operational forecasting environment.

A somewhat more general balance system may be derived by using the so called "geostrophic momentum approximation" (GM, Eliassen 1949, Fjørtoft 1962) which replaces:

$$\frac{\partial \vec{V}}{\partial t} + \vec{U} \cdot \nabla \vec{V} \rightarrow \frac{\partial \vec{V}_g}{\partial t} + \vec{U} \cdot \nabla \vec{V}_g. \quad \textbf{(3.7)}$$

The approximation involves replacing the actual momentum (u,v) per unit mass in the momentum equations by the geostrophic momentum (u_g,v_g); hence the name. Contrasting this with (3.2), note that although GM still predicts the geostrophic wind, the *advection* is done by the full 3-dimensional wind **U**, whereas in QG, only geostrophic advection is considered. GM is also valid for flows with large shear vorticity, but small curvature vorticity (Hoskins 1990; Shapiro and Montgomery 1993).

Hoskins (1975) and Hoskins and Draghici (1977) combined the GM approximation with the geostrophic coordinate transformation to produce the elegant semigeostrophic (SG) theory. In the transformed coordinate space, SG appears very much like QG, since the ageostrophic advection is implicit, being embedded in the geostrophic coordinate transformation. This modification permitted the simulation of such features as realistic discontinuous cold frontal structures, more intense lows, and relatively weaker and broader highs (Hoskins 1990). SG has been used with a fair measure of success in a variety of applications ranging from frontogenesis (Hoskins 1975) to polar lows and tropical cyclones (Montgomery and Farrell 1992, 1993). In these latter studies of features with significant curvature vorticity, Montgomery and Farrell obtained reasonable accuracy even for R_0

approaching unity. For the rapidly rotating centers of cyclones, where R_0 is very large, the accuracy degenerated, demonstrating the need for a more general theory.

One criticism of GM (McWilliams and Gent, 1980) is that it neglects the geostrophic advection of the ageostrophic wind while retaining ageostrophic advection of the geostrophic wind. McWilliams and Gent argue that since these terms formally have the same scaling, a consistent truncation in R_0 requires inclusion of the former term as well. They refer to this modification of the GM approximation as hypogestrophy (HG) to distinguish it from SG theory. Snyder et al. (1991) compared baroclinic waves simulated by PE, SG, and HG models. After several days of simulation time, SG deteriorated relative to PE, while HG remained a good balance approximation. Snyder et al. attributed the divergent behavior of the SG model to the small but cumulative errors in the ageostrophic contribution to the PV. HG also has some negative attributes not found in SG, namely nonconservation of particle-wise PV and volume-integrated energy (Xu, 1994).

The above balance systems partition the winds into a primary flow which is geostrophic and a secondary circulation which is ageostrophic. Another approach to obtaining a balanced system comes from approximating at the level of the divergence equation, rather than approximating the momentum equations themselves. This (generally) involves a different partitioning of the winds. Here the decomposition involves a nondivergent primary circulation, typically described by a stream function (Ψ) and an irrotational secondary flow, usually formulated in terms of a velocity potential (χ). Such an approach has led to a family of equations commonly known (unfortunately) as the balance equations (BE, McWilliams and Gent 1980), referred to here as the nonlinear balance (NLB) system.[2]

---

2. I feel that this is a poor choice of terminology, since all the systems of equations described so far in this section are equally well called "balance equations". Rather, I will refer to this as the nonlinear balance (NLB) system (Raymond, 1992) and reserve the term "balance equations" as a generic term for any balanced system. In keeping somewhat with tradition however, I will consider the *specific abbreviation* "BE" as having a meaning identical to "NLB".

The NLB approximation neglects δ and $\partial\delta/\partial t$ in the divergence equation. Therefore, this balance approximation is exact for nondivergent flows, such as gradient wind balance and deformation wind fields. A more complete examination of the NLB system will be deferred until the next section.

The consequences of making the approximation *after* differentiation of the momentum equations are several. Perhaps most importantly, particle conservation of PV does not exist. Further, McWilliams and Gent point out that the existence of a unique solution to the NLB equation has not been demonstrated, though solution bifurcation has not been observed in tests where initial guess fields have been varied considerably (Davis and Emanuel 1991). The NLB system *does* have the advantage of maintaining an integral energy invariant and it retains only those terms necessary to be asymptotically accurate to $O(R_0)$, formally the same accuracy as HG. Using a scaling based on the ratio of across-front flow to along-front flow as a small parameter (ε), Gent et al. (1994) showed that NLB is accurate to $O(\varepsilon^2)$ for sharply curved fronts whereas SG is accurate only to $O(\varepsilon)$.

Several balanced model variations similar to NLB have been proposed and used. Neglecting the nonlinear terms in the NLB approximation yields the linear balance system (LBE, Gent and McWilliams 1983) which is quite similar to QG theory. Raymond and Jiang (1991) developed a system for solving the NLB system if deviations from QG were small. Similar to QG, this model considered advection only by the balanced nondivergent flow, ignoring advection by the balanced secondary circulation. Raymond (1992) improved his "semibalance" model to include these secondary advections. Iversen and Nordeng (1984) evaluated two models intermediate to the NLB system and the primitive equations. Specifically, these more accurate models retained higher order terms of the velocity potential describing the divergent wind. In simulations using actual meteorological data, Iversen and Nordeng found that although the higher order models had problems with computational stability, they produced stronger and more accurate divergent wind fields in some cases.

Allen (1991) proposed a modification of the BE system of McWilliams and Gent (1980) which permits the balance approximation to be made on the momentum equation level, similar to QG and SG. Allen referred to this system as BEM (*b*alanced *e*quations based on *m*omentum equations). This approach results in momentum equations where some terms of order $O(R_0^2)$ are retained. In contrast to NLB, making the approximation on the momentum equation level admits conservation of PV on fluid particles, as well as globally invariant potential enstrophy and energy. In addition, this system permits a more straightforward formulation of consistent and realistic boundary conditions. The actual numerical solution of BEM is usually still done at the divergence/vorticity equation level. These equations are more complete and hence more complicated, than their NLB analogs. Allen also showed that BEM has a spurious high frequency mode. This is a consequence of the inconsistent truncation in R_0 since inclusion of terms containing the velocity potential χ in the BEM balance (truncated divergence) equation, leads to time derivatives, $\partial\chi/\partial t$ when diagnosing the secondary circulation.

A further extension of NLB was introduced by Xu (1994). This model is based on a single truncation of the vector vorticity equation which neglects the advection, stretching and tilting of the secondary flow. This approximation is equivalent to the assumption that the balanced leading order velocity and unbalanced secondary vorticity are assumed nearly parallel with slow spatial variation along leading order flow streamlines. Most notably, Xu's "semibalance" model includes a *rotational* component to the secondary circulation, whereas other NLB models diagnose only the *divergent* secondary flow. This addition permits both particle conservation of PV (not found in BE) and an invertibility principle (absent in BEM).

It should be stressed that these higher-order modifications to NLB are not consistent truncations in the sense described by McWilliams and Gent (1980), and so, *in general*, would not be expected to perform better than NLB.

Recently, another balanced system has been proposed for rapidly-rotating vortices which has the attractive feature of placing no formal constraint on the magnitude of the horizontal divergence or vertical motion. This asymmetric balance (AB) theory of Shapiro and Montgomery (1993), considers an expansion of the square of the ratio of orbital to inertial frequencies, i.e., the square of a local Rossby number on isentropic surfaces. Unfortunately this theory is derived by linearization about a symmetric balanced vortex, an inappropriate basic state for application to MCCs with a leading squall line.

3.3 Diagnostic Use of Balanced Equation Systems

The use of balanced equation systems is not limited to prognostic models. It is possible to exploit the invertibility relationship for any PV distribution, predicted or observed, given proper boundary conditions and a suitable balance approximation. In a prognostic model, this inversion provides the nondivergent winds which may then be used to advect PV at the next time step. The mass or geopotential field obtainable from the inversion describes the balanced thermodynamic structure. In the diagnostic approach, this inversion provides the balanced nondivergent winds and balanced mass field.

Of course, "balance" as used in this context is not uniquely defined. Rather, it depends on the balance approximation being implemented in the invertibility relation. One could quite reasonably talk of a QG balanced wind, SG balanced wind, NLB balanced wind, etc. In the diagnostic use of the PV invertibility, a more accurate balance approximation will hopefully yield better agreement with the observed nondivergent winds. Since all balance approximations eliminate gravity waves, such a diagnostic inversion could also be thought of as a filter, removing gravity-wave effects from observed mass and wind fields.

Davis and Emanuel (1991, hereafter DE) described such a technique, which they used to diagnose the balanced flow component in several observed synoptic situations. Using the NLB equation, and a definition of PV consistent with NLB they developed a 2-equation invertibility relationship. Examining NMC data analyzed at mandatory pressure levels on a $2.5° \times 2.5°$ grid DE diagnosed the balanced wind and geopotential associated with the calculated PV distribution. By decomposing the PV into mean and perturbation parts, they were able to determine how the PV anomalies at various levels effected the total wind and geopotential patterns.

DE found that, for the most part, the inverted winds agreed quite well with the observational data. Most of the discrepancy was due to divergent winds which were not captured in the inversion process. Using the NLB omega equation and parameterized diabatic heating, they also diagnosed the divergent wind associated with the balanced flow. Applying this method to a rapidly deepening extratropical cyclone, they found that the cyclogenesis could be explained by the Eady (1949) model as the interaction of counterpropagating upper and lower Rossby waves (HMR, Hoskins 1990). Davis (1992) made further use of this technique to consider several ways of partitioning PV into mean and perturbation parts. Using this partitioning, he performed "piecewise inversions" of PV to examine the sensitivity of partitioning methods to Rossby number. At large R_0 the greatest discrepancy was found to be above and below the anomaly, with good agreement in the region of the anomaly.

In a more mesoscale application, the method developed in DE and Davis (1992) was used to diagnose an idealized simulation of an MCV produced within an MCS (Davis et al 1993; Weisman et al. 1993). Davis et al. inverted the PV calculated from PE model output and found that the perturbation flow comprising the MCS was largely balanced. This study also determined that the front-to-rear updraft and rear-inflow circulations had no projection onto the horizontally nondivergent balanced flow. They concluded that although the vortical flows were nearly balanced, their formation could not be described within the constraints of balanced dynamics.

It is possible to use other balanced systems as diagnostic tools. For example, the Q-vectors (Hoskins et al., 1978) associated with QG theory, are frequently used to qualitatively describe cyclogenesis (Hoskins 1990; Holton 1992). This approach presupposes a small Rossby number, an assumption which is frequently violated in the regime of deep convection. While the simplicity of QG theory is appealing, its validity is limited to weak disturbances. Similarly, SG theory, while certainly less restrictive than QG, is still limited to flows without large curvature (Montgomery and Ferrell 1993).

It seems desirable to have a tool as versatile as possible. For that reason, the diagnostic system discussed in the remainder of this chapter will be based on the NLB approximation. NLB is based on the assumption of small divergence, a condition obviously violated in the close neighborhood of cumulus scale updrafts. For the mesoscale storm circulation as a whole however, the rotational component of the winds is significantly greater than the divergent component. Therefore, outside the region comprising the convective updrafts, the NLB approximation is a valid one. Also, while the various more generalized models based on NLB (e.g., Xu 1994) have attractive energy and PV conservation properties not found in the simpler BE system of McWilliams and Gent (1980), these improvements appear to have little bearing on the diagnostic use of NLB.

3.4 The Nonlinear Balance System

The NLB system can be obtained from a variety of different approaches, for example as a asymptotic expansion in R_0 (McWilliams and Gent 1980). In the case of large R_0, it has been demonstrated that NLB is still valid if the Froude number is small (Lilly 1983; Riley et al. 1981). Here, we will follow the approach of Raymond (1992) who develops a scaling based on the assumption that ε, the ratio of the irrotational winds to nondivergent winds, is a small quantity. While such an approach is less mathematically rigorous than that of McWilliams and Gent (1980), it is also less cumbersome notationally, and has the benefit of lending some intuitive physical insight into the balance system when horizontally divergent flow can be considered in some sense small. This small divergence approximation is akin to the assumption that gravity wave motions are a significant component of the divergent horizontal flow and that such wave motions are not important to the dynamics being considered.

First, a balance condition relating the mass and wind fields will be obtained. Next, a set of diagnostic equations will be derived describing the divergent "secondary circulations" which act to maintain balance when the system is thermally forced. (We have *not* completely done away with the divergence!)

2.4.1 The nonlinear balance equation

The analysis will use the following set of governing equations in (x,y,π) space:

$$
\begin{aligned}
&\textit{u momentum} && \frac{\partial u}{\partial t}+u\frac{\partial u}{\partial x}+v\frac{\partial u}{\partial x}+\omega\frac{\partial u}{\partial \pi}-fv = -\frac{\partial \Phi}{\partial x}+F_x && (a)\\
&\textit{v momentum} && \frac{\partial v}{\partial t}+u\frac{\partial v}{\partial x}+v\frac{\partial v}{\partial x}+\omega\frac{\partial v}{\partial \pi}+fu = -\frac{\partial \Phi}{\partial y}+F_y && (b)\\
&\textit{hydrostatic} && \frac{\partial \Phi}{\partial \pi} = -\theta && (c)\\
&\textit{continuity} && \frac{\partial u}{\partial x}+\frac{\partial v}{\partial y}+\pi^{-\mu}\frac{\partial}{\partial \pi}(\pi^{\mu}\omega) = 0 && (d)
\end{aligned}
\qquad \mathbf{(3.8)}
$$

where $F_{x,y}$ represent frictional and other dissipative forces, $\pi = c_p(p/p_0)^{\kappa}$ is the Exner function, $\omega = d\pi/dt$ is the vertical velocity in the Exner function coordinate system, $\Phi = gz$ is the geopotential, $\kappa = R/c_p$ and $\mu = 1/\kappa - 1$.

To derive the nonlinear balance equation, first form the divergence equation from the sum of ∂/∂x (3.8a) + ∂/∂y (3.8b), which gives:

$$\frac{d\delta}{dt} + \delta^2 - 2\frac{\partial u}{\partial x}\frac{\partial v}{\partial y} + 2\frac{\partial v}{\partial x}\frac{\partial u}{\partial y} + \frac{\partial \omega}{\partial x}\frac{\partial u}{\partial \pi} + \frac{\partial \omega}{\partial y}\frac{\partial v}{\partial \pi} - f\left(\frac{\partial v}{\partial x} - \frac{\partial u}{\partial y}\right) + u\frac{\partial f}{\partial y} =$$

$$-\frac{\partial}{\partial x}\left(\frac{\partial \Phi}{\partial x}\right) - \frac{\partial}{\partial y}\left(\frac{\partial \Phi}{\partial y}\right) + \nabla \cdot \mathbf{F} \qquad \mathbf{(3.9)}$$

where $\delta = \partial u/\partial x + \partial v/\partial y$ is the horizontal divergence, $\mathbf{F} = (F_x, F_y)$, and $\nabla = \mathbf{i}\partial/\partial x + \mathbf{j}\partial/\partial y$ is the horizontal Laplacian operator.

Next, using Helmholtz's theorem (Arfken, 1970) the horizontal wind is decomposed into irrotational and nondivergent components. This is accomplished by defining a streamfunction, Ψ and a velocity potential, χ, with the following properties:

$$\vec{V}_h = (u, v, 0) = \nabla \chi - \nabla \times \Psi \hat{k}$$

$$\nabla \chi = \left(\frac{\partial \chi}{\partial x}, \frac{\partial \chi}{\partial y}\right) = (u_\chi, v_\chi), \qquad -\nabla \times \Psi \hat{k} = \left(-\frac{\partial \Psi}{\partial y}, \frac{\partial \Psi}{\partial x}\right) = (u_\Psi, v_\Psi)$$

$$\nabla^2 \chi = \nabla \cdot \vec{V}_h = \delta, \qquad \nabla^2 \Psi = \nabla \times \vec{V}_h = \xi, \qquad \nabla \cdot (\nabla \times \Psi \hat{k}) = \nabla \times \nabla \chi = 0 \qquad \mathbf{(3.10)}$$

where ξ is the relative vorticity. Note that this decomposition has the ambiguity that flow which is *both* nondivergent *and* irrotational may be represented by either Ψ or χ. To remove this ambiguity the following convention is used: *all flow which is both irrotational and nondivergent is represented by the streamfunction, Ψ. Thus, all flow represented by χ is strictly divergent and (u_χ, v_χ) shall henceforth be referred to as the divergent flow.*

Now, with the definitions in (3.10) the last 2 terms on the l.h.s. of (3.9) may be rewritten as:

$$-f\left(\frac{\partial v}{\partial x} - \frac{\partial u}{\partial y}\right) + u\frac{\partial f}{\partial y} = -f\nabla^2 \Psi + \left(-\frac{\partial u}{\partial y}\right)\frac{\partial f}{\partial y} = \nabla \cdot (f\nabla \Psi) \,. \qquad \mathbf{(3.11)}$$

Again, the central approximation of NLB is that the divergence, *and equivalently, motion associated with the divergence*, is in some sense small compared to the vorticity and its associated flow fields. Formally, this implies: $\mathbf{v}_\chi \sim \varepsilon \mathbf{v}_\psi$ and $\nabla^2\chi \sim \varepsilon\nabla^2\xi$, with $\varepsilon << 1$. From the continuity equation (3.8d) and the horizontal divergence, $\delta = \nabla^2\chi$, a scaling for ω may be obtained. Following Raymond (1992), the scale factors used are:

$$
\begin{aligned}
&v_\Psi \sim U && \Psi \sim UL \\
&v_\chi \sim \varepsilon U && \chi \sim \varepsilon UL \\
&u, v \sim U && \pi \sim \Delta\Pi \\
&\omega \sim \Omega \sim \varepsilon\frac{U}{L}\Delta\Pi && \Phi \sim f\Psi \sim fUL \\
&\nabla^2\chi = \delta \sim \varepsilon\frac{U}{L} && \nabla^2\Psi = \xi \sim \frac{\partial u}{\partial y} \sim \frac{U}{L} \\
&t \sim T \sim \frac{L}{V} &&
\end{aligned}
\qquad \mathbf{(3.12)}
$$

where $\Delta\Pi$ is a characteristic pressure depth, say the depth of the troposphere and ε is the ratio of divergence to vorticity . As noted by Lilly (1983) and Raymond (1992), the timescale L/V is the *advective* timescale, *not* the gravity wave timescale $1/N$. This is an important distinction since the advective processes contained in the NLB omega equation will be shown to be the mechanism by which this system maintains balance under the influence of diabatic heating.

Now, scaling the frictionless divergence equation gives:

$$
\begin{array}{ccccccc}
\dfrac{d\delta}{dt} + \delta^2 + & 2\left[-\dfrac{\partial u}{\partial x}\dfrac{\partial v}{\partial y} + \dfrac{\partial v}{\partial x}\dfrac{\partial u}{\partial y}\right] + & \left[\dfrac{\partial \omega}{\partial x}\dfrac{\partial u}{\partial \pi} + \dfrac{\partial \omega}{\partial y}\dfrac{\partial v}{\partial \pi}\right] & - \nabla\cdot(f\nabla\Psi) & + \nabla^2\Phi & = 0 \\
\varepsilon\dfrac{U}{L}\dfrac{U}{L} \quad \varepsilon^2\left(\dfrac{U}{L}\right)^2 & \left(\dfrac{U}{L}\right)^2 & \varepsilon\dfrac{U\Delta\Pi}{L^2}\dfrac{U}{\Delta\Pi} & f\dfrac{UL}{L^2} & f\dfrac{UL}{L^2} &
\end{array}
\qquad \mathbf{(3.13)}
$$

where only lowest order powers of ε are indicated in the terms containing u,v. Retaining only terms not containing ε (which is equivalent to dropping any terms relating to the divergent wind, v_χ), yields the following relationship:

$$\nabla^2\Phi - \nabla\cdot(f\nabla\Psi) + -2\left[\frac{\partial^2\Psi}{\partial x^2}\frac{\partial^2\Psi}{\partial y^2} - \left(\frac{\partial^2\Psi}{\partial x\partial y}\right)^2\right] = 0 \qquad \textbf{(3.14)}$$

which is the nonlinear balance equation, first introduced by Charney (1955). This is a rather remarkable result. The divergence equation has been scaled in such a manner that the divergence is not retained! The remaining terms must be those which are nearly in balance when the divergence is small. Alternatively, the divergence equation apparently has several relatively large terms which tend to cancel.

Several comments are in order regarding the form of this equation. The geostrophic relationship $(u_g,v_g) = f^{-1}(-\partial\Phi/\partial y, \partial\Phi/\partial x)$ yields a definition for the geostrophic streamfunction, $f\Psi_g = \Phi$. Using this definition in the f-plane approximation of the NLB equation gives:

$$\nabla^2(f\Psi_g - f\Psi) = 2\left[\frac{\partial^2\Psi}{\partial x^2}\frac{\partial^2\Psi}{\partial y^2} - \left(\frac{\partial^2\Psi}{\partial x\partial y}\right)^2\right]. \qquad \textbf{(3.15)}$$

If the nonlinear term on the r.h.s. of (3.15) is dropped, geostrophic balance is recovered. Consequently this nonlinear term, which may be written as the jacobian

$$\frac{\partial[(\partial\Psi/\partial x), (\partial\Psi/\partial y)]}{\partial(x,y)} \qquad \textbf{(3.16)}$$

is also referred to as the ageostrophic term. If f is allowed to vary, i.e., $f = f^{cn}(y)$, and the nonlinear term is dropped, the so called linear balance is obtained. This is almost the same as geostrophic balance with the retention of the term $u(\partial f/\partial y)$ (see 3.11). In the context of the divergence equation, this term, which comes from the v-momentum equation, produces convergence resulting from the increasing coriolis torque as f increases poleward, even in the case where $u \neq f^{cn}(y)$. In the linear balance approximation, the mass field must balance this term as well as the geostrophic wind. Note also that the NLB equation is strictly 2-dimensional, with no vertical derivatives or vertical velocities and therefore no vertical coupling between horizontal levels in this equation.

2.4.2 A consistent PV approximation

As noted before, Ertel's PV in cartesian coordinates is given by:

$$q = \rho^{-1}\,\vec{\eta} \cdot \nabla\theta$$

which, when expanded in its approximate hydrostatic form, becomes:

$$q = -\frac{\partial v}{\rho \partial z}\frac{\partial \theta}{\partial x} + \frac{\partial u}{\rho \partial z}\frac{\partial \theta}{\partial y} + \left(\frac{\partial v}{\partial x} - \frac{\partial u}{\partial y} + f\right)\frac{\partial \theta}{\rho \partial z}. \qquad \textbf{(3.17)}$$

This approximation to the potential vorticity contains no vertical velocity terms, i.e., no horizontal shear of the vertical wind. Since the hydrostatic approximation to the vertical equation of motion sets the substantial derivative of vertical velocity to zero, this is the vorticity predicted by the (vector) vorticity equation. To obtain the proper (approximate) form using the Exner function as a vertical coordinate, the density, ρ, is replaced by the proper pseudo-density $\sigma_\pi = -\rho\theta/g = -p/g\kappa\pi$, which may be obtained from the hydrostatic equation. This gives

$$q = -\frac{g\kappa\pi}{p}\left[-\frac{\partial v}{\partial \pi}\frac{\partial \theta}{\partial x} + \frac{\partial u}{\partial \pi}\frac{\partial \theta}{\partial y} + \left(\frac{\partial v}{\partial x} - \frac{\partial u}{\partial y} + f\right)\frac{\partial \theta}{\partial \pi}\right]. \qquad \textbf{(3.18)}$$

When the same scaling and truncation applied to the divergence equation is applied to (3.18) along with the hydrostatic identity, the NLB approximation to the PV is obtained:

$$q = -\frac{g\kappa\pi}{p(\pi)}\left[\frac{\partial^2\Psi}{\partial\pi\partial x}\frac{\partial^2\Phi}{\partial\pi\partial x} + \frac{\partial^2\Psi}{\partial\pi\partial y}\frac{\partial^2\Phi}{\partial\pi\partial y} - (\nabla^2\Psi + f)\frac{\partial^2\Phi}{\partial\pi^2}\right]. \qquad \textbf{(3.19)}$$

This approximate form of the full Ertel PV equation neglects:

1. vertical shear of the divergent winds, $\mathbf{v}_\chi$, and,
2. horizontal shear of the vertical velocity, (a consequence of the hydrostatic approximation).

Equations (3.14) and (3.19) represent the invertibility condition for the NLB balance system. In simpler balance systems, such as the QG theory, it is possible to reduce the balance equation (in that case simply the definition of the geostrophic wind) to the functional form $\Psi = f^{cn}(\Phi)$, reducing the invertibility condition to a single equation. Unfortunately, due to the complicated nature of the nonlinear balance equation (3.14), the invertibility condition is defined by 2 nonlinear second order differential equations which must be solved simultaneously for the variables Ψ and Φ. This is probably the principal reason that the NLB system has not been used more widely in a prognostic model.

The invertibility condition described above, plus suitable boundary conditions and a given PV distribution, constitute a well-posed problem from which, at least in principle, the balanced horizontal nondivergent winds ($\mathbf{v}_\Psi$) and balanced mass field may be extracted. From the vertical gradient of the balanced geopotential (Φ_b) the balanced potential temperature (θ_b) can be computed from the hydrostatic relation. This, however, is not the most complete representation of the slow manifold flow obtainable from the NLB model.

4.2.1 An ω equation for the NLB system

Lacking in the framework presented so far is a representation of vertical motion. Almost any weather system of interest involves diabatic processes, most notably latent heat release in clouds. The MCS represents an extreme example since heating rates in MCSs are among the largest of any natural atmospheric phenomena. An understanding of the slow manifold behavior of the MCS requires a theory for how the balanced flow evolves in the presence of this strong diabatic forcing.

The full primitive equations allow for a rich variety of responses to this heating. Sound waves are produced almost immediately as a response to rapid local changes in density.

Vertical motion and acoustic waves are induced almost immediately as the atmosphere responds to heating related buoyancy production (Nicholls et al. 1991). In a stably stratified atmosphere, this will produce gravity waves as parcels displaced by the buoyant rising plume seek an equilibrium state. The convective elements themselves eventually reach and overshoot their equilibrium level, producing strong oscillations in the upper troposphere and stratosphere (Bretherton and Smolarkiewicz 1989; Gossard and Hooke 1975). These modes of response, characterized by divergent flow and relatively fast oscillations, radiate energy away from the heat source and project on the fast manifold of the primitive equations.

In addition to these fast manifold modes, the primitive equations also admit a large scale *nonradiative* divergent response, which is considered a projection on the slow manifold. It is through these divergent motions that balance is achieved and maintained. It is once again useful to appeal to PV thinking to see how this comes about. As noted before, even after the hydrostatic approximation is applied to the Ertel PV, there are still an infinite number of combinations of $\theta(x,y,\pi)$ and $\eta(x,y,\pi)$ which satisfy a given PV distribution. Initially, the diabatic heating perturbs the PV largely through changes in $\nabla\theta$. However, the partitioning of PV between the vorticity and $\nabla\theta$ is uniquely defined by the balance condition (here the NLB equation). The balance condition, in the general case, will not partition PV with the whole perturbation in the θ distribution. Accordingly, adjustments in both the vorticity and potential temperature fields are required to allow the perturbed PV to achieve the correct partitioning. Evidently, the balance condition puts a very significant constraint on how the system can adjust.

The modification of the vertical vorticity field can be understood by examining the vertical vorticity equation:

$$\underset{a}{\frac{\partial \zeta}{\partial t} + \mathbf{v}_{\psi} \cdot \nabla (\zeta + f)} = \underset{b}{-\mathbf{v}_{\chi} \cdot \nabla (\zeta + f)} \underset{c}{- \omega \frac{\partial \zeta}{\partial \pi}} \underset{d}{- \delta (\zeta + f)} + \underset{e}{\left(\frac{\partial \omega}{\partial y}\frac{\partial u}{\partial \pi} - \frac{\partial \omega}{\partial x}\frac{\partial v}{\partial \pi}\right)} \qquad \textbf{(3.20)}$$

which indicates that local changes in the (relative) vorticity may be brought about by: horizontal advection of absolute vorticity, by a) the nondivergent wind and b) the divergent wind, c) vertical advection of relative vorticity, d) horizontal convergence, and e) tilting of horizontal vorticity into (or away from) the vertical.

Similarly the thermodynamic equation:

$$\frac{\partial \theta}{\partial t} + \mathbf{v}_{\psi} \cdot \nabla \theta = -\mathbf{v}_{\chi} \cdot \nabla \theta - \omega \frac{\partial \theta}{\partial \pi} + H \qquad \textbf{(3.21)}$$

indicates changes in θ result from advection and diabatic heating, represented in (3.21) by H. Both (3.20) and (3.21) are, as yet, exact within the hydrostatic and inviscid approximations. Note that in both equations the advection is by the *total* wind. In addition, term (d) in (3.20) explicitly relates divergence to the relative vorticity change. A naive scaling, which would seem consistent with the approximations to the NLB and PV equations, would be to neglect all terms which scale as ε, i.e., those terms which contain the divergent winds, $\mathbf{v}_{\chi}$. From the foregoing discussion, however, it should be apparent that some form of divergent flow is required in the balanced description if we are to consider vertical motion. (There are other compelling arguments for maintaining some of the divergent wind terms. They will be discussed at the end of this section.) Recasting the continuity equation, (3.8d) in terms of the velocity potential, χ:

$$\begin{array}{ccc} \pi^{-\mu} \dfrac{\partial}{\partial \pi} (\pi^{\mu} \omega) & = & -\nabla^2 \chi \\ \Delta\Pi \varepsilon \dfrac{U}{l} \dfrac{1}{\Delta\Pi} & & \varepsilon \dfrac{U}{l} \end{array} \qquad \textbf{(3.22)}$$

indicates that for any nontrivial $\omega(\pi)$, divergent flows must be considered. Therefore, terms of $O(\varepsilon^1)$ must be retained to diagnose nontrivial secondary circulations.

Examination of the vorticity equation indicates that all terms on the r.h.s. of (3.20) scale as ε. Expanding the tilting term, (e) in the vorticity equation gives:

$$\left(\frac{\partial\omega}{\partial y}\frac{\partial u_\Psi}{\partial\pi}-\frac{\partial\omega}{\partial x}\frac{\partial v_\Psi}{\partial\pi}\right) + \left(\frac{\partial\omega}{\partial y}\frac{\partial u_\chi}{\partial\pi}-\frac{\partial\omega}{\partial x}\frac{\partial v_\chi}{\partial\pi}\right)$$

$$\varepsilon\left[\frac{U}{l^2}\Delta\Pi\frac{U}{\Delta\Pi}\right] \qquad \varepsilon^2\left[\frac{U}{l^2}\Delta\Pi\frac{U}{\Delta\Pi}\right] \quad . \tag{3.23}$$

Neglecting the second term in (3.23), which scales as ε^2, yields a vorticity equation which is a consistent truncation to $O(\varepsilon^1)$. The r.h.s. of the thermodynamic equation (3.21) scales as ε and it is retained intact.

Using the above results, it is now possible to derive a diagnostic equation for the vertical velocity, namely the NLB ω equation. While the algebra is involved, the essential scheme combines the complete thermodynamic equation, the balanced vertical vorticity equation, and the nonlinear balance equation as shown schematically in (3.24), where the term *J(t)* is the time derivative of the jacobian term in the NLB equation (i.e $\partial/\partial t$ (3.16)), *H(t)* is the diabatic warming rate, $\beta = \partial f/\partial y$ and $\sigma = \partial^2\Phi/\partial\pi^2 = -\partial\theta/\partial\pi$ is the static stability.

The NLB ω equation (3.24) and the continuity equation (3.22) represent a coupled system in ω and χ, the vertical and horizontal components of *balanced* divergent wind. Similar to the coupled system in Φ and Ψ introduced earlier in this section, a solution, $\omega(x,y,\pi)$, $\chi(x,y,\pi)$ can, in principle, be found which simultaneously satisfies these equations and accompanying boundary conditions. Like the Φ,Ψ set, one of these equations, in this case the continuity equation, is a 2-dimensional Poisson equation, while the ω equation is 3-dimensional. *Unlike* the Φ,Ψ set, these equations are linear and therefore less sensitive to initial guess fields.

The ω equation shows how, through a great variety of simultaneous interactions, the divergent part of the flow balances with the PV and balance equation. The terms on the r.h.s. of

$$\nabla^2 \quad \left[\frac{\partial \theta}{\partial t} + \mathbf{v}_h \cdot \nabla\theta + \omega\frac{\partial \theta}{\partial \pi} = H\right] \qquad \textit{(thermodynamic equation)}$$

$$-\frac{\partial}{\partial t}\frac{\partial}{\partial \pi} \quad \left[\nabla^2 \Phi - \nabla \cdot (f\nabla\Psi) + -2\left[\frac{\partial^2\Psi}{\partial x^2}\frac{\partial^2\Psi}{\partial y^2} - \frac{\partial^2\Psi}{\partial x \partial y}\right] = 0\right] \qquad \textit{(Nonlinear balance equation)}$$

$$-f\frac{\partial}{\partial \pi} \quad \left[\frac{\partial \zeta}{\partial t} + \mathbf{v}_\Psi \cdot \nabla\ (\zeta + f) = -\mathbf{v}_\chi \cdot \nabla(\zeta+f) - \omega\frac{\partial \zeta}{\partial \pi} - \delta(\zeta+f) + \left(\frac{\partial \omega}{\partial y}\frac{\partial u}{\partial \pi} - \frac{\partial \omega}{\partial x}\frac{\partial v}{\partial \pi}\right)\right]$$

(balanced vorticity equation)

$$\downarrow$$

$$f\eta\frac{\partial}{\partial \pi}\left(\pi^{-\mu}\frac{\partial \Psi}{\partial \pi}(\pi^{\mu}\omega)\right) + \nabla^2(\sigma\omega) =$$

$$+\left[f\frac{\partial}{\partial \pi}\left(\frac{\partial^2\Psi}{\partial x \partial y}\frac{\partial \omega}{\partial x} + \frac{\partial^2\Psi}{\partial x \partial y}\frac{\partial \omega}{\partial y}\right) - \left(f\frac{\partial \eta}{\partial \pi}\frac{\mu}{\pi} + \frac{\partial^2\Psi}{\partial \pi^2}\right)\omega\right] \qquad f^{cn}(\omega)$$

$$+\left[\nabla^2\ (\mathbf{v}_h \cdot \nabla\theta) + f\frac{\partial}{\partial \pi}(\mathbf{v}_h \cdot \nabla\eta)\right] \qquad f^{cn}(\chi)$$

$$+\left[-\beta\frac{\partial^2\Psi}{\partial x \partial y \partial t} - \frac{\partial}{\partial \pi}J(t) - \nabla^2 H(t)\right] \qquad f^{cn}(t)$$

(3.24)

(3.24) are grouped as functions of vertical velocity, velocity potential and time. Recall that through the hydrostatic relation, θ and Φ are related. This implies that the balanced Φ determined by the Φ,Ψ set is sufficient to determine the "balanced θ". Likewise, η comes from Ψ, and is also balanced. The second group of terms above, which are functions of $\mathbf{v_h}$, the *total* horizontal wind (and hence functions of χ), adjust the differential horizontal advection of (balanced) vorticity and (balanced) θ with the spatial distribution of ω. The continuity equation simultaneously maintains the conservation of mass as a function of the balanced horizontal divergent flow and the balanced vertical motion.

The last set of terms on the r.h.s. of (3.24) are functions of time, and determine how the vertical motion is affected by:

1) the spatially-varying coriolis torque interacting with time-varying sheared zonal flow,
2) time varying vertically-sheared nondivergent ageostrophic flow, and
3) the spatial distribution of the diabatic heating.

In a precipitating MCS, this last term is usually quite large, and frequently dominates the ω forcing.

The 2 sets of equations outlined here completely define the 3-dimensional balanced flow (both nondivergent and divergent) through Ψ, χ, and ω, and the balanced mass field through Φ. From these quantities, all the other relevant balanced dynamical properties of the fluid system can be deduced.

It should be evident that the solution of the above system is not by any means trivial. The assertion that solutions can, in principle, be obtained *does not imply* that they can be obtained in practice. The highly nonlinear Φ,Ψ equation system in particular is quite sensitive to the initial guess fields of Φ and Ψ, especially in regions where the flow is strongly sheared and significantly ageostrophic. While the atmosphere is able to maintain a state of balance quite close to that defined by this system, the attempts of man to simulate this balance are often less successful!

Chapter 4: Numerical Solution of the Nonlinear Balance System

4.1 Introduction

In Chapter 3, the NLB balanced equation set was derived with the intention of using this system to diagnose the balanced component of flow from PE model simulations. In this chapter, the application of this balance system in such a diagnostic sense will be discussed.

In the next section we will consider how the invertibility may be reformulated to facilitate the numerical solution. In the Section 4.3 the strategy used to achieve convergence of the 2 equation system will be discussed. This requires a careful selection of a first guess field for both the geopotential and the streamfunction. Care must also be exercised to prevent the solution from leaving its attractor basin as the solution evolves. In addition, the data at times violate some of the basic assumptions, such as implicit stable stratification, and need to be filtered to prevent divergence of the numerical scheme.

Appropriate boundary conditions are an essential part of the PV inversion (HMR). Balanced model simulations are often formulated such that the boundary conditions are simple to apply. When inverting observed or PE model-generated data, the specification of boundary conditions can be much more difficult. In Section 4.4 this problem is addressed and a method is presented to derive approximate boundary conditions which agree well with observations.

4.2 A More Tractable Invertibility Equation Set

The Ψ,Φ equation system given by (3.14) and (3.19) can be further rearranged to facilitate the solution (DE). To do this it is convenient to nondimensionalize the equations using the following dimensional factors:

$$\Psi = \sigma\frac{\Pi^2}{F}\tilde{\Psi} \qquad \Phi = \sigma\Pi^2\tilde{\Phi} \qquad q = \sigma F g \kappa C_p p_0^{\kappa} p^{\kappa-1}\tilde{q},$$

where $F = 2\Omega = 1.458 \times 10^{-4}\ s^{-1}$ and σ is a characteristic static stability ($\partial\theta_0/\partial\Pi$). The vertical independent variable scales as Π, say the depth of the tropopause, while the horizontal independent variable scales as λ_R, the Rossby radius of deformation, where $\lambda_R{}^2 = \sigma\Pi^2/F^2$.

When nondimensionalized, the NLB equation and the potential vorticity become:

$$\tilde{\nabla}^2\tilde{\Phi} = \tilde{\beta}\frac{\partial\tilde{\Psi}}{\partial\tilde{y}} + \tilde{\nabla}^2\tilde{\Psi} + \tilde{G}; \qquad G \equiv 2\left[\frac{\partial^2\Psi}{\partial x^2}\frac{\partial^2\Psi}{\partial y^2} - \left(\frac{\partial^2\Psi}{\partial x\partial y}\right)^2\right] \quad (a)$$

$$\tilde{q} = (\tilde{f} + \tilde{\nabla}^2\tilde{\Psi})\frac{\partial^2\tilde{\Phi}}{\partial\tilde{\pi}^2} + \tilde{B}; \qquad B \equiv \frac{\partial^2\Psi}{\partial\pi\partial x}\frac{\partial^2\Phi}{\partial\pi\partial x} + \frac{\partial^2\Psi}{\partial\pi\partial y}\frac{\partial^2\Phi}{\partial\pi\partial y} \quad (b) \qquad . \qquad \textbf{(4.1)}$$

G represents the nonlinear (ageostrophic) term in the NLB equation and B is the baroclinic component of the potential vorticity. For notational convenience, the tildes (~) will be dropped in subsequent equations.

The sum of (4.1a) and (4.1b) can be manipulated to produce a 2 dimensional Poisson equation for Ψ:

$$\nabla^2\Psi = \frac{\left[q + \nabla^2\Phi - f\frac{\partial^2\Phi}{\partial\pi^2} - (G+B) - \beta\frac{\partial\Psi}{\partial y}\right]}{\left[f + \frac{\partial^2\Phi}{\partial\pi^2}\right]} \qquad \textbf{(4.2)}$$

while the difference yields a type of 3-dimensional Poisson equation for Φ:

$$\nabla^2\Phi + (f + \nabla^2\Psi)\frac{\partial^2\Phi}{\partial\pi^2} = q + f\nabla^2\Psi + G - B + \beta\frac{\partial\Psi}{\partial y}. \qquad \textbf{(4.3)}$$

Inspection of (4.2) and (4.3) reveals that the forcing (r.h.s.) terms for both equations are functions of both Φ and Ψ making this system highly implicit in nature.

The PV inversion problem requires that both these equations be solved *simultaneously*. This is accomplished by treating the r.h.s. of each equation as a constant while inverting the elliptic operator. The newly obtained solution for one equation is used to update the r.h.s. of the other equation, which is in turn inverted. This constitutes a "cycle" in the solution algorithm. The cycle process is repeated until both fields (hopefully) converge on the correct solution which satisfies (4.2) and (4.3) to a specified accuracy.

4.3 Solution of the NLB System

With moderate forcing, either one of these equations is readily solved using a standard method such as successive over-relaxation (SOR). Solving the system as a whole, however, proves to be much more difficult. The nonlinear nature of the forcing in this problem (terms G and B) often means that small excursions from the actual solution produce locally large forcing. This provides a positive feedback which acts to drive the solution further from its attractor resulting in rapid divergence. The application of this balance model to the MCS regime is further aggravated by the extremely large shears and strong temperature gradients (and hence large PV gradients) generated locally by the deep convection. While, at least in principle, a balanced solution exists to this PV distribution, the nonlinear terms are so dominant that success in achieving convergence with the numerical method becomes very dependent on the initial guess. The initial nonlinear error often forces the solution out of its attractor basin within the first cycle.

For times when strong convection was not present, an adequate initial guess was simply the primitive equation solution interpolated onto the analysis grid. To the extent that a relatively unperturbed atmosphere is nearly in balance and the horizontal divergence is small, this would be expected to provide a reasonable starting point. In regions where deep convection *is* present, the atmosphere quickly produces strong divergent motions in the form of gravity waves. While the PE solution is still in reasonable balance in those regions removed from deep convection, local departures from the slow manifold are substantial, leading to rapid divergence.

To mitigate this problem of sensitivity to initial guess, an initial guess was employed which was a combination of the balanced solution at an earlier time and the PE solution at the current time. The boundary conditions were derived (by necessity) entirely from the current PE solution, while away from the boundaries the initial guess was weighted more heavily towards the balanced field from a previous time. A linear transition region of 3 points between the boundary and the interior was used to minimize spurious gradients. At some times an additional nine point Gaussian smoothing of the initial fields was required to achieve convergence. This hybrid initial guess was successful as long as the previous guess was in close temporal proximity to the current analysis time. Furthermore, during periods where domain-wide diurnal temperature changes were occurring, this method was applied only to the streamfunction since the geopotential was systematically changing over large areas.

Another consequence inherent in the solution of this inversion problem is a "ringing" as the system approaches convergence and oscillates between 2 solutions. This oscillation is damped by using an under-relaxation method. After the SOR iterative solver converges on a new solution at iteration τ, the updated forcing for the complementary equation is computed using a linear combination of the current(τ) and past (τ-1) solutions:

$$^{\tau}F_{forcing} = \lambda{}^{\tau}F + (1-\lambda)\,{}^{(\tau-1)}F \qquad \textbf{(4.4)}$$

where F =Φ,Ψ. The under-relaxation factor, λ, varied from about 0.8 for the first cycles to as low as 0.4 for the final few cycles. This under-relaxation on the first few cycles was useful in dampening out the positive feedback runaway behavior due to the initial guess error. Iversen and Nordeng (1984) found a comparable behavior with their family of balanced prognostic models. DE reported using a similar damping method in their diagnostic system.

In addition to the carefully constructed initial guess discussed above, a few other adjustments were necessary to ensure convergence. These modifications were necessary to maintain inertial stability ($PV \geq 0$) and static stability ($-\partial\theta/\partial\pi > 0$). The typical MCS environment is one of strong surface heating and anticyclonic synoptic scale flow, where these stability factors are frequently small (Maddox 1983; Cotton et al 1989).

As the storm occurred in an environment which ranged from weakly inertially stable to slightly unstable, storm-induced perturbation flows produced local regions where the PV was quite negative (~ -0.5 PVU). To maintain the ellipticity of the inversion problem, the PV must be a positive quantity (DE; Mcwilliams and Gent 1980). Therefore, PV fields used in the inversion were filtered such that PV values $q < 10^{-3}$ PVU were set to this small value. Since the inversion of the second order operator acts as a pronounced smoother, eliminating most of the fine-grained detail seen in the PV fields, these local changes would not be expected to have a significant impact on the resulting inverted fields (HMR).

The PE model results, and therefore the initial and boundary conditions used in the diagnostic solver, contained no static instability. (The strong surface heating in the model simulation produced a deep and well mixed convective boundary layer, $-\partial\theta/\partial\pi \sim 0$, with superadiabatic lapse rates in the lowest few model levels. These lowest model levels were not included in the diagnostic data sets.) During the first few cycles of the inversion process, unstable lapse rates ($\partial^2\Phi/\partial\pi^2 < 0$) would occasionally appear as the geopotential made relatively large adjustments to a balanced state, creating a numerical instability. When this occurred, the static stability was set to a very small positive value. As the solver converged to a balanced Φ solution this problem disappeared.

The ω, χ system, composed of the ω and continuity equations which was used to solve for the balanced divergent flow was comparatively easy solve. The ω equation is quite complex and implicit but linear while the continuity equation is also linear, simple in form and well behaved. These equations were solved in dimensional form as they appear in (3.22) and (3.24) in a manner analogous to that described for the Φ,Ψ system. The under-relaxation procedure described above was used to damp out ringing in the last few cycles. The initial guess fields were simply the PE model divergence and vertical motion consistent with the initial guess divergence and associated boundary conditions.

4.4 Boundary Conditions

Suitable lateral boundary conditions (BCs) for the inversion of observed PV distributions in a bounded region present a special problem. Balanced modeling studies, by design, generally have simple, well-posed boundary conditions. The winds (or equivalently, the streamfunction) and geopotential (or similar measure of mass distribution) at the boundaries are typically specified as a part of the steady-state background or basic-state flow. In particular, a horizontally-homogeneous resting basic state, as used by Hertenstein and Schubert (1991), permits trivial BCs. Similarly, Jaing and Raymond (1994) used a specified baroclinic basic state with boundary values held constant. Implicit to this approach is the assumption that the lateral boundaries are far enough removed from the region of interest that their contribution to the solution is negligible.

With observational and model simulation data, on the other hand, the concept of a background state is much fuzzier. Terrain variations and other surface inhomogeneities may cause time-dependent circulations near boundaries which are unrelated to the phenomena of interest. Further, the "background state" itself may not be perfectly balanced, and perturbations from balance are not generally confined to the center of the domain. Boundary conditions that contain only the slow manifold component of the observed data fields are obviously the ideal choice, but this slow manifold component is indeed exactly what we are trying to obtain!

One solution is simply to use the observed fields which contain both fast manifold and the desired slow manifold components. While this can be done with the geopotential, the streamfunction is defined as the derivative of a nondivergent wind field, and as such is not a measurable quantity. DE proposed a method to define an approximate streamfunction along the lateral boundaries from the observed winds, which will be outlined here.

Partitioning the horizontal observed winds $\mathbf{v}_t$ into the component divergent $\mathbf{v}_\chi$ and nondivergent $\mathbf{v}_\Psi$ vector fields and applying the 2-dimensional version of the divergence theorem to each field gives

$$\int_A \nabla \cdot \vec{v}_t da = \int_A \nabla \cdot \vec{v}_\chi + \cancelto{0}{\nabla \cdot \vec{v}_\Psi} da = \oint_S \vec{v}_t \cdot \hat{n} ds \qquad \textbf{(4.5)}$$

where S is a closed contour bounding the surface A. Using the nondivergence of $\mathbf{v}_\Psi$ and its definition in terms of Ψ from (3.10) yields:

$$\int_A \nabla \cdot \vec{v}_\Psi da = \oint_S \vec{v}_\Psi \cdot \hat{n} ds = \oint_S -\frac{\partial \Psi}{\partial s} ds = 0. \qquad \textbf{(4.6)}$$

Now, using (4.5), we may define a "divergence velocity" V_0:

$$V_0 = \frac{\oint_S \vec{v}_t \cdot \hat{n} ds}{\oint_S ds}. \qquad \textbf{(4.7)}$$

V_0 represents an "average" divergent wind for each level. This velocity must be removed from the normal component of the model wind field along S to make the 2-dimensionally domain-wide flow nondivergent.

Combining these results and using the Mean Value Theorem of calculus yields:

$$\oint_S \left(-\frac{\partial \Psi}{\partial s} + V_0\right) ds = \oint_S \vec{v}_t \cdot \hat{n} ds, \qquad \textbf{(4.8)}$$

or

$$\frac{\partial \Psi}{\partial s} = -\vec{v}_t \cdot \hat{n} + V_0, \qquad \textbf{(4.9)}$$

since (4.8) holds true for any arbitrary surface A bounded by S. Now, integrating (4.9) along the contour S defines a streamfunction along the boundary. This is *not* an exact solution since the mean value V_0 has been used in place of the (unknown) divergent wind component at each point. What (4.9) *does* assure is that the closed-contour integral of Ψ along S is zero.

A boundary condition for Ψ is also required for the horizontal boundaries at the top and bottom of the domain. One possibility, (DE) is to use the observed geostrophic streamfunction Φ/f. With flows having a large curvature, this may be a poor choice. In this situation it is possible to obtain a streamfunction which shows much better agreement with the observed winds. Using the vorticity, $\zeta = \mathbf{k} \cdot \nabla \times \mathbf{v}$, computed from the observed winds and using the boundary conditions consistent with (4.9), the Poisson equation:

$$\nabla_h^2 \Psi = \zeta \qquad \textbf{(4.10)}$$

may be inverted to give a streamfunction representation of the horizontal boundary winds which has vorticity everywhere equal to the observed wind field.

For the χ, ω balanced divergent wind inversion, boundary conditions consistent with the PE model are somewhat harder to derive since a relationship similar to (4.9) does not exist for the divergent wind. Further, a fundamental assumption is made that, *to first order*, the nondivergent winds represent the balanced flow and the divergent winds represent the unbalanced flow. However, in general, to maintain mass continuity in a domain-wide sense, some divergent wind is required at each level. A boundary condition of $\chi = 0$ at the lateral boundaries was used for these calculations, which allows the freedom for the integral in (4.5) to be satisfied. This boundary condition does eliminate any tangential component of the divergent wind field along the boundaries. This side effect was found to be negligible when interpreting the results in the interior of the domain.

The upper and lower horizontal boundaries present more of a problem. The upper boundary is above 100 mb, well into the lower stratosphere. Due to the very stable nature of the stratosphere, it is reasonable to assume that most of the vertical motion seen there is due to gravity waves, and a rigid lid (ω=0) is justified. The bottom of the analysis domain (a constant pressure surface) is *not* the earth's surface. Hence a boundary condition of ω=0 is *not* justified here. Indeed, a significant amount of the convergence feeding the convective updrafts is found very near the surface where the high θ_e values are found. These updrafts are responding in large measure to the diabatic heating, which *is* represented in the balanced ω equation, and therefore should be included. Also, since the atmospheric environment is well mixed and therefore almost neutral in the lower levels, significant gravity wave radiation is at a minimum there. For these reasons, a nonzero vertical velocity $\omega = f^{cn}(x,y)$ was specified at the lower boundary. To derive $\omega(x,y)$ at the lower boundary, (3.22) was integrated downward using $\omega_{top} = 0$ and the 2-dimensional divergence obtained from the PE model. This divergence was also used as the first guess in the cyclic-iteration procedure.

Chapter 5: Primitive Equation Simulation of the 23-24 June, 1985 MCC

5.1 Introduction

In the past several chapters, we have been concerned with the MCC in the context of balanced dynamics. In a somewhat different vein, this chapter is concerned with a particular case study: the PE numerical simulation of an MCC. In Section 5.2, the PE model used in this simulation of the 23-24 June, 1985 MCC over Iowa and Missouri will be described, particularly those aspects of the model, such as the cumulus parameterization, of importance for this simulation. Note is also made of the model features which have been modified from the standard model configuration. Section 5.3 contains a description of the initial conditions specified for this simulation, in particular the spatially variable upper-air and surface fields. In Section 5.4, the synoptic situation pertaining to the simulated MCC event will be reviewed. In Section 5.5, the simulation in the early stages of storm development and mesoscale organization will be examined. In Section 5.6 we will consider the mature and dissipating stages of the simulated storm, and compare the results to observations and other MCS studies.

5.2 Basic Simulation Structure

The simulation of the 23-24, June 1985 MCC was performed using RAMS (Regional Atmospheric Modeling System), a nonhydrostatic primitive-equation model. The salient features of the model as it is applied to this particular study will be discussed here. For a more thorough description of the model see Pielke et al. (1992).

Table 5.1. *A summary of the RAMS model configuration.*

	Grid #1	Grid #2	Grid #3
grid spacing (Δx)	75 km	25 km	8.33 km
grid dimensions (x $\times$ y) km	4050$\times$3225	1975$\times$1600	833.3$\times$633.3
number of points (x $\times$ y)	55 $\times$ 44	80 $\times$ 65	101 $\times$ 77
vertical levels	32	32	32
time step (Δt)	90 s	45 s	22.5 s
convective parameterization	none	none	level 2.5 w

5.2.1 Space and time configuration

The 24 hour simulation started at 1200 UTC, June 23, 1985 (23/1200), terminating at 1200 UTC, June 24 (24/1200). The simulation used the two-way interactive multiple nested-grid capability of RAMS. Table 5.1. contains a summary of the various grid properties. The simulation was initialized with two grids. After 9 hours of simulation time a third grid was added in the region of the storm to better simulate the smaller-scale flow features. The coarsest grid (Grid #1) had a grid spacing of 75 km with 55 points E-W and 44 points N-S. The first nested grid (Grid #2) had a 25 km grid spacing with 80 points E-W and 65 points N-S. The second nested grid (Grid #3) had a grid spacing of 8.33 km with 110 points E-W and 77 points N-S. Fig. 5.1 shows the relative geographic locations of the grids.

The RAMS model uses a terrain-following (σ_z) vertical coordinate system, defined as:

$$\sigma_z(z) = \frac{(z - z_b)}{(z_t - z_b)} z_t \qquad \textbf{(5.1)}$$

where $z_b(x,y)$ is the terrain height above sea level (ASL), and z_t is the (specified) model top (in this case 20 km). All three grids contained 32 vertical levels with a stretched grid spacing (no nesting was done in the vertical). For a grid column where $z_b = 0$ (i.e., sea level) beginning at the surface, model levels were separated by 175 meters, each succeeding grid spacing being a factor of 1.1 times larger, until a maximum grid spacing of 1000 m was

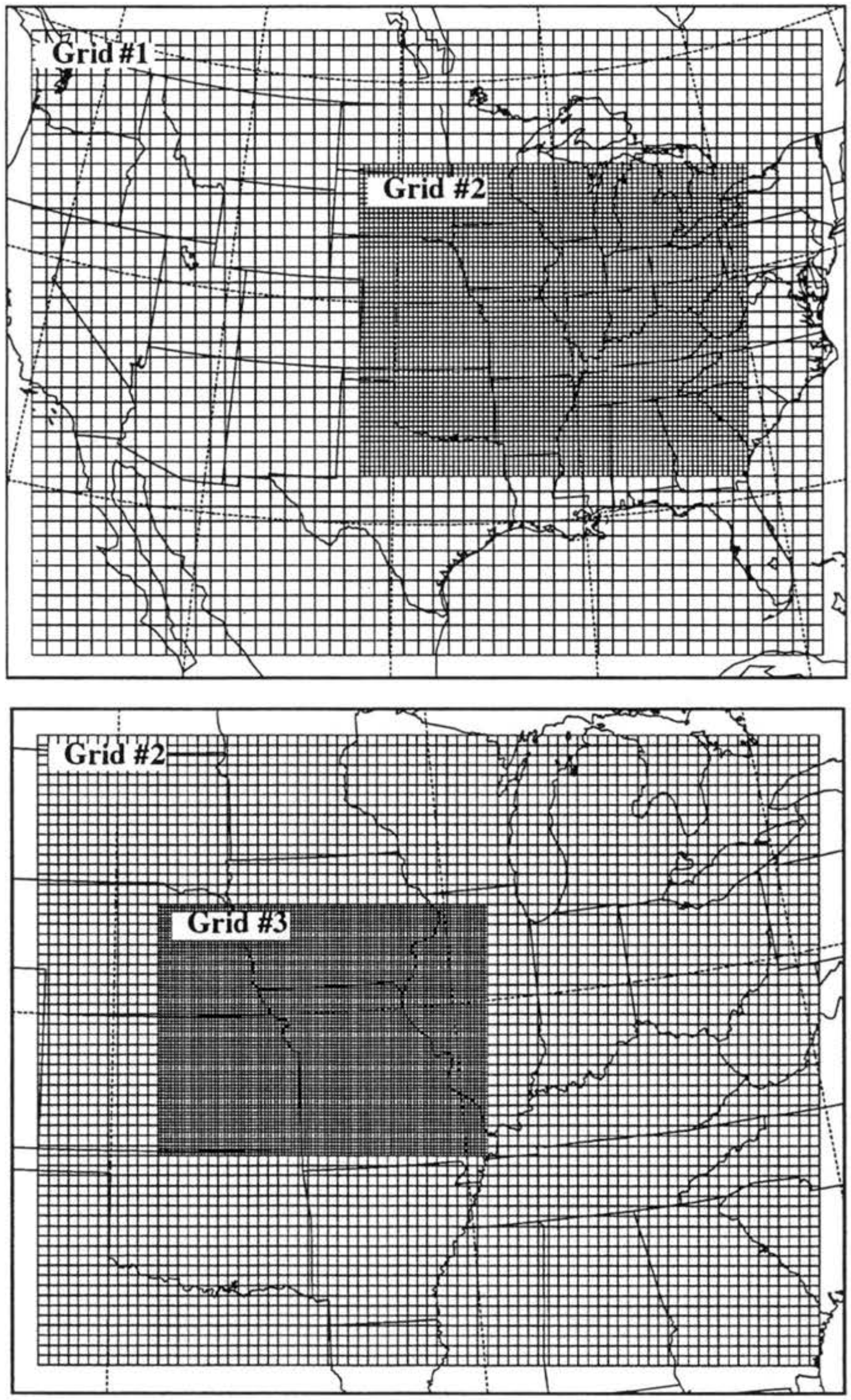

Fig. 5.1. *Relative locations of the model grids. The upper panel depicts Grid #1 (75 km Δx) and Grid #2 (25 km Δx). The lower panel depicts Grid #2 and Grid #3 (8.33 km Δx). The interior points of Grid #2 constitute the horizontal domain on which the balance diagnostics are performed. The convective parameterization was active on Grid #3 only.*

reached. From this level to the top of the domain, the vertical grid spacing was kept constant at 1000 m to the model top. $\Delta\sigma_z(z)$, the vertical grid spacing in the terrain-following coordinate system, is horizontally homogeneous. Hence, for grid columns where $z_b(x,y) > 0$, the actual vertical grid spacing (Δz), as determined by the relationship in (5.1), will be somewhat less.

The time step on Grid #1 was limited by the necessity to resolve buoyancy oscillations and was set at 90 seconds, a much smaller time step than would be required to satisfy the Courant-Friedrichs-Levy (CFL) criterion (Pielke 1984). Grids 2 and 3 require a somewhat smaller time step due to the small grid spacing. RAMS requires that the ratio of nested-grid time steps to a parent-grid time step be an integer. Hence each nested grid time step was half the length of the parent-grid time step, giving a Grid #2 time step of 45 seconds and a Grid #3 time step of 22.5 seconds.

5.2.2 Boundary Conditions

In a variably-initialized simulation, boundary conditions are time varying. To handle the upper and lateral boundaries, a Newtonian relaxation technique was used. Intermediate data sets at 12 hour intervals were created by the same method used to produce the initial fields. From time-weighted averages of these intermediate data sets and the initial fields, tendency terms were computed and applied to points near the boundaries, "nudging" them to the observed values. This technique was applied to the top and lateral boundaries of the coarsest grid and to the top boundaries of the nested grids.

5.2.3 Surface Topography

The surface topography (terrain elevation) was obtained from RAMS global and U.S. data sets. Grid #1 used terrain heights from the global 10 minute resolution data set, while the heights on Grid #2 were obtained from the U.S. data set at 30 second resolution. The terrain heights on Grid #3 were interpolated from Grid #2. This was required since Grid #3 was spawned after the model was initialized. The terrain calculations for Grid #1 used straight averaging while the topography specification on Grid #2 employed silhouette

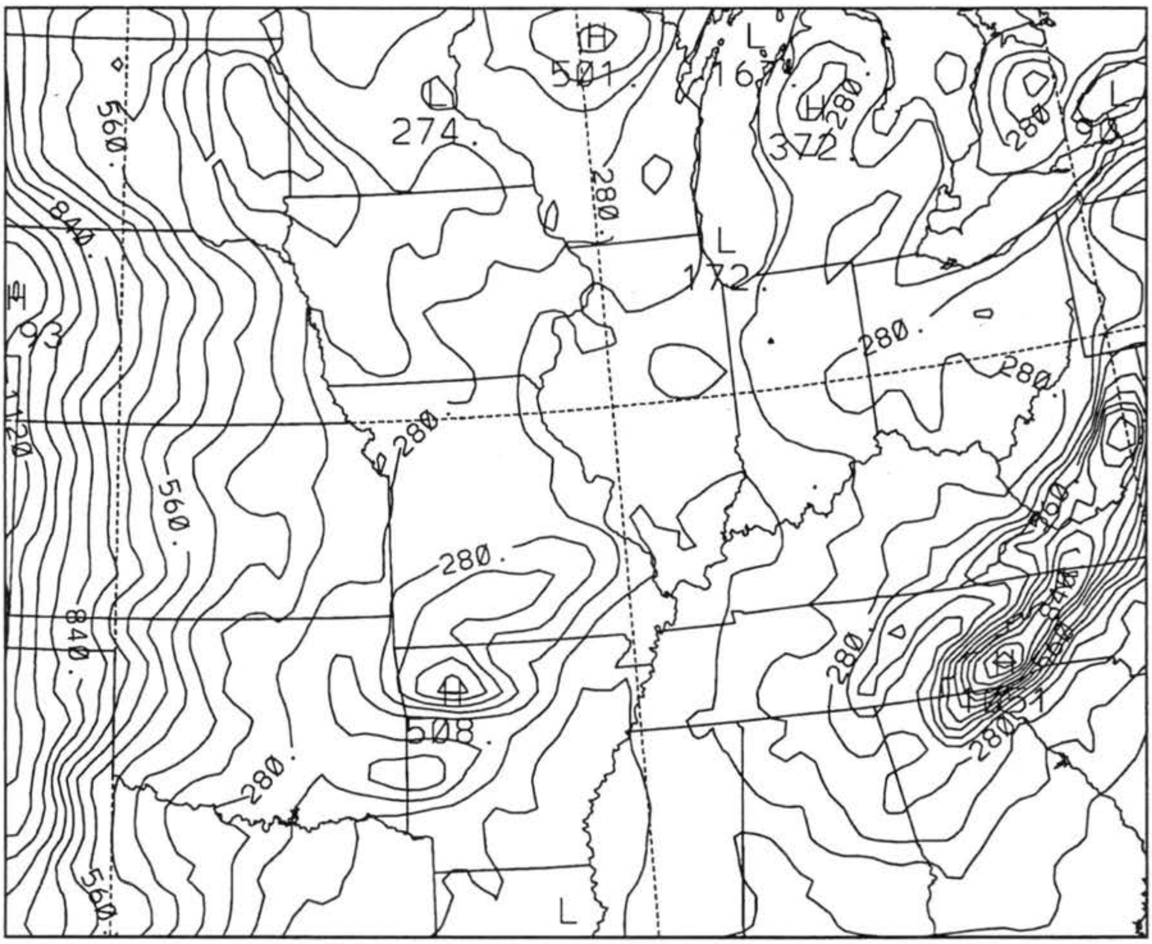

Fig. 5.2. *Topography for Grid #2, contour interval of 70 m. The highest point in the domain, in western Nebraska, is 1193 m and the lowest is sea level, 0 m.*

averaging. This permitted better resolution of topographic inhomogeneities over the Great Plains on Grid #2 while maintaining relatively smooth topography on the coarse grid. The topography for Grid #2 is shown in Fig. 5.2.

5.2.4 Cumulus parameterization

One of the inherent problems in any modeling of dynamical systems on a finite grid is the inability of a model to explicitly capture processes which occur at scales less than the model grid spacing. To maintain a reasonable degree of certainty in regards to energy balance in a system which includes energy sources, some method must be made available to transfer energy from resolvable motion to sub-grid scale motion. This is done by parameterizing the loss terms in a manner consistent with the physics on which the model is based.

While the cascade of energy is usually considered as proceeding from larger to smaller scales, the converse also occurs. For example, Pedlosky (1979) demonstrates that for the quasigeostrophic system, the constraint of total energy and total enstrophy conservation requires that energy transfer downscale by nonlinear processes must be accompanied by a significant transfer of energy to larger scales.

Atmospheric thermal convection is a more intuitive example of a significant source of energy for fluid motion which is generated at small scales and perturbs the larger scale circulation patterns. The scale of convective motions is on the order of a kilometer. To adequately resolve such motions, a finite-difference model would require a grid spacing of a few hundred meters. While simulations at such resolution have been performed for a limited grid size and length of time, the size and duration of an MCS makes this resolution unfeasible when simulating such a storm. For this reason, parameterization of convection was necessary.

The Level 2.5w Convective Adjustment Scheme (Weissbluth and Cotton, 1993) was employed for this simulation. This convective parameterization was designed for use with grid sizes from 5 to 50 km, a scale at which many convective parameterization schemes are not applicable. The level 2.5w scheme incorporates an extension of the Mellor and Yamada (1974) level 2.5 turbulence closure based on vertical velocity variance, $\overline{w'w'}$, rather than turbulence kinetic energy (TKE). In this scheme, $\overline{w'w'}$ is treated as a prognostic variable which is advected by the model's resolved winds.

This convective parameterization consists of two parts; a microscale vertical diffusion scheme which controls sub-grid scale vertical mixing, and a cumulus-scale updraft/downdraft component which is driven by a one dimensional cloud model. In the absence of deep convection, the vertical diffusion component provides tendencies to the prognostic variables proportional to gradients in their sub-grid scale vertical fluxes. When the scheme has determined that deep convection is present, additional tendencies are fed into the host model. The one dimensional cloud model produces a vertical profile for each column, and at each time step, tendencies are computed for the temperature and the various microphysical species. In this manner, the host model is "nudged" towards the evolving one-dimensional cloud profile on a time scale determined by, among other things, cloud-core fractional coverage of updrafts and downdrafts, the profile of $\overline{w'w'}$, and differences between in-cloud and environmental values of the variable under consideration.

Another rather unique feature of this parameterization is its ability to directly provide a source of hydrometeors for the host model, in contrast to other schemes (e.g., Kuo 1965, 1974; Arakawa and Schubert 1974; Fritsch and Chappel 1980) which simply moisten the host model, requiring nucleation processes to occur there.

5.3 Initialization

The initial fields were obtained by compositing several different data sets. The large scale background features were obtained from European Center for Medium-Range Forecasting (ECMWF) gridded data sets. These global data sets, used to initialize the ECMWF forecast model, have a horizontal latitude-longitude grid spacing of 2.5°, analyzed on constant-pressure surfaces of 1000, 850, 700, 500, 300, 200, and 100 mb. To resolve finer-scale features, rawinsonde and surface observation data sets were also analyzed.

The RAMS data assimilation is performed using objective analysis on constant isentropic surfaces. The various upper-air data mentioned above are first vertically interpolated linearly in a pressure coordinate (p^{κ}, where $\kappa = R/C_p$). Next, the Barnes (1973) objective analysis scheme is used on 48 specified θ surfaces ranging from 282°K to 500°K to create a regular gridded data set in latitude-longitude-θ, with a horizontal spacing of 0.5°. The surface atmospheric data were handled in a similar manner, with the pressure and Montgomery streamfunction being obtained from the first isentrope above the ground.

This composite initialization is then interpolated onto the RAMS (x,y,σ_z) model grid, where all fields are adjusted to hydrostatic balance. No attempt is made to introduce any further balance in the initial fields.

The choice of potential temperature as a vertical coordinate in the data assimilation process has several advantages. In regions of strong baroclinicity (e.g., fronts) where horizontal gradients of θ are large, this coordinate yields good resolution. There is a more fundamental, yet less intuitive, advantage of the isentropic coordinate system. In regions of sloping isentropes, short-wavelength features in cartesian coordinates become longer wavelength features in isentropic coordinates (Pielke et al. 1992). Since the built-in scale filtering of the objective analysis retains more information at longer wavelengths, this coordinate yields a better resolved analysis when the data are re-interpolated into cartesian space.

A significant disadvantage of the isentropic coordinate is poor resolution in a weakly stratified environment. In a deep, well-mixed convective boundary layer, the lowest levels are superadiabatic and the one-to-one relationship between θ and physical height is lost. The 23-24, June simulation was initialized at 23/1200, just after sunrise local time in the central U.S. when the nocturnal boundary layer was still largely intact. Hence, this potential weakness in the RAMS assimilation methodology was not a concern here.

5.3.1 Surface initialization

The Tremback-Kessler (1985) soil model was used in this simulation, with 11 vertical levels located from -1 cm to -1 m. The soil model predicts both surface heat and surface moisture fluxes, working in concert with the Chen and Cotton (1987) radiation model, which updated radiative fluxes every 900 s.

During the summertime, diurnally varying surface heat fluxes play a predominant role in the evolution of the boundary layer and consequent destabilization of the atmosphere. The details of the surface fluxes are, in turn, strongly effected by the imposed initial conditions on soil temperature, soil moisture, soil texture, and vegetation type and coverage. Unfortunately, complete and accurate data sets for the initialization of these surface values are either not documented (soil texture, soil temperature) or not available in an easily ingestible form (soil moisture, vegetation type and coverage). Soil texture information is simply not available for the U.S. as a whole. Hence, a constant soil type (clay loam) was used for this simulation. As soil initial temperature is also not readily available, the initial soil surface temperature was initialized 3°C colder than the lowest (surface) atmospheric level, a typical offset just after sunrise (Sellers 1965).

Some data were available concerning vegetation type and coverage and soil moisture. A vegetation type data set was obtained from NCAR which was composed of 11 primary vegetation types at a 5 minute latitude/longitude resolution. These data are interpolated onto the model grids and then converted to the vegetation classification used in the model (RAMS uses 18 vegetation types). Within this classification, various quantities such as leaf-area index and shaded soil fraction are diagnosed.

Soil moisture information was obtained from the USDA publication, Weekly Crop Bulletin, which contains weekly maps of soil moisture index for the continental US. The soil moisture index data were manually transferred to a latitude/longitude gridded data set at 1° resolution. This data set was then filtered and interpolated onto the model grid where it was converted, using a simple linear transformation, into a soil moisture percentage. This transformation was admittedly ad-hoc, but it produced credible soil moisture variations and gradients which were in good qualitative agreement with the soil moisture index values.

Several sensitivity tests were performed with different values of initial soil moisture and initial soil temperature/surface atmospheric temperature offsets. After a few hours of simulation, the model showed little sensitivity to a reasonable range of initial soil temperature offsets. An exception to this was found in areas where a large temperature deficit was combined with very wet soil. In these regions, the Bowen ratio (sensible heating/latent heating) is very low, resulting in unreasonably cool surface temperatures, low-level stratus cloud and fog.

The model was much more sensitive to soil moisture initialization, as might be expected from the preceding discussion. Large gradients of soil moisture created spurious mesoscale circulations of the classical sea-breeze type, while exceptionally dry soils produced unrealistic boundary layer depths. The combination of large moisture variations with topographic effects, especially along the Front Range of the Rocky Mountains produced pronounced slope flows which were not seen in the observations. The most realistic circulations and surface temperature fields were found with the relatively dry initial values for the variable soil moisture.

5.4 Storm Description

The MCS outbreak which occurred over the central Great Plains on June 23-24, 1985 was comprised of two storms. The larger of the two storms, and the focus of the modeling study, was an MCC which initiated as a line of convection over south-central Iowa and eastern Nebraska at around 23/2030 (all times UTC), with MCC initiation later that afternoon, at around 23/2300 (Augustine and Howard 1988). The smaller and more western of the two storms initiated in west-central Kansas. This faster moving storm propagated SSE directly over the PRE-STORM[1] surface observation network in south-central Kansas and Oklahoma. By 24/1000 the storm was dying out over the Oklahoma panhandle and northern Texas. It is interesting to note that MCVs were observed in both the small, western MCS (Johnson and Bartels 1991) and the larger MCC (Meitín and Cunning 1985), even though the environments were considerably different.

5.4.1 Great Plains synoptic situation on 23-24 June, 1985

A vigorous low pressure system over Hudson Bay, with closed contours up to 200 mb, was the dominant synoptic scale feature over North America for the period of June 23/24. Another low pressure system moved into the Pacific Northwest digging a trough along the western U.S. coast. The north-central U.S. was under a weak midtropospheric ridge which progressed from central Montana at 23/1200 to the central Dakotas by 24/1200. Winds near the ridge crest (Fig. 5.3b) were westerly and fairly strong (13 to 23 m s^{-1}) at 500 mb with the jet located along the U.S.-Canada border. The flow through the ridge crest at 300

1. PRE-STORM (Preliminary Regional Experiment for Stormscale Operational Research Methodology) was a multi-agency field program conducted in May and June, 1985 in Oklahoma and Kansas to study convective storms on the mesoscale (Meitín and Cunning 1985).

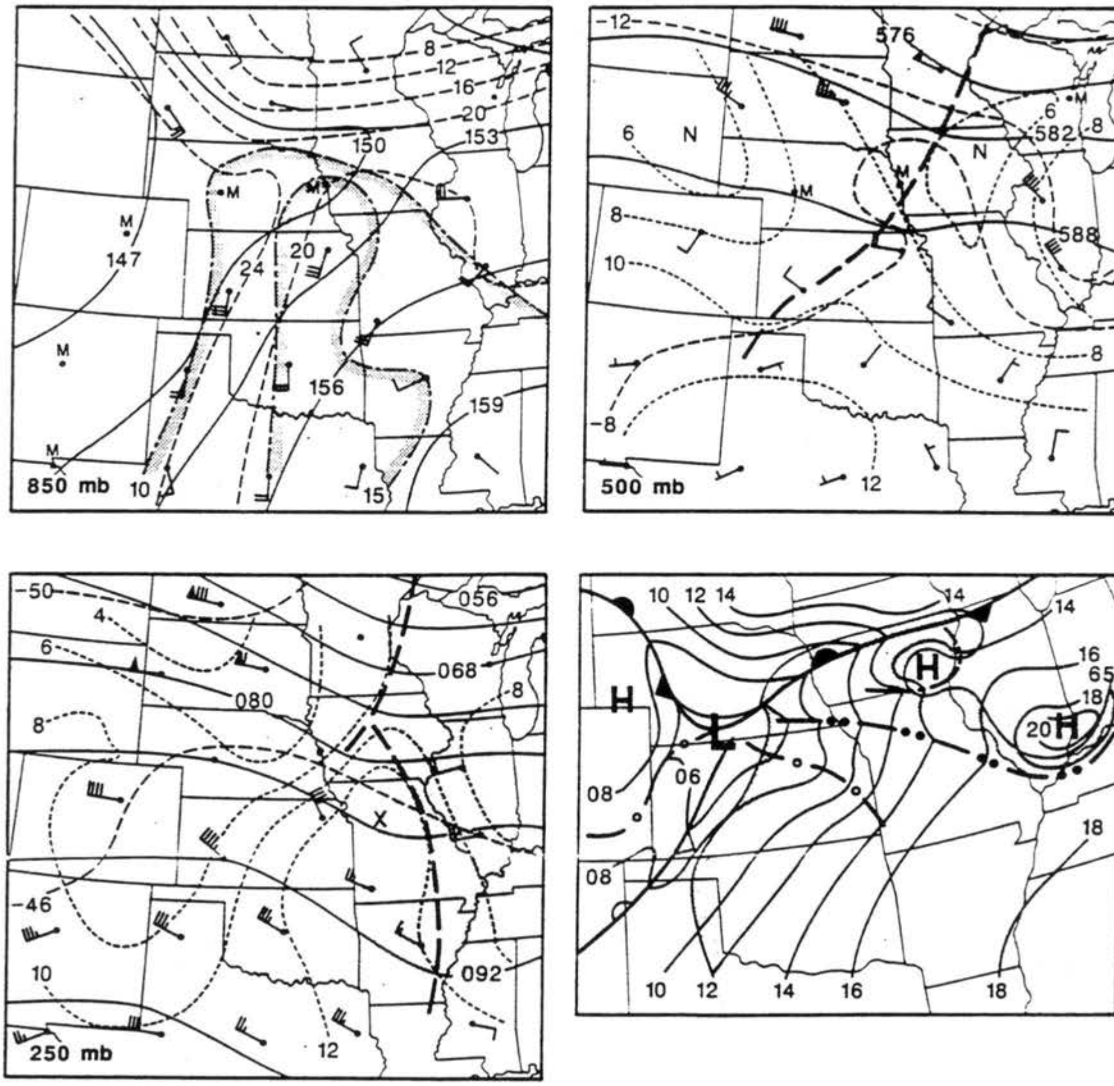

Fig. 5.3. (a) 850 mb height temperature and dewpoint temperature at 24/0000. Winds are in knots (full barb indicates 10 kt). Height contours (solid) are in decameters and (dashed) temperature contours have 4°C increments.Regions in which dewpoint temperatures exceed 10°C and 10°C are shown. (b) Corresponding analysis of 500 mb height, temperature and absolute vorticity fields. Winds, height and temperature contours, as in Fig. 5.3a. Vorticity (× 10^{-5} s^{-1}) contours (short-dashed), with N denoting minimum in absolute vorticity. (c) As in Fig. 5.3b, except at 250 mb, and height contours now -1000 dm. Thick dashed line shoes location of short-wave trough. X denotes absolute vorticity maximum. (d) Sea level pressure (mb -1000) and surface frontal analysis at 24/0000. Dash-dot-dot pattern indicate outflow boundaries. Shaded line indicates region where dewpoint temperatures exceed 18.5°C. (from Stensrud and Maddox 1988.)

mb exceeded 45 ms^{-1}. During this period, winds over the northern and central Rockies backed as the west-coast trough progressed eastward.

Further south, over the central Great Plains, the flow through the weak mid-level ridge was much weaker with typical speeds less than 10 m s^{-1}. The winds above 500 mb in this region, however, increased significantly with height (Fig. 5.3c), giving a large vertical shear in the upper troposphere. A significant horizontal N-S velocity gradient also existed, with 500 mb winds increasing from less than 5 m s^{-1} over southern Missouri to almost 25 m s^{-1} over central Minnesota, resulting in a weakly inertially stable to slightly unstable environment over the MCC genesis area. A weak shortwave trough passed through the ridge over South Dakota and Nebraska during the late afternoon and evening of June 23. Stensrud and Maddox (1988) suggest that this shortwave feature acted as a focus and intensification mechanism for the storm over Iowa and eastern Nebraska, since differential vorticity advection would provide favorable lower-tropospheric vertical motion.

Another important synoptic feature during June 23-24 was persistent strong southerly flow at 850 mb (Fig. 5.3a), a consequence of anticyclonic flow around a low-level high-pressure system centered over southern Alabama. Recall from Chap. 1 that this LLJ feature is frequently observed during periods of strong convection over the southern and central Great Plains and acts to transport moisture from the Gulf of Mexico well into the central U.S. By 24/0000, dewpoint temperatures (T_d) at 850 mb exceeded 10° C over all the south-central states. A tongue of even more moist air (T_d > 15° C) and strong southerly winds (> 15 m/s) extended over eastern Texas and Oklahoma and into the storm initiation region in SE Iowa and SW Nebraska.

A surface analysis (Stensrud and Maddox, 1988) valid at 24/0000 is shown in Fig. 5.3d The front, extending through Nebraska, Iowa and Illinois, had been in almost the same location in Iowa for at least the preceding 12 hours, and had slowly sagged southward into south-central Nebraska from its location along the South Dakota/Nebraska border 18 hours earlier. South of the front, maximum temperatures ranged from 32°C to 39°C in Kansas and Oklahoma. T_d ranged from 5°C west of the dryline in far western Kansas to 24°C in eastern Kansas. While mid-afternoon surface temperatures were not much cooler north of the cold front, the air mass there was significantly drier with T_d mainly in the single digits.

During the daylight hours of 23 June the frontal boundary was the focus for convection from eastern Nebraska to Illinois and Indiana. Convection started along and south of the front in north-central Nebraska around dawn and quickly developed eastward along the frontal zone. In their detailed mesoscale analysis, Stensrud and Maddox found a well-defined outflow boundary and meso-high extending from Nebraska to Michigan. In central and southern Iowa, convection occurred sporadically throughout the day. Hail of diameter greater than 1 cm fell in central Iowa about 2 hours after sunrise. By mid-morning, hail up to 4 cm in diameter and winds exceeding 35 m s^{-1} were reported in several locations in southern Iowa. After a brief lull around noon, convective activity again increased along the front. In the mid to late afternoon tornados were reported at several locations along the frontal boundary. Local flooding occurred south of Des Moines in the late afternoon with precipitation rates over 10 cm h^{-1}. About 200 km west at this time, numerous tornadoes were reported near the Iowa-Nebraska border as well as three lightning-related fatalities. This line of severe convection, intensifying and spreading southwest into Nebraska, achieved MCC status by 2300 UTC.

As the MCC slowly propagated south and east during its 9 hour lifetime, the system lost much of its initial linear organization. At 24/0530 NMC WSR-57 radar summary charts depict echoes extending from east-central Kansas across central Missouri and into east-central Illinois. By 0730 UTC June 24, the southernmost extent of the storm was just north of the Missouri/Arkansas border, with radar summary charts indicating detectable echoes over more than half of Missouri, stretching westward into SE Kansas. In Illinois, a smaller convective system had split off from the eastern end of the line, drifting east over east-central Illinois. At about this time the storm was starting to significantly weaken in intensity. By 24/1030, precipitation from the storm had largely ceased, though the remnant cloud shield was still visible for several hours.

Further to the west, a dryline formed and tightened in western Kansas during the late morning of 23 June. In contrast to the Iowa-Missouri border area, this region was experiencing large-scale subsidence, which helped to suppress convective initiation (Stensrud and Maddox 1988). By 23/2000 surface heating had sufficiently destabilized the boundary layer and convection fired along the dryline. Analysis of satellite images shows that by 12/2300 an almost continuous line of convection ran from NE New Mexico along the dryline in western Kansas and then extending along into Nebraska and joining the prefrontal convection in S Iowa. The convection along the dryline eventually formed the smaller, western MCS.

5.5 The 23-24 June MCC PE Simulation: Genesis Stage

Unlike other PE simulations of MCSs (e.g., Zhang and Fritsch 1987,1988; Zhang et al. 1989) the paramount desire in this simulation was not to reproduce results in almost exact agreement with observations. Here, the ultimate purpose of the PE simulation was to provide a data set which would be as tractable as possible to the balanced flow diagnosis. While it is desirable to have as good agreement as possible with the observations, the simulation structure optimal for the PV inversion by necessity precludes the simulation of some of the observed meteorological features which were observed. Within these constraints, the simulation was found to verify well with the observations. These practical limitations on the simulation structure will be outlined below.

In terms of the invertibility problem, probably the greatest restriction on the data set is the need for reasonably balanced conditions at the lateral boundaries throughout the simulation. As discussed in Section 4.3, the model winds and geopotential at these boundaries are used to formulate boundary conditions for the Ψ,Φ solver. The global nature of the inversion of (4.2) and (4.3) results in the boundary conditions having an effect on the solution well into the interior of the domain. The streamfunction and geopotential values specified at lateral boundaries are an inherent part of the balanced solution and the integrity of that solution rests partly in the use of boundary conditions relatively free of gravity wave motions. For this reason, convection was allowed only on Grid #3, while the inversion was performed on Grid #2. The grid structure was designed such that all Grid #2 boundaries were separated from Grid #3 by a distance significantly greater than the Rossby radius λ_R, this length being an e-folding scale or "radius of action" for boundary effects (Hoskins et al. 1985). The desired result is that the strong fast-manifold motions induced by the simulated MCC are largely contained well into the Grid #2 interior.

Aside from convection, fast-manifold gravity-wave behavior is induced by other agents (such as the Rocky Mountain orography) on the coarse grid outside of Grid #2. Due to the communication between grids, such gravity wave motions are contained in the Grid #2 boundary fields, but again the distance from the boundaries to the MCC should minimize these boundary effects in the region of greatest interest.

A consequence of restricting convection to Grid #3 is that observed convection occuring outside the region spanned by Grid #3 was not reproduced in the simulation. Most significantly, this means that the more western MCS of 23-24 June was not simulated. Since this storm occurred near the western boundary of Grid #2, its unbalanced flow would certainly have seriously effected the boundary wind and thermal structure.

To the extent that the western MCS might have had dynamical impact on the eastern MCC, this may be seen as a shortcoming of the simulation. One of the most common interactions between neighboring convective systems occurs in the convergence zone created when downdraft-driven outflow boundaries collide (Purdom 1982; Schreiber 1986). Based on this knowledge, forecasters for the OK-PRESTORM project on June 24, 1985 had *incorrectly* predicted the onset of new convection as the outflow boundaries from the two storms collided in eastern Kansas. Stensrud and Maddox (1988), studying the mesoscale circulations from the two storms, determined that the main interaction was upper tropospheric compensating subsidence induced by both convective systems which produced a vertical motion field suppressing the incipient convection in the convergence zone. Apparently, the upper- and lower-tropospheric interactions in this case were mutually compensating, the net effect being neutral. From this viewpoint, the absence of the western MCC does not constitute a significant compromise in the simulation of the eastern storm.

In addition to the MCS in Kansas and Oklahoma, scattered convection occurred in the late afternoon in southern Illinois, eastern Colorado, Texas, and elsewhere. Most of this convection was transient, and by about 24/0200 IR satellite images show that the two mesoscale systems were the only significant convective systems in the central U.S.

Some temporal constraints were also placed on the simulated convection. This was done for two reasons. First, the RAMS initial wind fields do not necessarily satisfy mass continuity, i.e., the initial horizontal divergence field is incompatible with the initial vertical motion field (w = 0 everywhere). This results in spurious vertical motion fields as the model achieves continuity. These motions, though usually quite small and short-lived, can trigger the convective parameterization in an unrealistic manner. The second reason relates more to the PV inversion. As discussed in the last section, convection was occuring along the front in Iowa and Illinois from the early morning on. In sensitivity studies, capturing this morning convection confused the interpretation of the balanced flow during the upscale growth of the MCC. For these reasons the convective parameterization was not activated until 7 hours of simulation time. In an attempt to reproduce some of the low-level effects of this earlier convection, the soil moisture was enhanced in eastern Iowa and western Illinois, and the soil temperature was decreased in the top two model levels by 5°C, consistent with the perturbations observed in the surface model as the result of moderate precipitation. These modifications were done to Grid #3 when it was spawned at 23/1800, and were fed back onto the coarser grids via the grid interaction. No modifications were made to the atmospheric fields.

5.5.1 Storm initiation

The deep convective parameterization was activated at 23/1900. Fig. 5.4 shows the surface θ_e field and horizontal winds at this time, along with the cold front and surface low pressure center. The tongue of high-valued θ_e air is quite apparent in this figure, with values of $\theta_e \geq 350$°K extending from the maximum in extreme SW Iowa down through eastern Kansas and into central Oklahoma. The LLJ also corresponds with this θ_e maximum, acting as an agent in maintaining and reinforcing the high surface θ_e values. Recall from Chapter 1 that both of these attributes are typical of the MCC environment (Maddox 1983; Wetzel et al. 1983). The location of the surface low pressure center along the Kansas-Oklahoma bor-

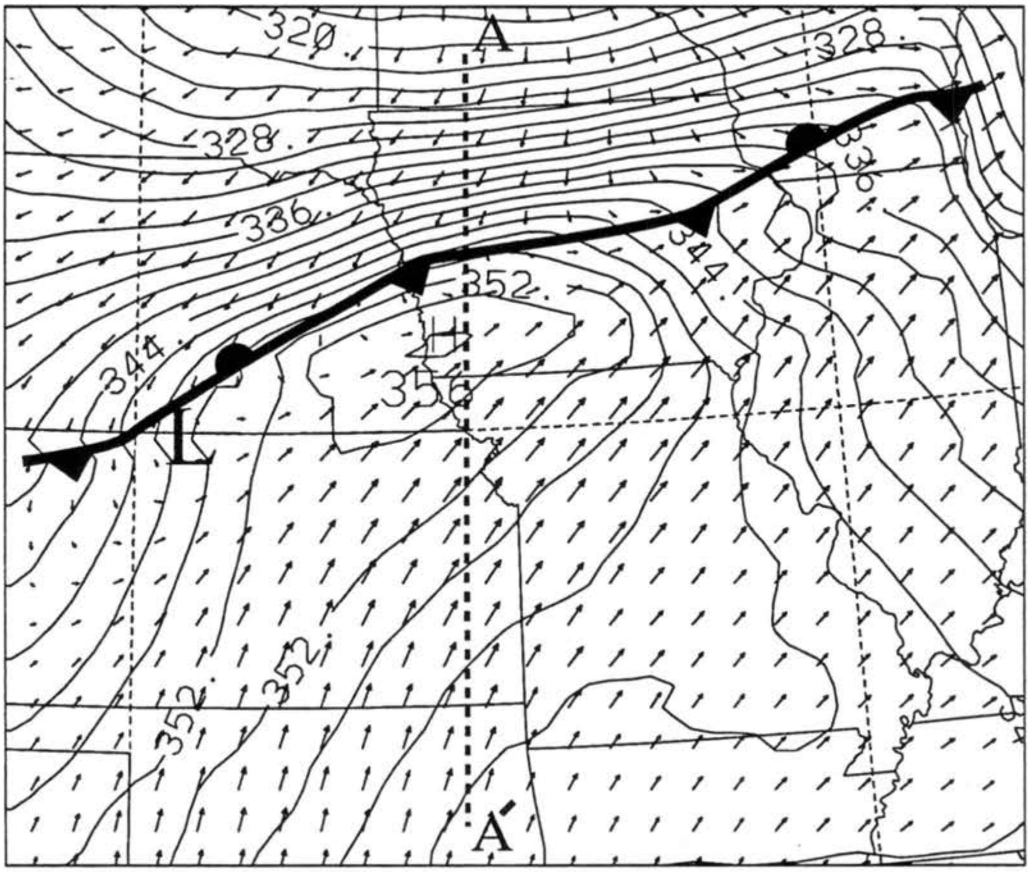

Fig. 5.4. *Wind vectors and contours of equivalent potential temperature at the surface at 23/1900. The contour level for θ_e is 2°K and the maximum wind vector in the figure corresponds to 8 m s^{-1}. The bold* **L** *indicates the location of the surface low-pressure center.*

der agrees fairly well with the 23/2100 mesoscale analysis of Johnson et al. (1989, see their Fig. 1) and is somewhat south compared to the NWS 23/1800 surface analysis. The model circulation around the low is not as closed and cyclonic as was observed, perhaps because the observed low-level flow was being deflected northward upon colliding with the outflow from the earlier convection in SW Iowa (see Fig. 5.3d).

By 23/2000, a region of convection had developed in east-central Iowa along the simulated cold front. (Though contemporaneous observations indicate that precipitation was not occurring here, late morning surface reports from this region recorded heavy rain, damaging winds, and golf ball-sized hail.) As a result of the strong surface convergence, by late morning the model had produced significant stratus cloud in this region even prior to the spawning of Grid #3. The strong response of the convective parameterization was likely due to the combination of large resolved vertical velocities (> 8 cm s^{-1}) and CAPE values. As the convective system drifted eastward over the more moist soil in eastern Iowa, where sensible surface heat fluxes were weaker and ambient CAPE values smaller, the parameterized convection subsided. By about 23/2030, the parameterized convection for this region was largely finished, though it had produced very heavy rainfall as it exhausted the large CAPE. This cloud mass continued to produce resolved precipitation for the next several hours as it drifted eastward along the cold-frontal boundary.

Soon after this time, the convection directly associated with the subsequent MCC developed in two distinct regions along the cold front. Shortly after 23/2000 an E-W convective line developed along the eastern half of the Iowa-Missouri border, just to the south of the model cold front, continuing WSW about 100 km into SE Nebraska. The initial location of this new convection coincided with the θ_e maximum in Fig. 5.4. In their climatology of the MCCs of 1985. Augustine and Howard (1988) list the time of "first storms" as 2030 UTC, though on this day the definition of "first storms" is indeterminate, as vigorous convection had been occuring in the MCC genesis region almost continuously since dawn.

Stensrud and Maddox (1988) state that the E-W oriented convective line was triggered at its western end by a remnant outflow boundary from the morning convection. Since the simulation had no previous convection in Nebraska this triggering feature was not present. Instead, the resolved low-level vertical motion near the lifted condensation level (LCL) was sufficient to trigger parameterized convection. Fig. 5.5 shows the simulated thermodynamic profile for a model point near Beatrice, Nebraska at 23/2000, just prior to the activation of the convective parameterization. As seen in N-S cross section in Fig. 5.6b positive vertical velocities exceeding 4 cm s^{-1} were found in lowest 2 km of the troposphere along the front, with weak positive vertical motion extending throughout the troposphere, The simulated surface temperature/dew point temperature was 35°C/22°C, which agrees well with the observed values of 36°C/22°C at 23/2100. Note that a stable layer exists in the sounding between about 810 mb and 760 mb. Such a thermal "lid" is commonly associ-

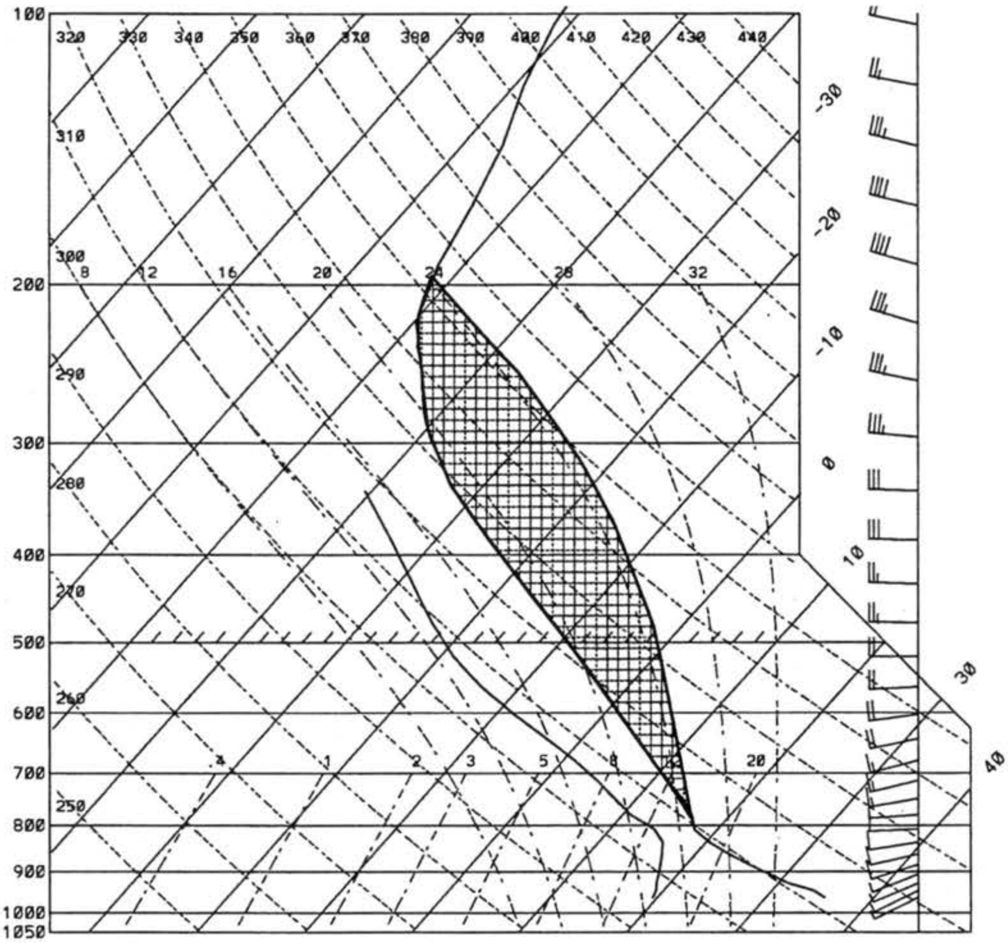

Fig. 5.5. *The skew-t thermodynamic diagram for the simulated sounding for Beatrice, NE at 23/2000, just prior to the onset of convection. The hatched region represents the positive area of buoyant energy with a CAPE value greater that 3700 J kg^{-1}.*

ated with severe convection, as it acts to suppress vertical motion and associated convection, allowing the CAPE to reach very large values (Anthes et al. 1982; Anthes and Carlson 1983). The hatched region indicates the positive area on the diagram, corresponding to a CAPE of over 3700 J kg^{-1}. Several tornadoes, damaging winds, and hail over 5.0 cm in diameter were reported in this area during the period 23/2100 to 24/0200.

Between 23/2030 and 23/2200, both lines continued to intensify. Fig. 5.7a (23/2230) shows contours of vertical velocity variance, $\overline{w'w'}$, a variable predicted by the convective parameterization. Large values of $\overline{w'w'}$ are found in regions where the convective parameterization has recently produced convection. Fig. 5.7b shows the level 3 and level 5 VIPS

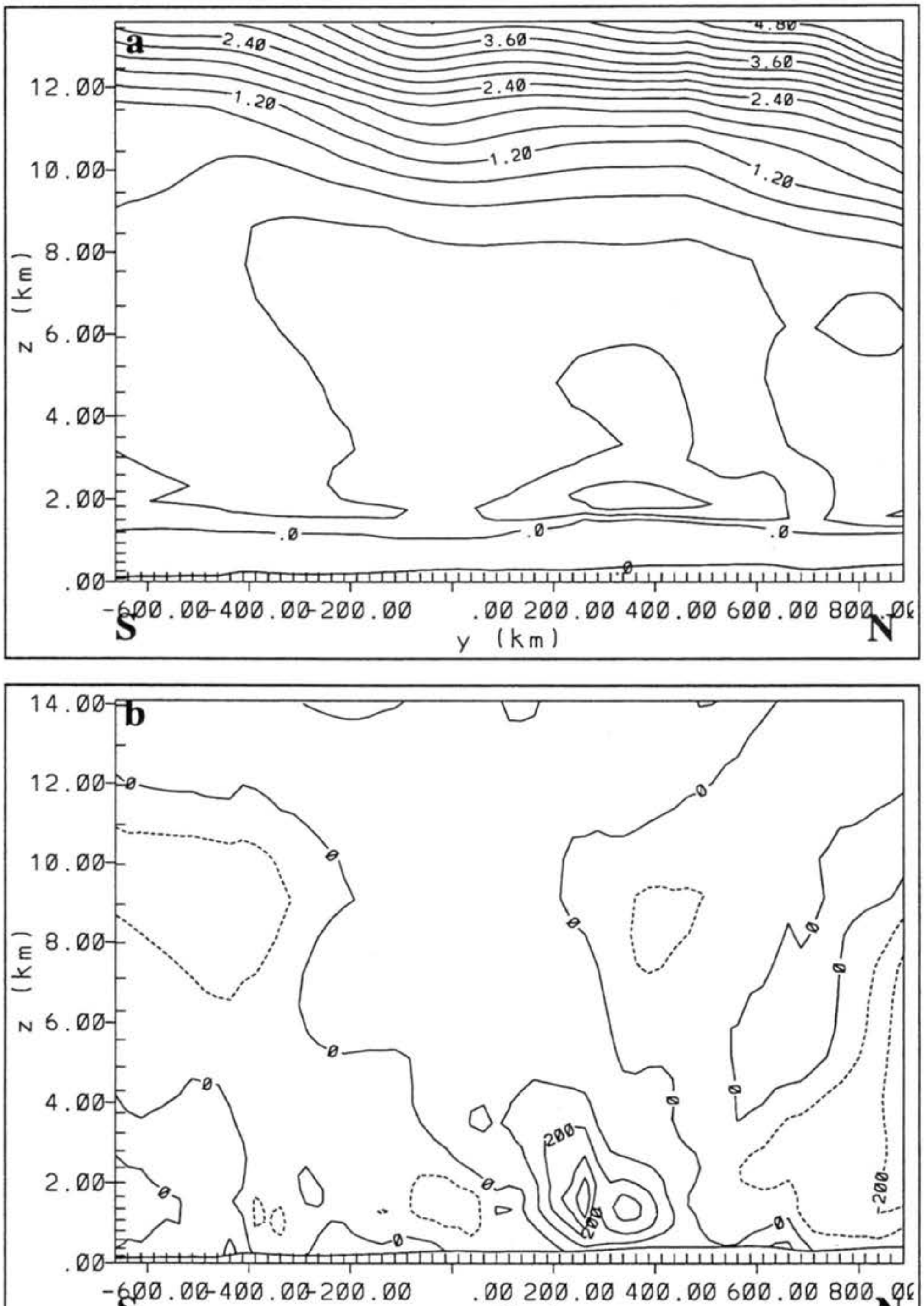

Fig. 5.6. *North-south vertical cross sections of (a) PV and, (b) vertical velocity at time 23/2000. The location of the cross section is along the line AA′ in Fig. 5.3. The PV contour level in a is 0.3 PVU and only positive values are contoured. The vertical velocity contour level in b is 1 cm s^{-1}, with negative contours dashed and the contour labels are × 10^2. (Note that the top of the model domain extends beyond the top of the figures.)*

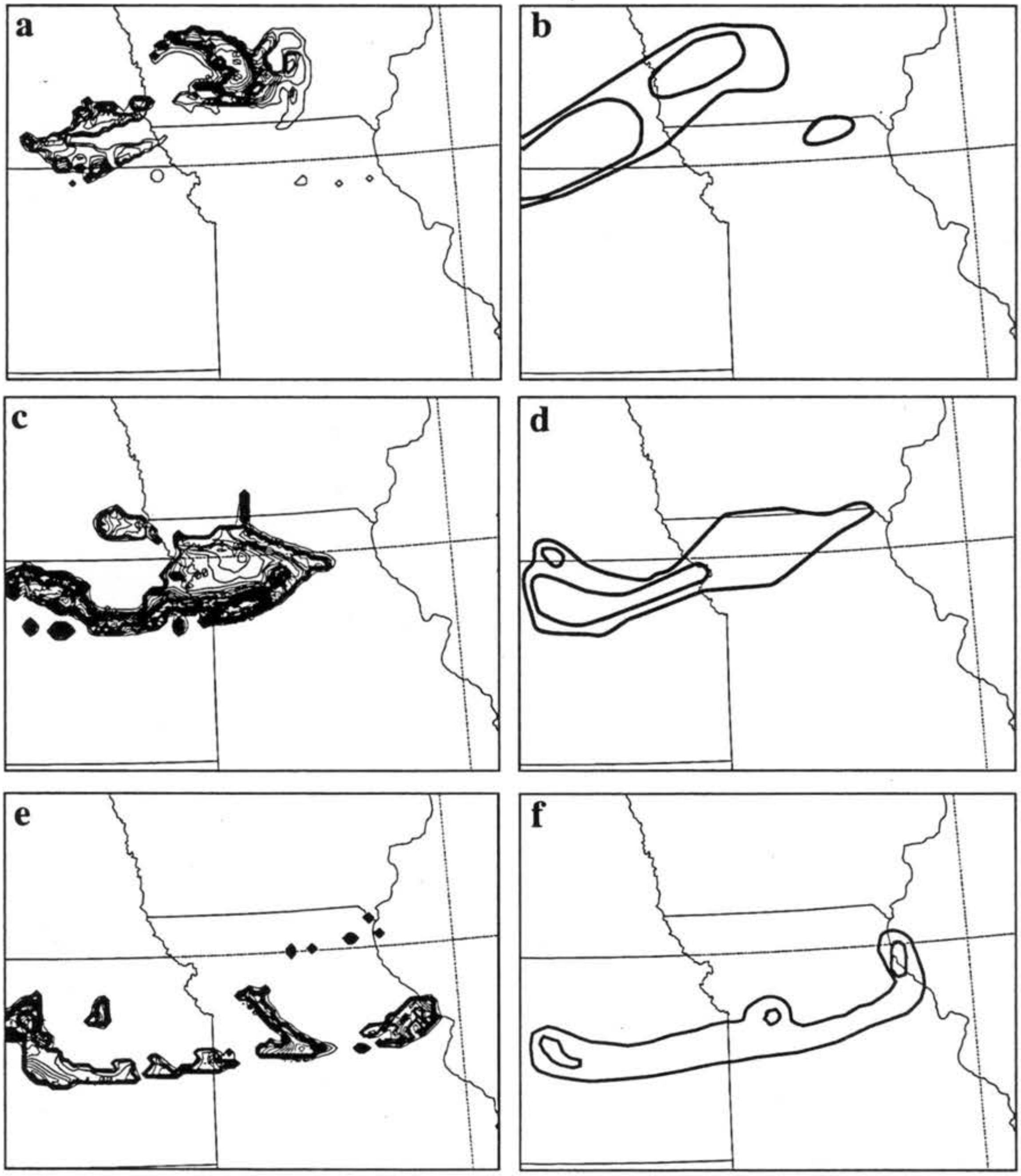

Fig. 5.7. *(a) Surface $\overline{w'w'}$ at 23/ 2230 with contours are 4 m^2 s^{-2}. (The convective parameterization uses $\overline{w'w'}$ as a trigger function. Hence locations where $\overline{w'w'}$ is large indicate, in a short term time averaged sense, where the parameterized convection is occurring in the model simulation.) (b) WSR 57 observed radar echoes, also at 23/2230. Contours are VIPS levels 3 and 5, corresponding to 40.5 and 50.5 dbz respectively (National Weather Service, 1982). (c) Same as in a except $\overline{w'w'}$ contours at 2 m^2 s^{-2}, time 24/0230. (d) Same as b except time 24/0230. (e,f) As in c,d except time 24/0530.*

contours at 23/2230, corresponding to 40.5 and 50.5 dbz, respectively (National Weather Service, 1982). These areas of high reflectivity typically are co-located with regions of strong convective activity. Comparison of Fig. 5.7a and Fig. 5.7b show that the overall pattern of parameterized convection agrees well with the observed convective activity at this time.

Inspection of a well-resolved time series of $\overline{w'w'}$ surface fields reveals that the southward propagation of the western end of the line was the result of new convective bands forming along the low-level convergence zone where the outflow from the current convection met the LLJ in NE Kansas and SE Nebraska. Fig. 5.7a shows a new band of convection of convection developing in extreme SE Nebraska, while the original E-W oriented line behind has lost continuity in SW Iowa. Though parameterized convection continued behind the new line for about another hour, it was much less vigorous, since the positive advection of θ_e by the LLJ was intercepted by the newly developed line to the south.

5.5.2 Early mesovortex development

The N-S convective line in south-central Iowa broadened considerably and by 23/2230 was of almost the same dimensions latitudinally and longitudinally (Fig. 5.7a). The convection occurring in this region at this time was the most intense of the simulation, with rainfall rates exceeding over 5 cm hr^{-1}, again in good agreement with observations. Storm reports from this region record very heavy rainfall, with over 12 cm of rainfall occurring in portions of Madison, Clark and Warren Counties of Iowa in the late afternoon, causing widespread flooding of local streams. Three tornadoes were reported, F0 to F1 on the Fujita (1971) intensity scale, as were numerous funnel clouds and large hail.[2] The simulation developed an MCV in this region, with a closed (storm relative) circulation extend-

---

2. It is acknowledged that the development of this system in agreement with observations is perhaps somewhat fortuitous, as the complex pattern of convective outflows and storm-scale circulations associated with observed convection throughout the day are not captured in this simulation. Typically however, the function of these boundaries is more to provide a focus for the initial convection than to play an essential role in the evolution of the storm dynamics. The mesoscale low-level convergence and θ_e maximum provided the focusing in the simulation.

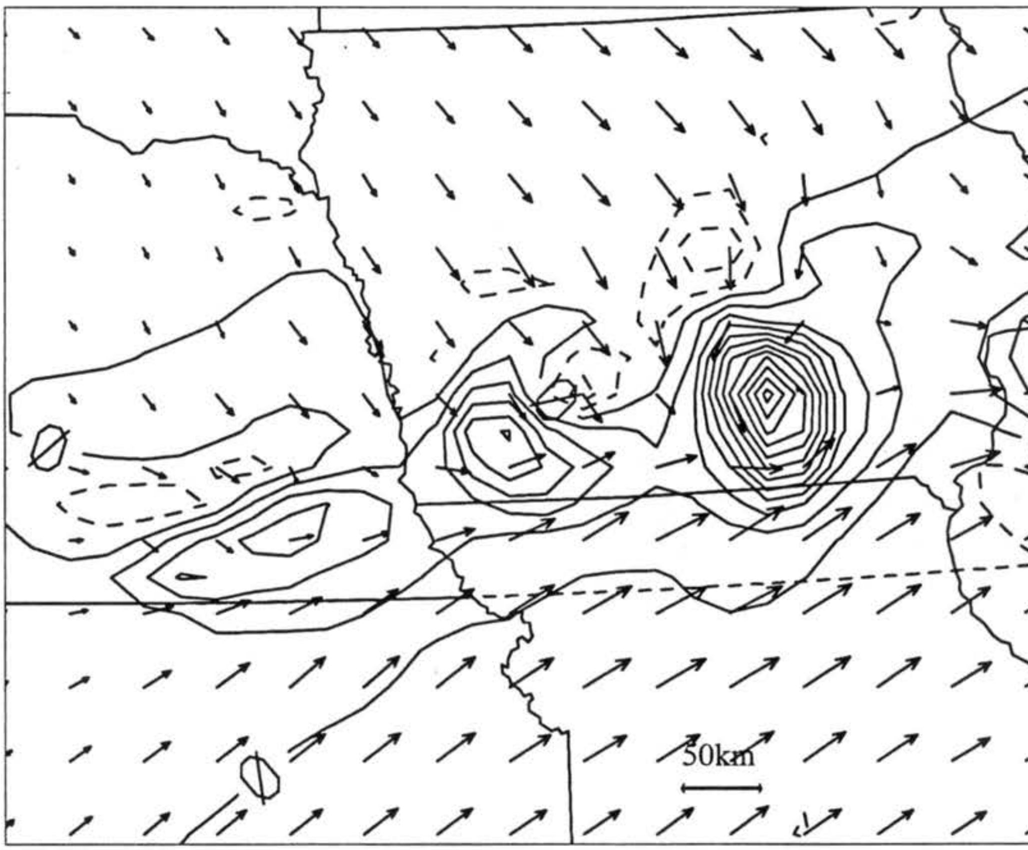

Fig. 5.8. *Simulated relative vorticity (Grid #2) at about 1500 m AGL, 23/2230, with contour level of 0.5×10^{-4} s^{-1}, dashed lines negative. This level was approximately the cloud base of the convective cells. The vorticity maximum of 6.5×10^{-4} s^{-1} (over 6 times the local planetary vorticity) in southern Iowa is associated the N-S oriented convective line which had developed in south-central Iowa 2 hours earlier. Surface observations near this time included heavy rains and several tornadoes.*

ing from near the surface to about 4500 meters. Fig. 5.8 shows the model 23/2230 relative vorticity field at about 1500 m, approximately the level of the convective cell cloud base in this region. The relative vorticity maximum is 6.5×10^{-4} s^{-1}, about 6 times the local planetary vorticity.

In Fig. 5.9a the vertical velocity is plotted at model level 3, about 275 m AGL. The general location of the forward and rearward flanking downdrafts (labeled FFD and RFD respectively in Fig. 5.9a) relative to the circulation center shows good agreement with the observations of Lemon and Doswell (1979), though the wind field shows considerably more convergence than they depict. The updraft in the center of the mesovortex UD1, is much weaker (21 cm s^{-1}) than the convective cell to extreme left of the figure, which has a maximum of 44 cm s^{-1}. The cyclonic circulation, being warm core (> 5° C), has a more stable

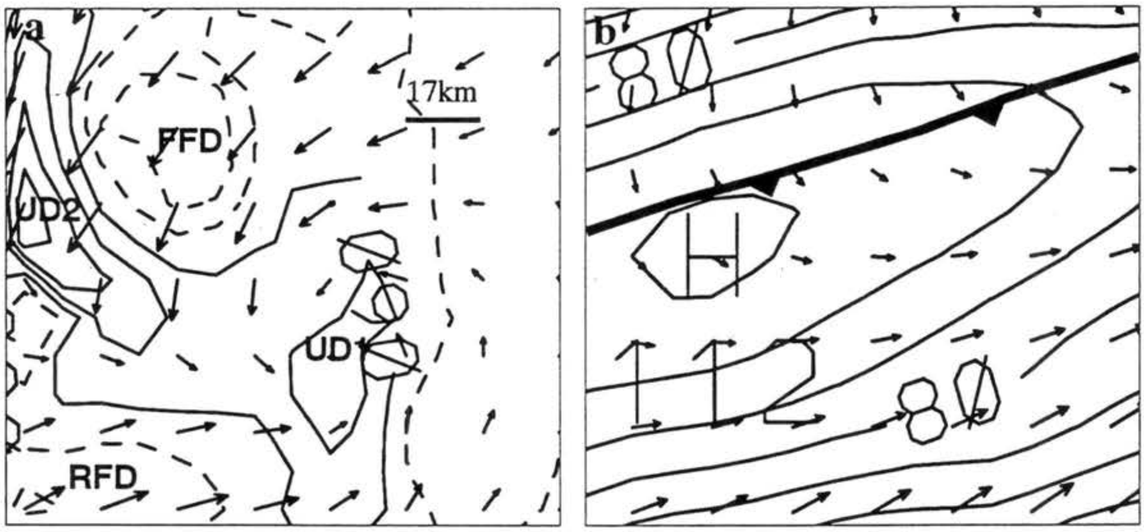

Fig. 5.9. *(a) Grid #3 vertical velocity and winds at 23/2230 at 270 m AGL. The maximum wind vector corresponds to a magnitude of 22 m s^{-1} and the contour level for vertical velocity is 9 cm s^{-1}, with dashed lines negative.The vortex in this figure lies directly under the vorticity maximum depicted in Fig. 5.8. UD1 is the decaying updraft associated with the mesocyclone. UD2 is a newly developed updraft. FFD is forward flank updraft while RFD marks the rear flank downdraft (as in Lemon and Doswell, 1979). (b) Relative vorticity at 23/1900, also at 270 m AGL, contours at 0.1×10^{-4} s^{-1}. The vorticity maximum in this figure is located about 75 km NNW of the circulation center in a.This area of large ambient vorticity along the active cold front is the genesis region for the intense convective storm which produced the MCV 3 hours later.*

vertical thermodynamic profile, which would act to inhibit the updraft velocity. Interestingly, both updrafts in Fig. 5.9a are located beneath the vortex in Fig. 5.8, which is 1200 meters higher. (Note the difference in scale between the figures). At 1500 meters, the vertical motion is almost entirely positive within the closed circulation, while the downdrafts (the dashed lines in Fig. 5.9a) are equally present closer to the surface. The cell associated with UD2 also exists in a more favorable low level θ_e environment, with convergence forced by the collision of the outflow-accelerated NNE winds on the north side and the ambient LLJ on the southwest side.

Fig. 5.9b shows contours of relative vorticity in the genesis region at 23/1900, just before the onset of convection and 3.5 hours prior to the storm depicted in Fig. 5.7a and Fig. 5.8. The relative vorticity maximum of 1.12×10^{-4} s^{-1} (slightly larger than the local planetary vorticity) was just to the south of the active cold front in central Iowa. The winds at the surface were also strongly convergent an the lower-tropospheric vertical velocity increased with height along the front, implying that the stretching/convergence term in the vorticity equation was already enhancing low-level vertical vorticity in the pre-squall line environment.

5.5.3 Early evolution of PV

A Grid #2 cross section of PV in the troposphere and lower stratosphere is shown at 23/2000 in Fig. 5.6a, just previous to any parameterized convection in the simulation. This cross section is located along the line *AA′* in Fig. 5.4, and passes through the surface front in eastern Iowa. The well-mixed, and in some locations superadiabatic, convective boundary layer is apparent in approximately the lowest 1.5 km of atmosphere, the top of this layer being the PV = 0.0 contour (contour interval is 0.3 PVU). The tropopause, near 12 km in the south and sloping downward to the about 8 km in the north, is located at the height where the PV gradient increases dramatically. No tropopause fold is associated with the surface front, though the tropopause does slope more steeply to the north of the front. The core of the upper-tropospheric jet, mentioned in the Section 5.4.1, is located just to the outside (north) of the plot at between 6 and 8 km in height. A region of relatively enhanced lower-tropospheric PV (> 0.6 PVU) associated with the horizontal frontal flow field is seen between 300 and 500 km in the horizontal. This is also a region of mesoscale low-level positive vertical motion (Fig. 5.6b). The "pre-MCC" mesoscale environment, that region from -200 km to about 400 km in the horizontal, is characterized, in the region south of the frontal zone, by a weak PV field (PV < 0.3 PVU) up to a height of 8 km. This is consistent with the climatologically-favorable MCC environment (Maddox 1983; Velasco and Fritsch 1987; Augustine and Howard 1991) under a broad midtropospheric pressure ridge. Here the low PV values are due to *both* the increasing westerly winds towards the north (weak inertial stability) and the pattern of warm advection at the surface (weak static stability) another feature typical in the MCC environment (Maddox 1983; Velasco and Fritsch 1987; Cotton et al. 1989; Augustine and Howard 1991).[3]

The plots in Fig. 5.10 show mid-tropospheric horizontal cross sections of relative vorticity, vertical velocity and PV at 23/2100 at a height of 5220 m. In Fig. 5.10b, the vertical velocity field clearly shows the orientation of the two convective lines. The more bow-shaped configuration of the N-S line looks quite similar to idealized explicit simulations of convective squall lines (e.g., Weisman 1992; Skamarock et al. 1994) though somewhat shorter in longitudinal dimension. The convective updrafts are strongest in the southern half of the line as seen by Skamarock et al. The developing E-W line is also in evidence, as are the areas of compensating mesoscale subsidence, indicated by the dashed (negative) contours.

The relative vorticity associated with the E-W line (Fig. 5.10.a), shows the presence of both large, positive relative vorticity, more or less co-located with the large convective updrafts, and a narrow trailing band of very negative relative vorticity. Note that the *ambient* relative vorticity field at this level is somewhat negative, due to the zonal wind increasing to the north, as seen in the wind vectors in Fig. 5.10a. (The $\zeta = 0$ contours surrounding the convective updrafts are closed.) The contour interval in Fig. 5.10b is $10^{-4}\ s^{-1}$, about the value of the local coriolis parameter. Therefore, regions within closed dashed contours, $\zeta < -1.0\times10^{-4}\ s^{-1}$ represent areas which are *inertially unstable*, in agreement with the PV < 0 contours in Fig. 5.10c. The N-S oriented line also has two associated vorticity maxima, with the developing MCV at lower levels (between 1 and 3.5 km) located under the southern vorticity lobe.

A N-S cross section of PV appears in Fig. 5.11a at time 23/2100, its relative location indicated by the heavy dashed line in Fig. 5.10c. This cross section is aligned parallel to, and behind the leading edge of, the N-S line in SE Iowa. The developing MCV is apparent as the positive PV anomaly with PV > 1 PVU between 2 and 5.5 km in height and 300 to 375 km in the horizontal. A negative upper-tropospheric/lower-stratospheric anomaly and a large region of inertial instability, with large negative (dashed contour) PV has developed south of the convective line. Inspection of Fig. 5.12, which plots wind vectors and con-

3. It is interesting to note that the dichotomous nature of PV reflects both these instabilities, one in the horizontal wind field (PV < 0 implying inertial instability,) and one in the vertical thermal structure (PV < 0 implying static instability). If *both* instabilities are present at the same time however, a scenario approached here, PV loses its diagnostic property as an indicator of stability, since then PV would be positive!

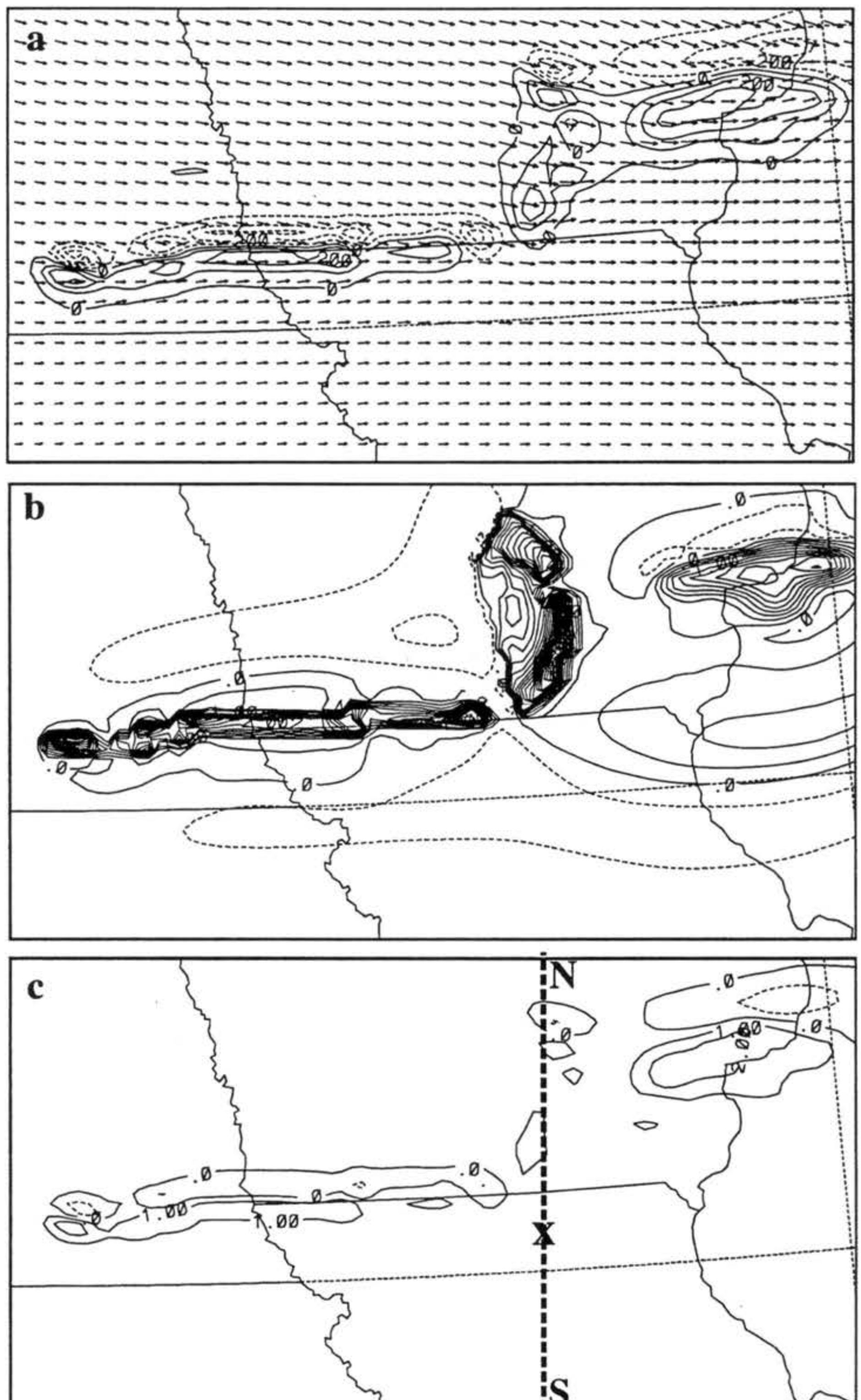

Fig. 5.10. *All plots at time 23/2100 and height of 5220 m ASL. (a) Horizontal winds (max. vector 26 m s^{-1}) and relative vorticity, with a contour level of 10^{-4} s^{-1} with the maximum wind vector having a magnitude of 22.5 m s^{-1}.(b) Vertical velocity, with a contour level of 25 cm s^{-1}.(c) PV, with a contour level 1 PVU. All plots have the negative coutours dashed.*

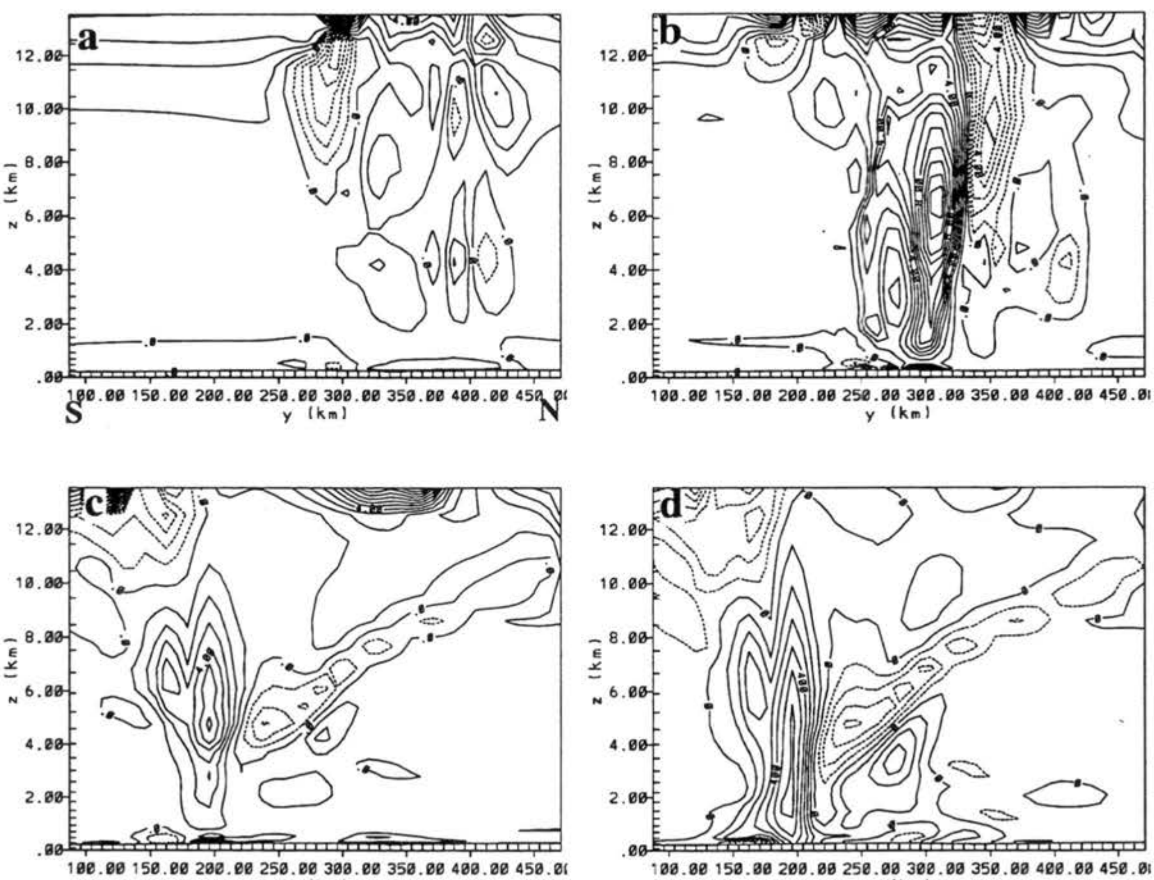

Fig. 5.11. *Panels a, b, and c show cross sections of PV at times 23/2100, 24/0000, and 24/0230 respectively. The cross sections are located along the dashed line in Fig. 5.10, with contours at 1 PVU increments. (d) Relative vorticity (contours at 10^{-4} s^{-1}) at 24/0230.*

tours of PV at 10.5 km (approximately the tropopause), shows that this region of large negative PV seems to be associated the anticyclonic turning of the ambient winds as they are blocked and deflected by the developing high pressure center near the tropopause. Note the undisturbed, ambient PV at this level is generally greater that 1 PVU.

A significant southerly and anticyclonic component to the wind has developed south of the E-W oriented line. Unlike the system farther to the east, the outflow from this line does not seem to present a significant block to the ambient flow, as evidenced by the lack of a stagnation zone upstream of the line, compared to the well-developed stagnation zone upstream of the more eastern N-S oriented line. Apparently, the accelerated southerly upper-tropospheric flow south of the line is primarily due to the outflow detraining from

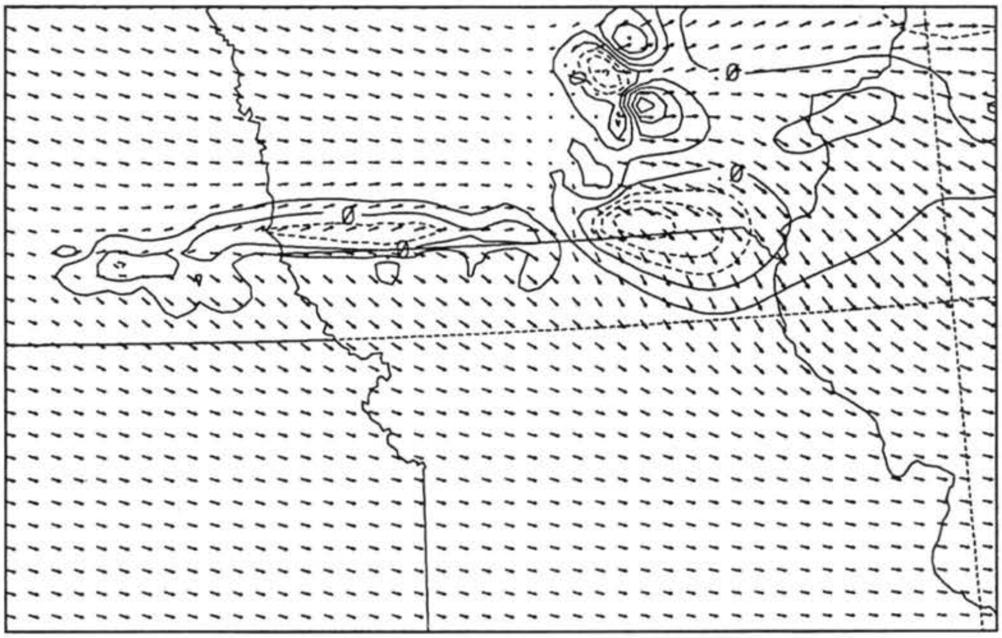

Fig. 5.12. *Winds and PV at 1 PVU increments at a height of about 10.5 km and time 23/2100. The maximum wind vector length in the figure represents a speed of 45 m s^{-1}.*

the convective updrafts. This effect is certainly also contributing to the southerly flow south of the MCV bearing system, but it is difficult to separate from blocking.

Recall that the discussion in Chapter 2 predicted a convective PV dipole structure with a negative anomaly above the positive anomaly. In the N-S cross section of Fig. 5.11a, the upper, negative anomaly is much larger that the lower, positive anomaly, with the minimum displaced southward of the lower anomaly. By contrast, the mid-level positive PV (Fig. 5.10c) associated with the E-W convective line *does* have a relative PV minimum located directly above it (Fig. 5.12). These differences are mostly due to the fact that the N-S line is more mature and storm-generated southerly shear has had time to advect the lower PV values, a factor not built into the simple conceptual model. (The simple conceptual model also does not consider strong vertical shear of the horizontal wind, a significant factor here.)

5.6 The Mature Stage and Dissipation

For the next several hours, the E-W oriented squall line continued to propagate south, with the western end in Kansas/Nebraska moving more rapidly. After a brief diminution in convective activity between 24/0000 and 24/0100 the convection again strengthened. Fig. 5.7c shows the simulated $\overline{w'w'}$ surface field at 24/0230, while Fig. 5.7d shows the WSR 57 level 3 and level 5 VIPS contours for the same period. The leading edge in Iowa is by now well decoupled from the front, though the strong convectively-driven circulations have made this frontal region poorly defined. The simulated convection over southern Nebraska and NE Kansas has also started to move away from the front. This time marks, perhaps, the greatest areal extent of parameterized convection, though the greatest convective precipitation rates occurred in the late afternoon, when CAPE values were highest and the convection had a more favorable low-level positive vertical velocity environment. This diurnal dependence of precipitation rates agrees with Maddox's (1980) climatology of MCC events. Houze et al. (1990), in their study of heavily precipitating MCSs in springtime Oklahoma, also noticed that severe weather (e.g., hail, tornadoes) seemed to occur in the early formation stages of MCSs, before large areal coverage of precipitation was seen.

Comparison of Fig. 5.7c and Fig. 5.7d shows generally good agreement between the simulation and observations. While the parameterized convection does not extend as far east as the level 3 VIPS contour, the location of the MCV is on the right (eastern) end of the parameterized convective line, and the resolved Grid #3 vertical motion of greater than 1 m s^{-1} (associated with significant resolved rainfall) extends beyond the end of the parameterized convective line in Fig. 5.7c.

During the period from 23/2300 to 24/0230, the overall organization of the storm became altered from the two distinct lines (visible in the vertical velocity fields of Fig. 5.10b) to the more continuous structure with a more clearly-defined squall line leading edge, as seen in Fig. 5.7c. Fig. 5.13 and Fig. 5.13 show plots of relative vorticity, horizontal winds, vertical velocity and PV at 5220 m AGL at 24/0000 and 24/0230 respectively. The horizontal cross section of vertical velocity at 24/0000 (Fig. 5.13b) shows this transition, with 3 vertical velocity maxima; a crescent-shaped maximum in SE Iowa associated with the MCV

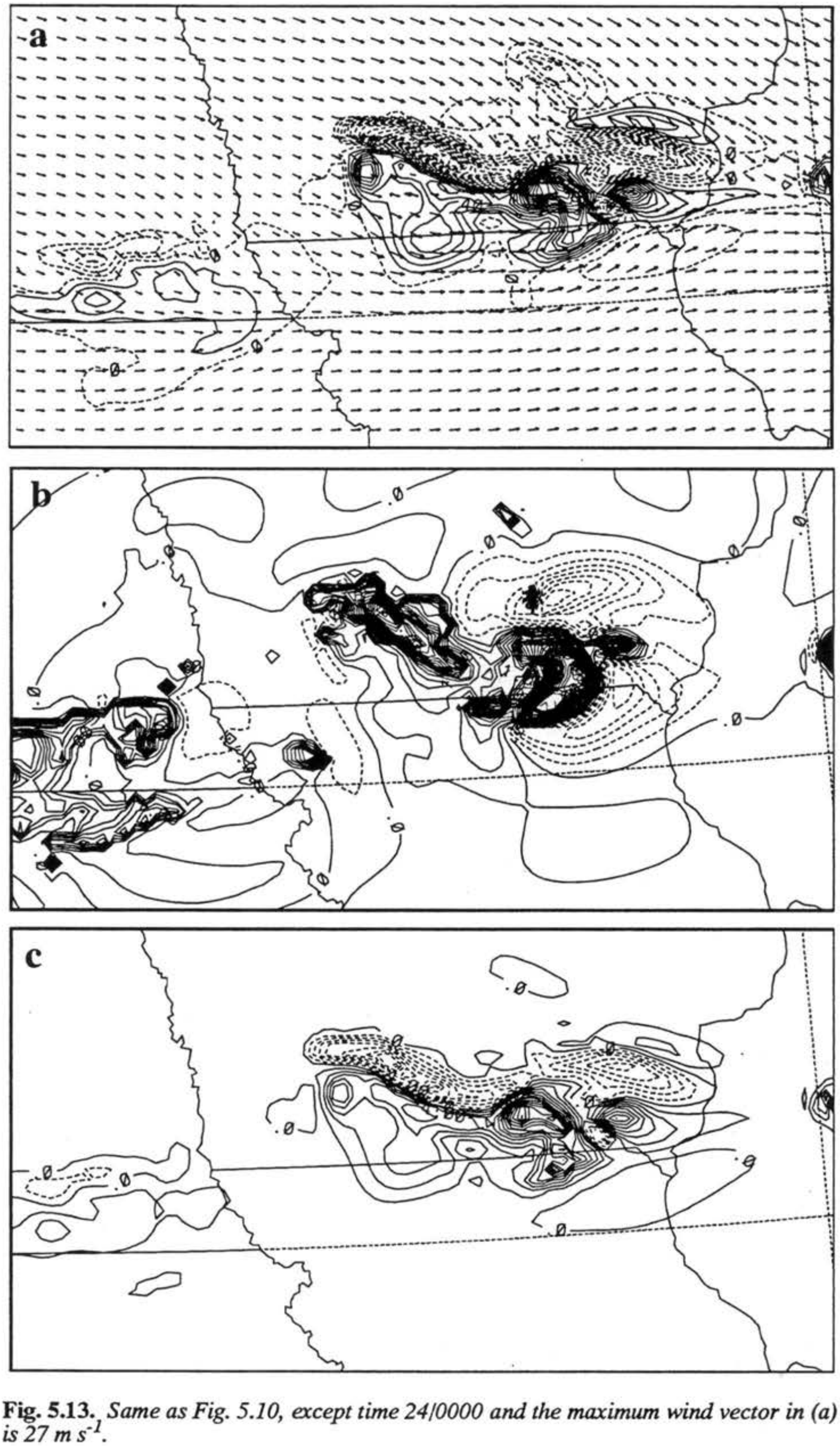

Fig. 5.13. *Same as Fig. 5.10, except time 24/0000 and the maximum wind vector in (a) is 27 m s^{-1}.*

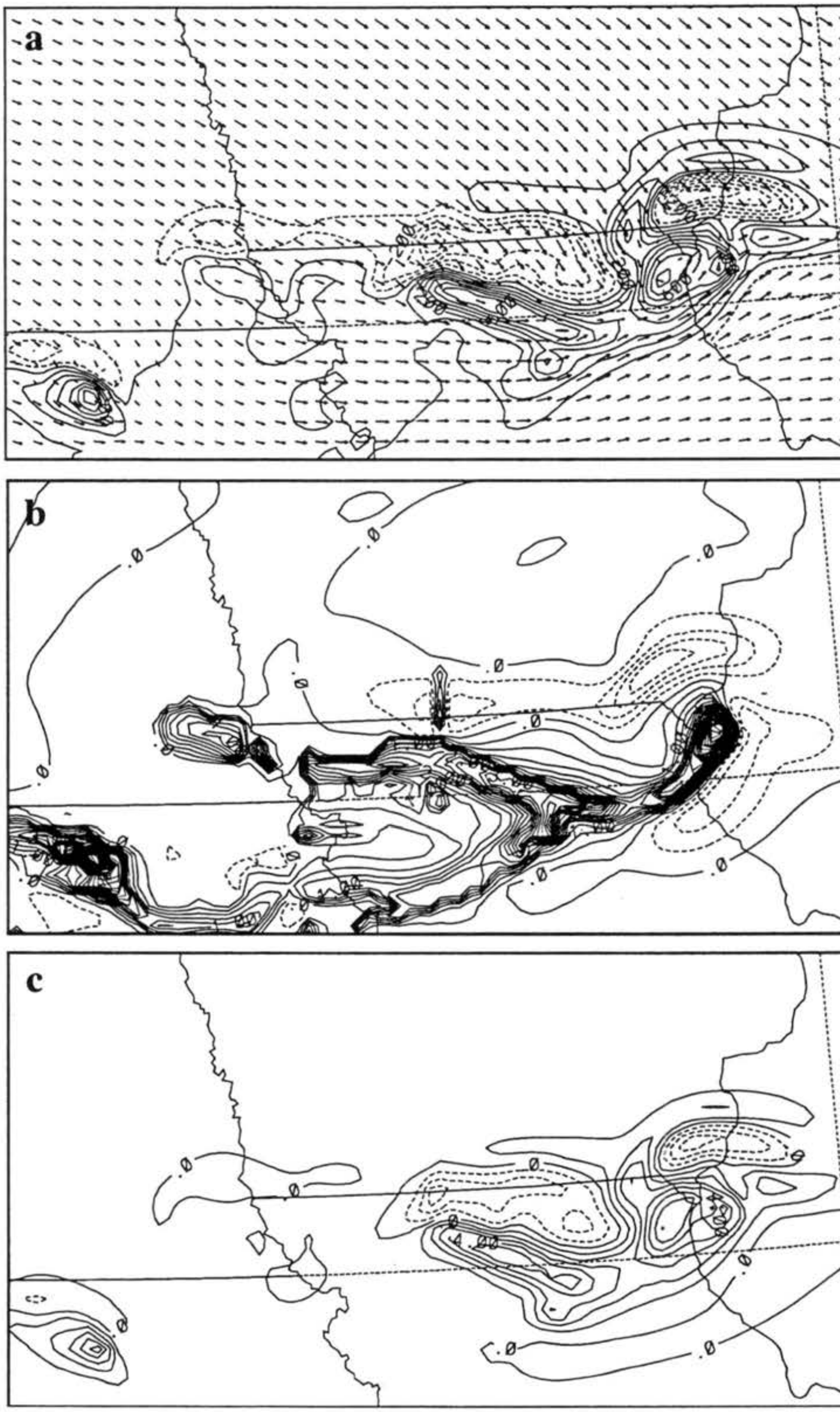

Fig. 5.14. *Same as Fig. 5.10 except time 24/0230 and the maximum wind vector in (a) is 28.5 m s^{-1}.*

(see the relative vorticity on Fig. 5.13a), a second in south-central Iowa and a third, smaller, elongated w maximum associated with the convection along the far eastern common border of Nebraska and Kansas.

The crescent-shaped vertical velocity maximum in SE Iowa in many ways resembles the "bow-echo" shape seen in radar observations (Fujita 1978; Schmitt and Cotton 1989; Burgess and Smull 1990) and in simulations (Weisman et al. 1988; Schmidt 1992; Weisman 1992, 1993; Davis et al. 1994; Skamarock et al. 1994). Though this storm is evolving in a very complex environment, unlike the horizontally-homogeneous, unidirectional-shear simulations of Weisman (1993), many of the flow structures seen in those simulations, such as a mesovortex on the north end of the bow at between 2 and 3 km AGL, are seen here. The tendency for stronger updrafts on the south half of the bow-shaped developing convective line seen as early as 23/2100 (Fig. 5.10b) agree well with the findings of Skamarock et al. (1994). This bow-shaped multi-cellular updraft structure contracts in the along-line dimension in the next 3 hours, from about 120 km in length at 23/2100 to about 70 km by 24/0000. During this time, the bow curvature increases sharply, maintaining its cross-line dimension while contracting orthogonally.

By 24/0230, 2.5 hours later, the mid-tropospheric vertical velocity (Fig. 5.13b) shows a more linear maximum along the leading edge of the convection and a much larger region of weaker mesoscale ascent. The (horizontal) location of the lower tropospheric MCV, at the eastern end of the line, still has a slight mid-tropospheric comma signature in both the vorticity, Fig. 5.13a, and vertical velocity, Fig. 5.13b, though it has propagated south and east, pivoting such that the long axis has become oriented more NE-SW as it has become incorporated into the leading updraft line.

The mid-tropospheric vertical velocity at 24/0130 (not shown) shows a detailed composition with considerable banding. Such a structure with an irregular leading edge, along line as well as front-to-rear variability, and an along-line asymmetry biased towards the NE, is similar to the "Weakly Classifiable, Asymmetric" classification of Houze et al (1990), who found this structure frequently associated with severe weather. Part of this finer structure is an E-W oriented bow-shaped line, much larger than the similar N-S oriented updraft structure seen in Fig. 5.10b. This bow-shaped line extended from the MCV region centered in extreme SE Iowa, SW along the leading convective edge across the eastern third of Missouri and then turning north, finally terminating near the midpoint of the Iowa/ Missouri border. Interestingly, the western half of the line was *not* along the leading convective edge, but developed, between 24/0100 and 24/0130, as a relatively stronger line *behind* the leading edge. This southward-propagating persistent bow feature remains apparent in the simulation for several hours, and is still detectable in the midtropospheric vorticity field at the end of the simulation (24/1200).

5.6.1 Evolution of the Rear-Inflow Jet and MCV

Examination of the wind vector plots in Fig. 5.10, Fig. 5.13 and Fig. 5.13 show an increasingly larger southerly component to the midtropospheric horizontal winds with time, this development coinciding with the evolution of E-W bow-shaped convective line mentioned above. Fig. 5.10a, at 23/2100, early in the development on the squall line, shows very little meridional component to the mid-tropospheric flow. By 24/0000 (Fig. 5.13) there is a distinct meridional storm-induced perturbation, and by 24/0230 the midtropospheric flow is northwesterly over the entire state of Iowa. The existence and evolution of this so-called "rear-inflow jet", a feature common to many squall lines and MCCs, is well documented in several observational studies (e.g., Smull and Houze 1985,1987a,b; Leary and Rappaport 1987; Johnson and Hamilton 1988; Schmitt and Cotton 1989; Houze et al. 1990) and also appears to be a robust feature in both numerical simulations (Zhang and Fritsch 1987,1988; Zhang et al. 1989) and idealized MCS and squall line simulations (Weisman 1992, 1993; Schmidt 1992; Davis and Weisman 1994, Skamarock et al. 1994).

The N-S cross section 24/0130 in Fig. 5.15a (same geographic location as section shown in Fig. 5.11) displays contours of vertical velocity and Fig. 5.15b has contours of the meridional (v) component of velocity. Both figures have the descending rear-inflow jet (RIJ) highlighted in light gray and the approximate cloud boundary marked by the heavy dashed line. At this time (about half way between the times valid for Fig. 5.13a and Fig.

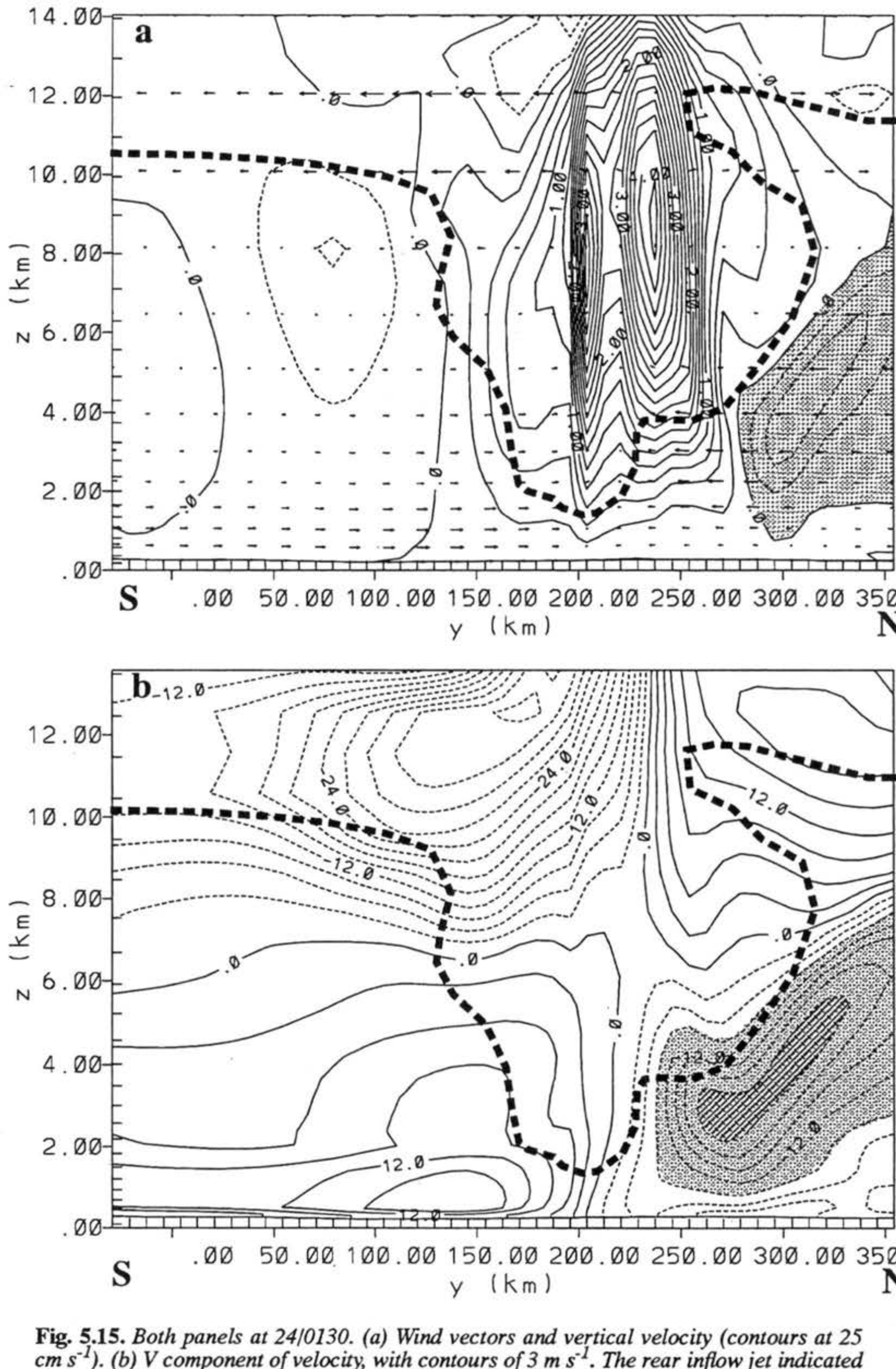

Fig. 5.15. *Both panels at 24/0130. (a) Wind vectors and vertical velocity (contours at 25 cm s^{-1}). (b) V component of velocity, with contours of 3 m s^{-1}. The rear inflow jet indicated by the gray shading. The diagonal striping in b denotes southward flow > 21 m s^{-1}. The heavy dashed line in both diagrams indicates the approximate outline of the cloud The location of these cross-sections in the same as in Fig. 5.11.. The position is indicated as the dashed line in Fig. 5.10. Negative contours in both panels are dashed.*

5.13a) the RIJ is already well developed. In the jet core, marked by the diagonal hatching in Fig. 5.15b as the region where the meridional wind speed is greater that 21 m s^{-1}, the subsiding motion exceeds 0.5 m s^{-1}. The RIJ corresponds well to the sloping rearward edge of the stratiform cloud region. Another southerly speed maximum appears south of the storm above about 8 km and is accompanied by a region of subsidence between 5 and 10 km ASL (Fig. 5.15a), as the cloud detrains in the upper atmosphere.

An hour later at 24/0230, the downdraft has penetrated to the surface (Fig. 5.16a). Though the (shaded) jet core has about the same meridional configuration as the previous hour, there are now two distinct subsidence maxima, the lower occuring just behind the convective line, and another, more rearward and elevated, along the sloping stratiform cloud region. This dipolar structure of mesoscale descent below the stratiform cloud region and ascent within the cloud has been observed in several MCS case studies (e.g., Smull and Houze 1985, 1987a,b; Johnson and Hamilton 1988). The downdraft maximum just along the rear flank of the convective line probably results from the combination of convective and mesoscale downward motion[4]. At this time also, the $v = 0$ contour is extending to the front of the convective line.

Concurrent with the time the RIJ downdraft reached the surface behind the convective line, the convective activity began to slowly weaken. Smull and Houze (1987b) also observed one of the storms in their study weakened as the RIJ reached the surface and began to undercut the convective line. They theorized that some of the lower θ_e air comprising the jet was entrained from the back side (rather than the leading edge) into the convective cores. This would act to decrease the CAPE and weaken the convection. The simulated θ_e values in the lower portion of the RIJ showed a significant depression from surrounding values. Here, the minimum θ_e of 320 °K behind the MCC, found initially at about 4.5 km ASL, eventually reached to within 500 m of the surface, near the back of the convective line, lending support to Smull and Houze's hypothesis.

4. It should be noted that velocity cross-sections presented here are *not* storm-relative, as is the case in the work of Smull and Houze. At this time, the squall line had a southward velocity of about 7.5 m s^{-1}. The gray shading in the N-S cross section corresponds to a contour of $v = -9$ m s^{-1}, which *would* be rear inflow in the relative sense.

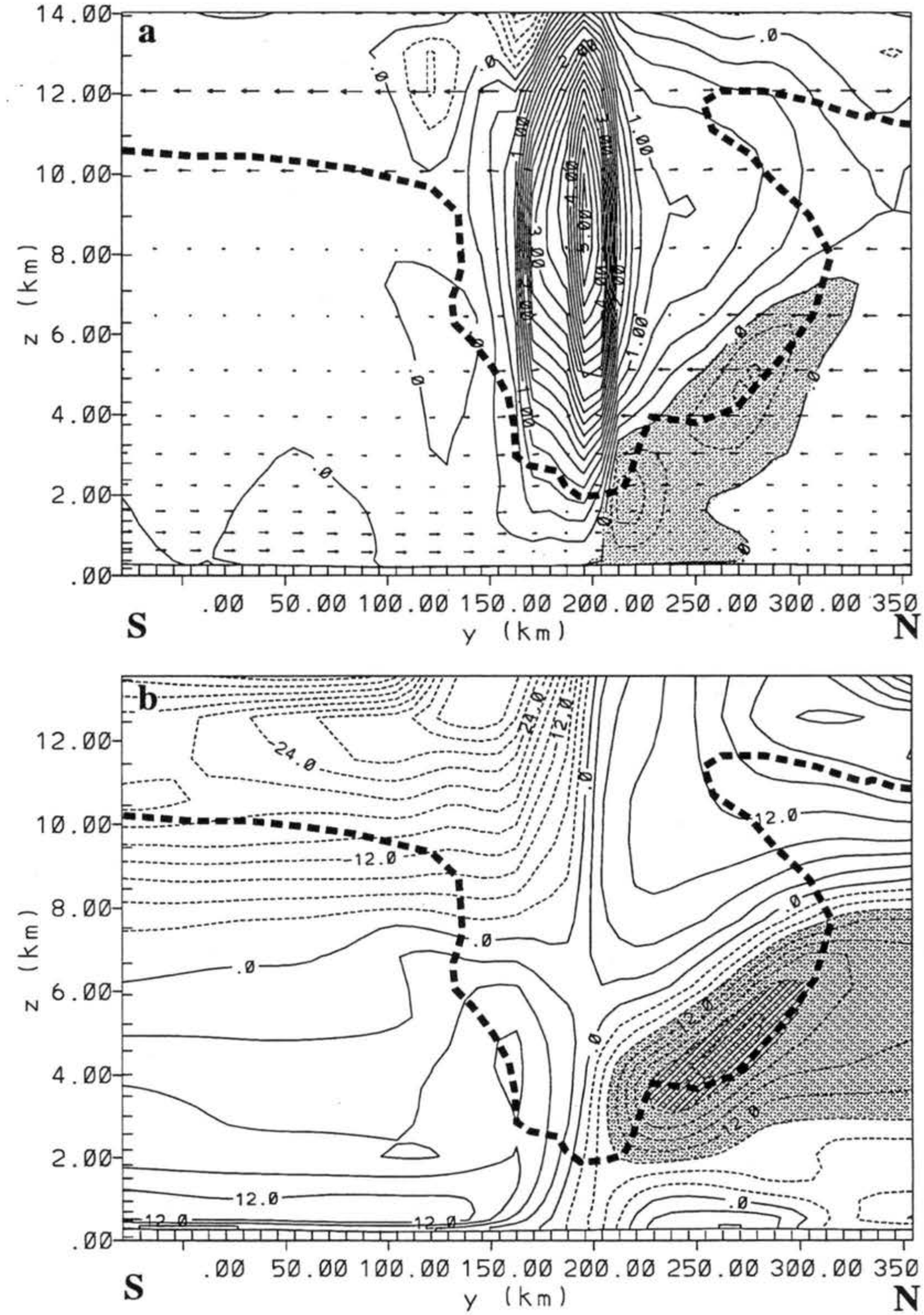

Fig. 5.16. *Same as Fig. 5.15 except at time 24/0230.*

By 24/0400, (Fig. 5.17) at about the time of maximum RIJ strength, the mesoscale downdraft region extended upward from the surface to over 10 km ASL, near the tropopause. Within the RIJ core, downdrafts exceeded 1.25 m s^{-1} and southerly winds extended beyond the front of the convective line. This type of undercutting of the convective updrafts was seen by Smull and House (1987b, see their Fig. 11d).

Front-to-rear flows have developed near the surface and above the RIJ in the stratiform region, as seen in Fig. 5.17b. There is a region of strong divergence near the surface as outflow from the RIJ pushes northward under the stratiform region. The vertical shear in the transition zone between these flow branches exceeds 10^{-2} s^{-1}, which agrees well with Smull and Houze (1987b) who note that a similar three-tiered flow arrangement was seen by Smull and Houze (1985) and Srivastrava et al. (1986).

5.6.2 The western end of the squall line in Kansas

During the period discussed in Section 5.6.1, the portion of the squall line extending into Kansas continued to grow. Radar observations (Fig. 5.7b,d) show that the strongest convection was oriented parallel to, and just south of, the stationary front, giving the convective line a NE-SW orientation. While the simulated convection had this orientation tendency early on (Fig. 5.7a), several hours later the convection had pushed south along the Kansas/Missouri border, with a convex, rather than the observed slightly concave, configuration (compare Fig. 5.7c and d at 24/0230).

The vertical velocity field over far eastern Nebraska and Kansas (Fig. 5.13b) shows well-developed updraft cores, with (Grid #3) vertical velocities exceeding 2 m s^{-1}. Note that this plot of midtropospheric vertical velocities indicates two separate regions of convective growth, similar to the NWS radar charts. Contemporary (24/0000) IR satellite observations however, do not show evidence of this storm structure. Evidently, the cold cloud shield generated by the two mesoscale updraft lines had merged.

As discussed previously, a line of weaker convection had developed ahead of the stronger, bow-shaped convective line in north-central and NW Missouri. The vertical-velocity cross

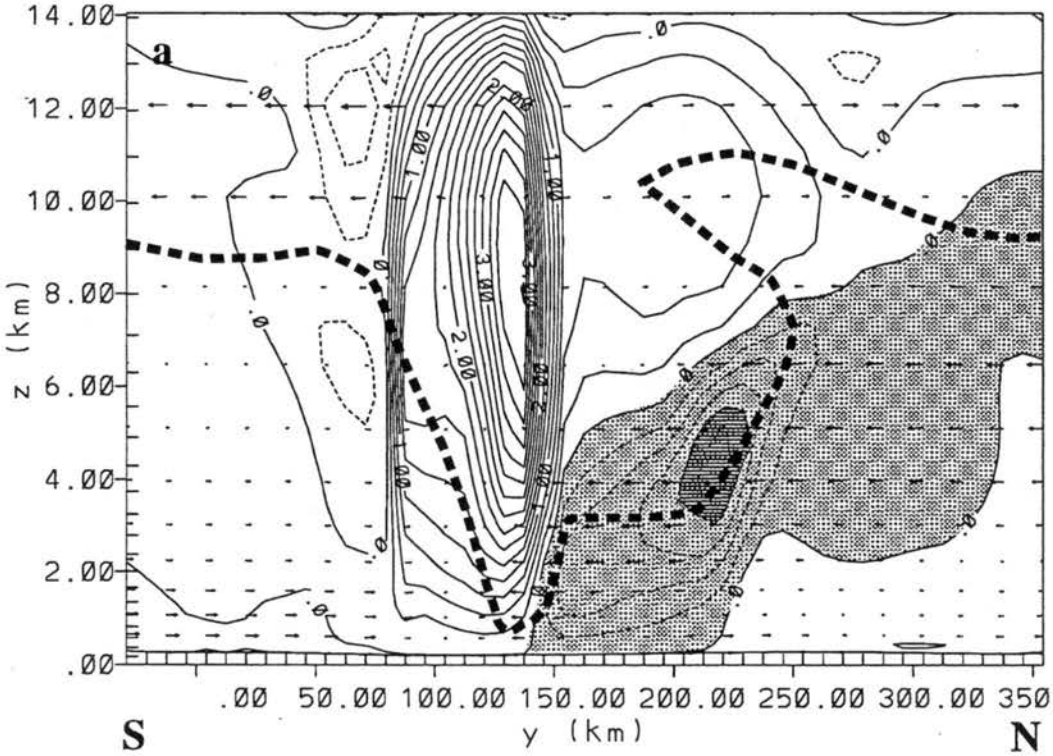

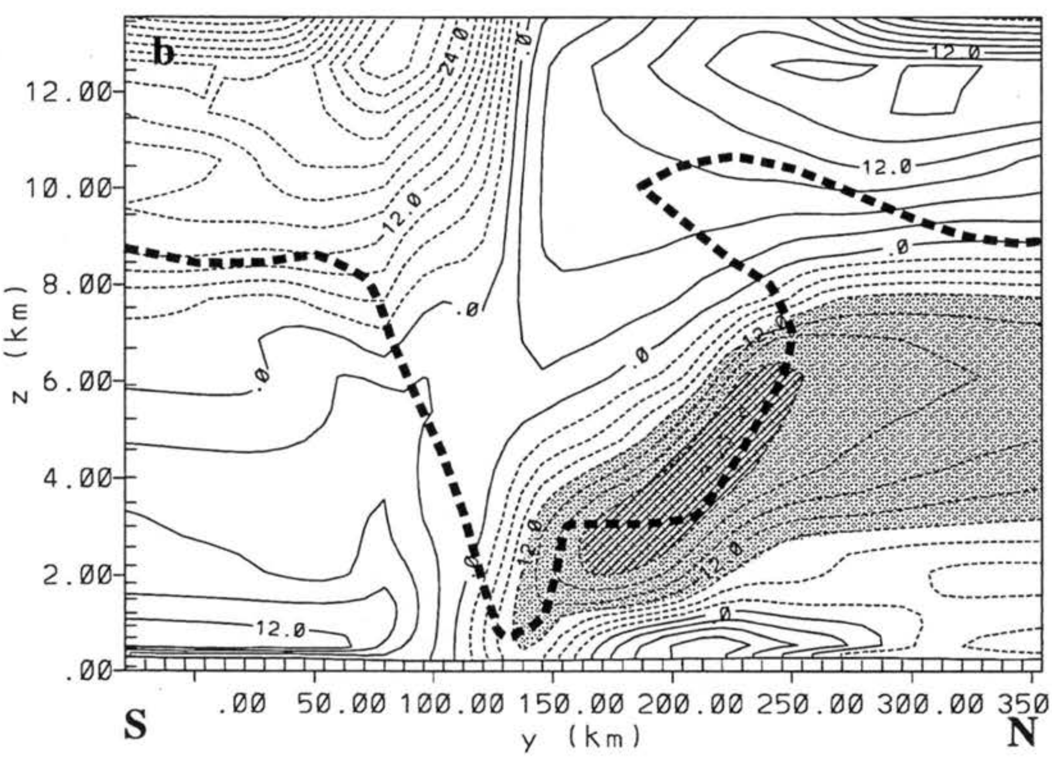

Fig. 5.17. *Same as Fig. 5.15, except at time 24/0400. The horizontal hatching in a denotes downdrafts in excess of 1 m s^{-1}.*

section in Fig. 5.13b (also at 24/0000) indicates that this weaker convection is responsible for the convex appearance of the leading line. During the next several hours, the model solution and observations converged. By 24/0530, (Fig. 5.7e,f) the orientation of the line in Kansas was again similar to the pattern of radar echoes.

During the upscale growth of this western extension of the storm, between 24/0130 to 24/0530, another vortical circulation began to form over extreme NE Kansas. This MCV is evident (Fig. 5.13, 24/0230) in both the midtropospheric vertical velocity and in the relative vorticity maximum which exceeds $5 \times 10^{-4}\ s^{-1}$. There was also a precipitation maximum associated with this feature, with rain rates exceeding 30 mm h^{-1}. NWS radar charts (0130-0430) also show a small, yet persistent, region of very strong reflectivity in this region.

5.6.3 Along-line banded vorticity structure

One of the intriguing features seen in this period of the simulation is the banded vorticity pattern oriented parallel to the squall line. This feature has been previously observed, both in Doppler radar studies (Biggerstaff and Houze 1991a,b) and MCS simulations (Zhang et al. 1989). Biggerstaff and Houze, who saw relative vorticity $\zeta < -3 \times 10^{-4}\ s^{-1}$ in a band along the transition zone (Smull and Houze 1987a) just behind the updraft cores, concluded that tilting of horizontal vorticity was largely responsible for the banding in their case.

A very similar feature is seen here in the 23-24 June simulation. Even in the earliest stages of squall line development (Fig. 5.10a, 23/2100) a very narrow band of negative relative vorticity $\zeta < -2 \times 10^{-4}\ s^{-1}$ is found behind the updraft cores along the Iowa/Missouri border. Three hours later, (Fig. 5.13a) the developing bow-shaped line in SE Iowa has developed a wider band of negative relative vorticity, with $\zeta < -6 \times 10^{-4}\ s^{-1}$ being found. By 24/0230 (Fig. 5.13a) this feature is still evident, though now the anticyclonic vorticity band has smaller magnitude. In addition another, positive, band has developed to the rear of the storm. Fig. 5.13a looks quite similar to Fig. 3a (550 mb) of Biggerstaff and Houze (1991b).

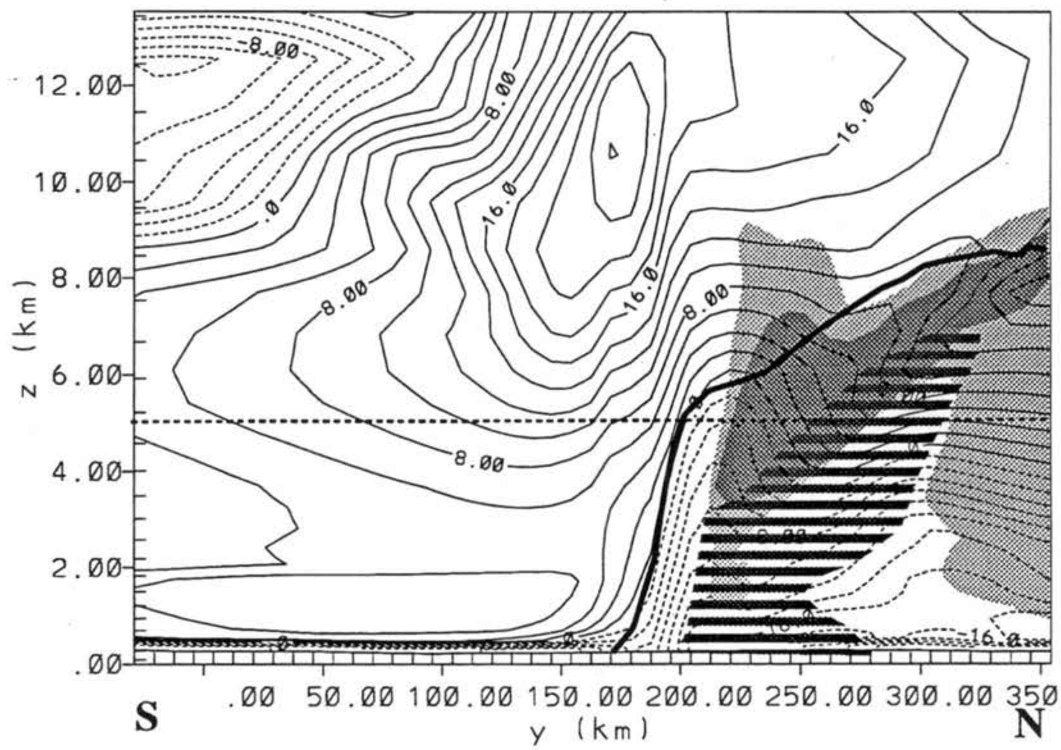

Fig. 5.18. *Contours of the E-W (u) component of the storm-relative wind at 24/0230 with a contour level of 2 m s^{-1}. The light gray shading denotes the area where relative vorticity is negative, while the darker gray indicates negative PV. The horizontal bars show the region of subsiding motion. The heavy dark line locates the zero contour of meridional velocity (not storm relative). The horizontal dashed line locates the level of the horizontal cross section in Fig. 5.13.*

As expected, this banding is also in evident in the PV fields, (see panel c in Fig. 5.10, Fig. 5.13, and Fig. 5.13), with the $\zeta = -1 \times 10^{-4}$ contour agreeing with the transition from positive to negative PV values. Panels c and d in Fig. 5.11 show N/S cross-sections of ζ and PV respectively at 24/0230. These cross sections strongly suggest that the RIJ is fundamental to this banded structure (compare with Fig. 5.16, same location and time).

To further examine the role of the RIJ in this banding, consider Fig. 5.18. The contours in this N-S vertical cross section are of storm-relative zonal (u) velocity. The light gray shading denotes $\zeta < 0$ and the dark gray shading PV< 0 (typically where $\zeta < -f$). The horizontal bars denote the RIJ downdraft and the heavy line shows where the meridional velocity changes sign, positive (northerly) to the left and negative (southerly) to the right of the

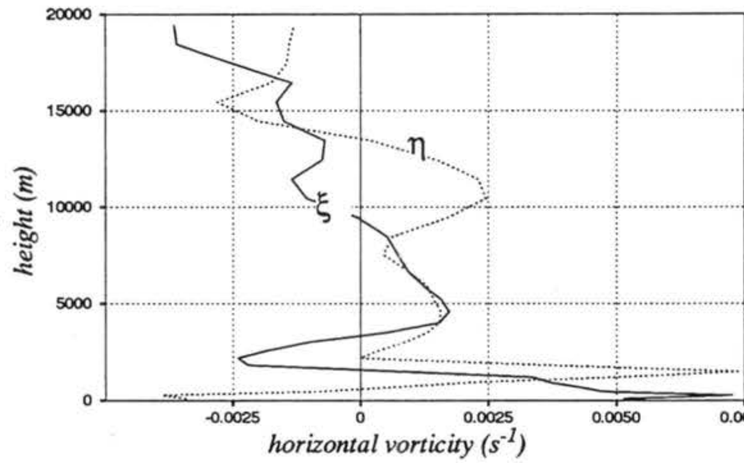

Fig. 5.19. *A vertical profile of the horizontal components of vorticity (ξ zonal and η meridional) at 23/2100 for the location marked by the X in Fig. 5.10. This may be considered as representative of the background horizontal vorticity in which the RIJ developed.*

line. For reference, the straight dashed line locates the level of the horizontal cross sections in Fig. 5.13.

The contours of zonal velocity are strongly deformed in the region of the RIJ, which is apparently advecting the zonal momentum downward and southward. The relative vorticity is very large in the convective updrafts. Note that the locations where $\partial u/\partial y$ changes sign correlate well with the boundary between positive and negative relative vorticity (light gray in the figure), indicating that the vorticity is largely determined by horizontal shear of u. Further, $\partial u/\partial y$ is largest just along the southern extent of the downdraft region (left side of horizontal bars) region of the downdrafts. Moving north, the vorticity again becomes positive near the core of the downdrafts.

From the foregoing discussion it is now evident how the banded structure seen in Fig. 5.13 depends on perturbed zonal velocity structure, apparently a consequence of advection by the RIJ. It is also instructive to consider this banded structure from the standpoint of vorticity dynamics. Fig. 5.19 shows a vertical profile of the horizontal components of vorticity typical of the large scale environment in which the MCS and RIJ developed. Note that at the height of 5220 m (the dashed line in Fig. 5.18),. both the zonal (ξ) and meridional (η) components of vorticity are positive and of similar magnitude, near 2×10^{-3} s^{-1}, or

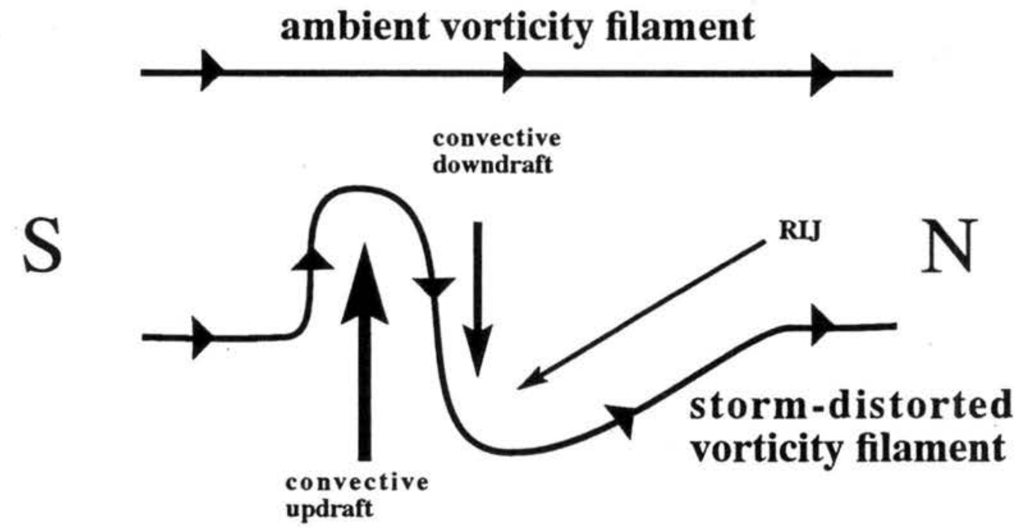

Fig. 5.20. *A schematic illustration of how a vorticity filament, initially almost horizontal, becomes distorted (tilted) by the MCS generated vertical motion field. (similar to Biggerstaff and Houze 1991b, fig. 8.*

about 20 times larger than f. Therefore the total vorticity vector is almost horizontal, and pointed to the northeast.

Now, consider the distortion, by tilting, of a representative vorticity filament in the region of the convective updrafts (Fig. 5.20). This figure may be considered, in this case, as a projection of the (horizontal) vorticity filaments onto a vertical N-S plane bisecting the squall line near its midpoint. The perturbed filament in the bottom half of the diagram is tilted steeply upward, then downward by the combined action of convective downdrafts and the RIJ. To the rear of the storm, the filament again tilts upward into its undisturbed position. This simple schematic, similar to that of Biggerstaff and Houze (1991b) agrees well with the model results in Fig. 5.13a and Fig. 5.18.

Biggerstaff and Houze note that this feature has not been observed in other case studies. The above discussion would suggest that this along-line banded vorticity phenomenon requires the coexistence of a significant component of horizontal vorticity normal to the squall line and a well-developed RIJ.

5.6.4 Later evolution of the MCVs

Both of the MCVs discussed earlier were still evident at 24/0530, their vorticity, pressure and temperature perturbations extending almost to the tropopause. The larger, western MCV, which had existed at this time for over 8 hours, has been left well behind the leading convective line. [5]

Fig. 5.21a shows the storm relative winds at this time at 3000 m. The light gray shading in this figure denotes the region where the relative vorticity $\zeta > 10^{-4}\ s^{-1}$ and the darker shading corresponds to $\zeta > 4 \times 10^{-4}\ s^{-1}$. Both MCVs are located near the darker gray, generally circular regions of roughly 50 km in radius. This appears, at first, as a rather unexpected vorticity configuration for a squall line. Several simulations of idealized squall lines in sheared environments (Weisman 1992; Weisman et al. 1992; Davis and Weisman 1994; Skamarock et al. 1994) show a pattern of what Weisman (1992) terms counter-rotating "bookend vortices"; a cyclonic vortex to the right (in their cases north, in this case east) of the low-level shear vector, and an anticyclonic vortex to the left (in their cases south, in this case west). Here, the vortex to the left of the low-level shear vector (i.e., the MCV in E Kansas) is cyclonic. This discrepancy can be resolved when one realizes that the vortices evolved in essentially different squall lines. The MCV in Kansas has developed near the location of the pre-existing surface low, shown in Fig. 5.4., while the MCV along the eastern Iowa border developed at the right (with respect to the low level shear vector) end of a bow shaped squall line of finite length, in the manner consistent with the results of Davis et al. and Skamarock et al. IR satellite photos (see Fig. 7c of Stensrud and Maddox 1988) at 24/0600, as the convection is starting to weaken, show a concave shape to the southern edge of the -63 °C temperature contour, with a northward deflection along the Kansas/Iowa border. This, and the existence of the persistent, somewhat circular reflectivity maxima mentioned earlier (see Fig. 5.7f), both offer observational support to the notion that

5. Tilting has not been demonstrated to be the sole agent acting here. Indeed convergence/stretching of vorticity is undoubtedly acting also. It should be noted however, that convergence/stretching can *not*, by itself, change the *sign* of the absolute vorticity. This requires horizontally-varying vertical motion (i.e., tilting) in an environment where the absolute (vertical) vorticity is initially positive.

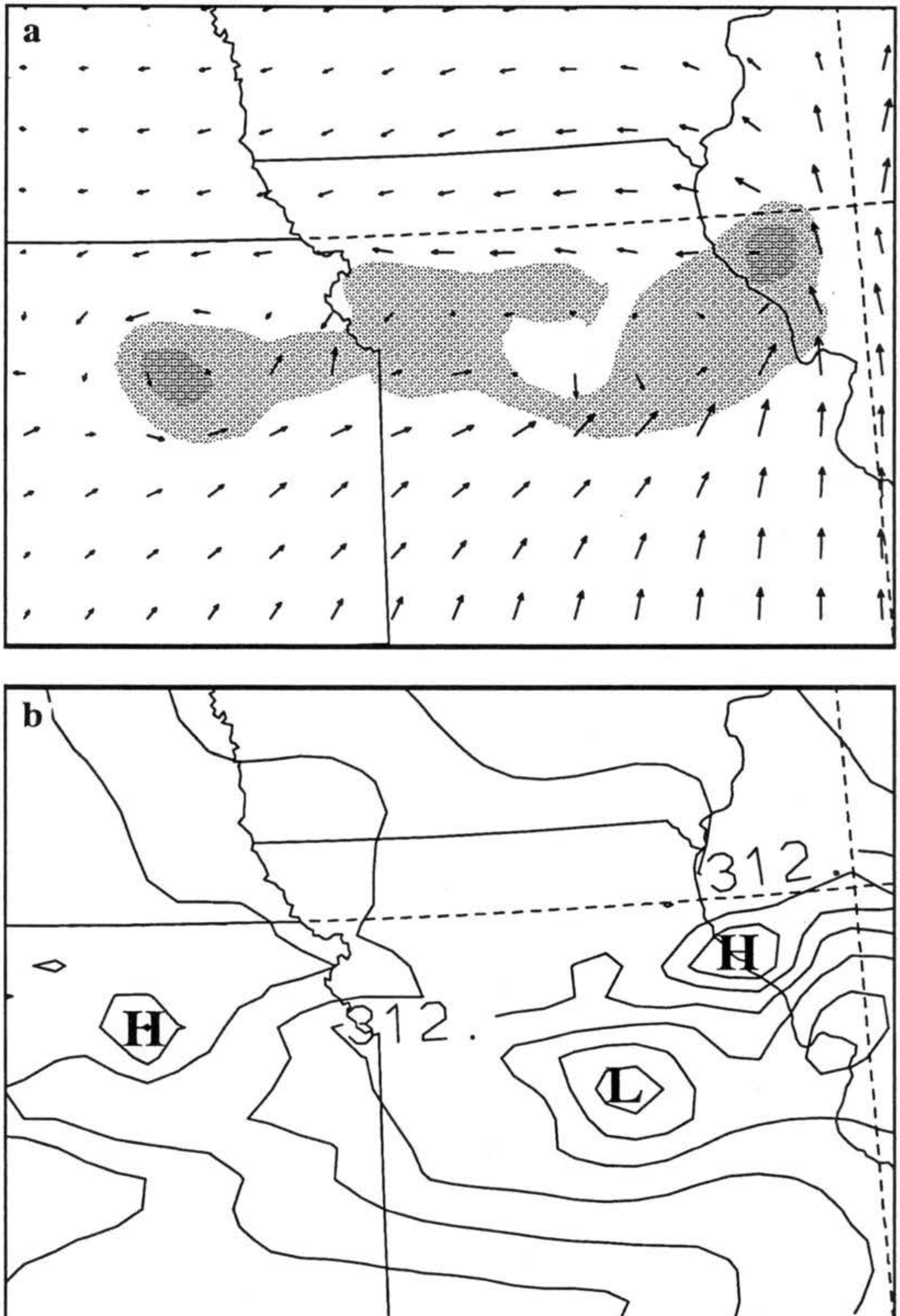

Fig. 5.21. *(a) The storm relative horizontal winds at 3000 m, 24/0530. The largest wind vector corresponds to a speed of 27 m s^{-1}. The light gray shading denotes areas with relative vorticity greater than 10^{-4} s^{-1} while the darker shading denotes areas with relative vorticity greater than 4×10^{-4} s^{-1}. (b) The potential temperature θ, also at 3000 m, 24/0530, contour level 1.0°K*

the western end of the squall line had, to some degree, developed its own semi-independent mesoscale circulation.

The relative vorticity pattern in Fig. 5.21a shows the presence of the RIJ in central Missouri, where the $\zeta = 10^{-4}\ s^{-1}$ contour has been strongly eroded away along its northern edge. The wind field also shows its strongest northerly flow at the head of this eroded vorticity contour. The location and hooked nature of this region (with a minimum relative vorticity $< -1.5 \times 10^{-4}\ s^{-1}$) also may be related in part to the anticyclonic vortex predicted by Skamarock et al. 1994. In that work, the simulation with coriolis force activated showed a growth of the cyclonic bookend vortex into an MCV and a weakening of the anticyclonic vortex with time. Their anticyclonic vortex developed at the left end of the convective line, while this feature appears to be in the middle. Recall however, that the stronger, bowed convective line at 24/0230 was preceded by a line of weaker updrafts (refer to Fig. 5.17b). If the bowed line of strongest updrafts is considered the dynamically significant line of convection in this context, the relative vorticity minimum in Fig. 5.21a, seen 3 hours later, would then agree with the idealized results of Davis and Weisman (1994) and Skamarock et al. (1994).[6]

The (storm-relative) wind vectors show closed circulations of at least 100 km radius around both MCVs. On the scale of the entire squall line, Fig. 5.21a shows a system-wide (storm-relative) elliptic closed cyclonic flow encompassing the entire squall line, and enhanced by the highly curved vortical flow on both ends. It is interesting to observe that in the older, eastern MCV, the center of the circulation and vorticity maximum are not co-located. The strengthening anticyclonic circulation around the building high pressure ridge centered in Mississippi is shearing and deforming this vortex as it propagates east. Fig. 5.21b shows that the western MCV has a relatively warm core, in agreement with sev-

6. It is difficult, if not impossible, to separate the various processes (e.g., end vortex formation, rear-inflow jet) in the generation of this vorticity minimum. Indeed the results of Skamarock et al. and Davis and Weisman suggest that they are intimately related phenomena. Their idealized studies are invaluable in helping to isolate and elucidate the processes occuring in nature and actual case simulations (like the one under discussion here) where large-scale environmental factors, other interacting storms, and secondary processes, such as radiation and surface drag, make interpretation more difficult.

eral MCV observations (e.g., Menard and Fritsch 1989; Fritsch et al. 1994) and modeling studies (Zhang and Fritsch 1987,1988). The older, eastern MCV has a more complex structure, which is difficult to describe as either warm or cold core. The vorticity maximum on the Iowa/Illinois border is co-located with a temperature maximum, but as noted before, the closed circulation extends well beyond this vorticity maximum. A cooler region lies at the front of the dissipating convective line in east-central Missouri, likely a consequence of the evaporatively-cooled RIJ, which may be overrunning and reinforcing the surface cold pool there.

5.6.5 Dissipation of the squall line

After 24/0400, the storm began to decrease in intensity and by 24/0600 the storm was into its dissipation stage. The storm-relative RIJ was no longer descending to the surface (Fig. 5.22) and the core (> 21 m s^{-1}) was now contained within the stratiform cloud region. The leading edge updraft zone of vertical velocities greater than 1 m s^{-1} was by now only about 40 km wide while the maximum downdraft speed associated with the RIJ was only about 80 cm s^{-1}, the downdrafts no longer extending upward to the tropopause. While significant N-S divergence was still occuring at the surface where the RIJ intersected the ground, it had weakened considerably in the past 2 hours. Further evidence indicative of the weakening storm-scale circulation was the dramatic decrease in the divergent southward outflow above 12 km, from a maximum of 33 m s^{-1} at 24/0400 (Fig. 5.17b) to a maximum of only 24 ms^{-1} just 2 hours later.

Fig. 5.7e shows the location of the parameterized convection at 24/0530, which is now starting to weaken considerably. Fig. 5.7f shows the corresponding NWS WSR57 radar echoes. The location and orientation agree well with the simulation. The strong echo on the eastern Missouri border verifies with the location of the eastern MCV (Fig. 5.21a,b). Even though the convective parameterization is not active there (see surface $\overline{w'w'}$ field, Fig. 5.7e), the model is still simulating updrafts greater than 2.5 m s^{-1} in this region, and producing moderate precipitation. The back edge of the outer (VIPS level 3) contour in east-

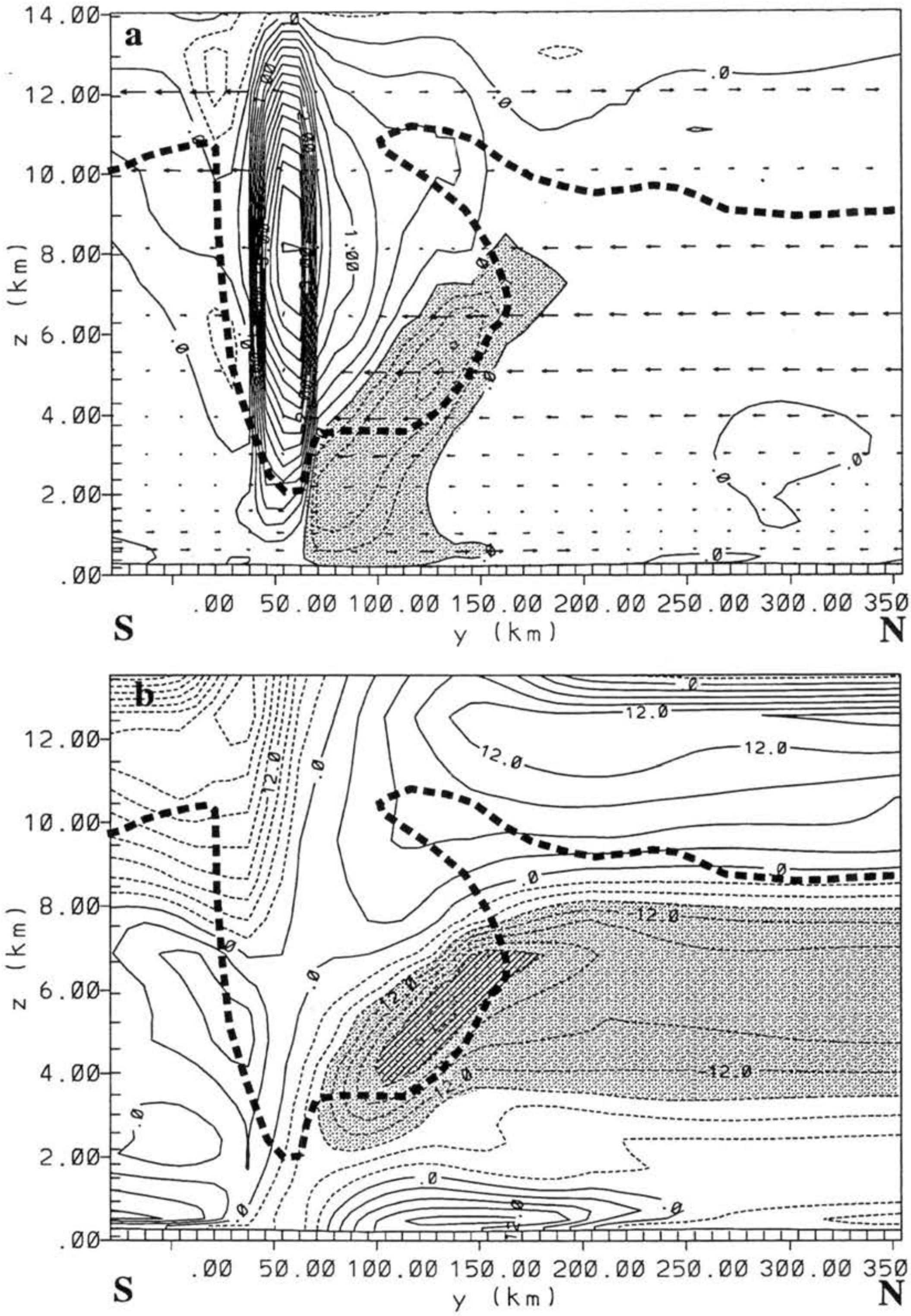

Fig. 5.22. . *Same as Fig. 5.15, except at time 24/0600.*

central Missouri shows a bowing similar in shape to that of the midtropospheric vertical motion of the simulation an 3 hours earlier (Fig. 5.13b).

A new thunderstorm, not evident in the radar summary charts or satellite images an hour earlier, had developed in north central Illinois by 24/0630. This storm is outside the domain of Grid #3, and consequently was not simulated, the convective parameterization being activated on Grid #3 only.

By 24/0730, the parameterized convection had largely ceased. The stratiform portion continued to produce resolved light precipitation for about the next 3 hours. By 24/2400, all precipitation from the storm had ceased. Both MCVs had weakened considerably as they drifted ESE in the mean flow. The upper portion of the eastern MCV continued to elongate due to the shearing action of the developing synoptic scale flow and the decaying RIJ. While there was no precipitation, upward motions greater than 0.5 m s^{-1} existed at midtropospheric levels in the region of the decaying MCVs. Fig. 5.23 shows the model circulation at 5220 m (horizontal mean pressure 527 mb) at the end of the simulation (24/1200). Also shown in this figure are the observed winds (bold wind barbs) at 500 mb from the standard NMC sounding network, 24/1200. The winds agree quite well in speed and direction, with the notable exception of the Springfield, Illinois sounding value. There, the simulation showed weak northerly winds while the observations had strong southwesterlies. The observed wind field likely was locally influenced by the observed convection which had occurred in central Illinois for the past several hours. This convection was not simulated by the model (see discussion above).

Though this storm occurred outside the PRE-STORM network, there were PRE-STORM research aircraft flights through the storm in the period from 24/0900 to 24/1300. The daily operations summary from the field project (Meitín and Cunning 1985) noted that the two aircraft encountered a warm-core vortical circulation at 10000 ft. (3050 m) over east-central Missouri at around 24/1030 This agrees fairly well with Fig. 5.21, (3000 m) valid at 24/1030. Meitín and Cunning further state that the circulation did *not* seem to be found at 15000 ft (4600 m) by the other aircraft at that time. Johnson and Bartels (1992) note that

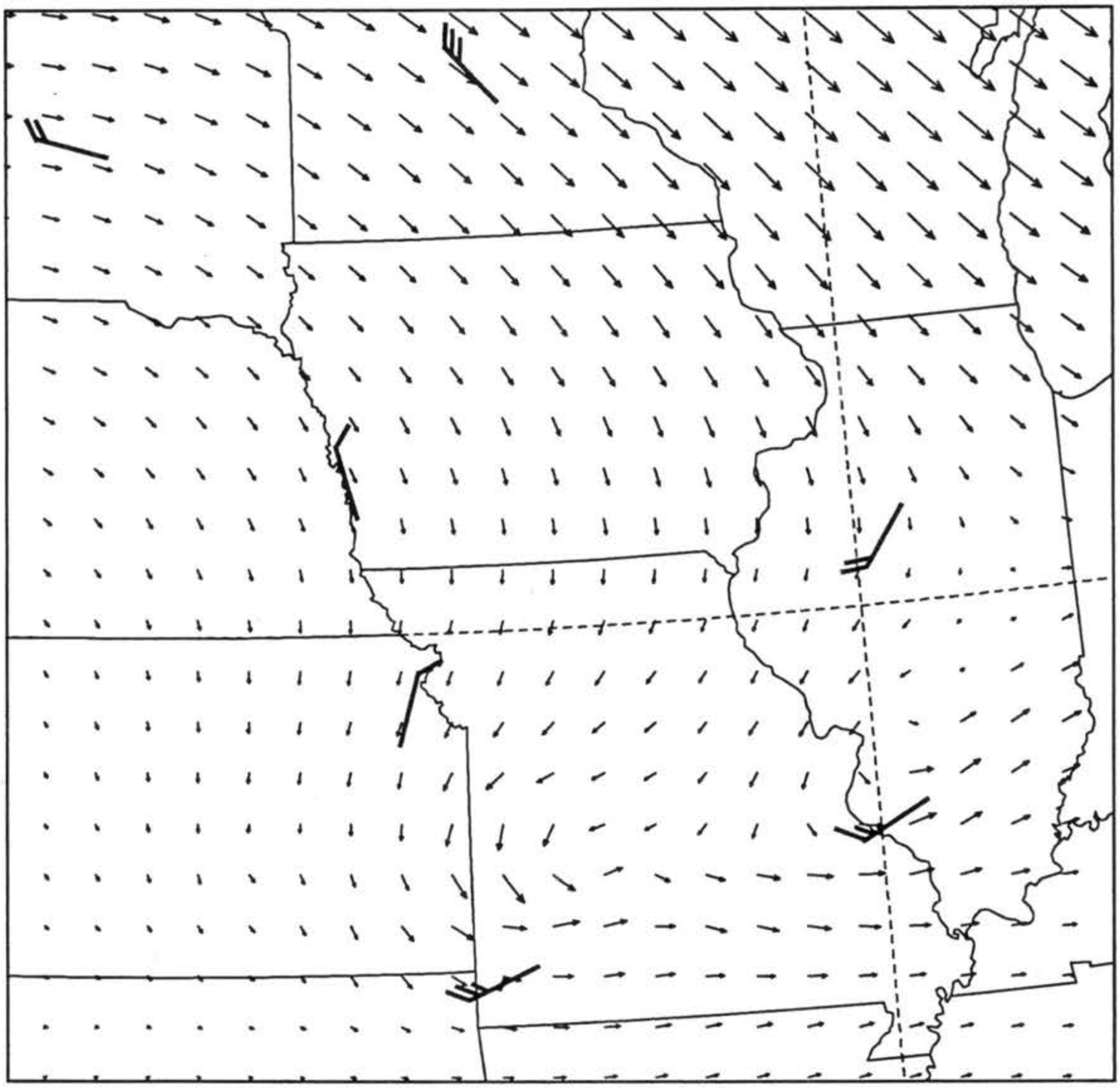

Fig. 5.23. *The model flow field at 5220 m ASL at the end of the simulation, 24/1200. This is the model level closest to the 500 mb level, with a mean pressure of 525 mb. Also plotted in this figure are the 500 mb observed winds (wind barbs) at 24/1200 from the standard NWS soundings. The largest wind vector (N Wisconsin) corresponds to a wind speed of 37 m s*$^{-1}$*. Full wind barb flags represent 5 m s*$^{-1}$*, half flags 2.5 m s*$^{-1}$*.*

the vortex *was* evident in the standard 500 mb NMC analysis for 24/1200. Examination of the wind barbs in Fig. 5.23, obtained from the NMC analysis referred to by Johnson and Bartels, does seem to indicate a closed cyclonic circulation over Missouri. The better resolved simulated winds (wind vectors) show a much more complex circulation, though obviously there exists meteorologically significant positive vorticity over the post-MCC region. Brody (1987) detected a "distinct comma shape, indicating an upper vorticity maximum had formed." This comma feature, seen on the visible satellite image at 24/1230, is about 100 km east of the simulated 24/1200 midtropospheric vertical velocity maximum.

5.7 Summary

The purpose of the simulation was to produce a reasonable data set to analyze in the context of balanced dynamics. The 23-24 June simulation in general agreed well with the surface and upper-air observations, satellite images, and ground-based radar. Several features typical to MCCs were simulated: a strong leading convective line, a trailing region of stratiform rainfall, formation of an MCV, and development of a rear-inflow jet.

In the next chapter we will examine the evolution of the balanced and unbalanced flows during the lifetime of the storm and consider how the evolving storm modifies its larger-scale environment.

Chapter 6: Balanced Analysis of the PE Simulation

6.1 Introduction

In the last chapter the results from a PE model simulation of the 23-24 June, 1985 MCC were discussed. It was shown that the simulation agreed reasonably well with observations and contained several features, such as an MCV and a RIJ, which are frequently seen in midlatitude MCCs.

In this chapter we will consider the results of the NLB diagnostic system which was developed in Chapters 3 and 4. In the next section, some of the details concerning the analysis domain and vertical coordinate transformation required to place the model data onto the analysis grid will be clarified. In Section 6.3, several definitions will be introduced in preparation for the discussion of the balanced analysis results in Section 6.4. Some aspects of the balanced analysis as a gravity-wave filter are examined in Section 6.5. In Section 6.6, we will briefly revisit the Rossby radius, λ_R, using information gained in the previous sections.

6.2 The Analysis Grid

The analysis grid (that is, the data volume upon which the PV inversion is performed) corresponds to a subvolume of Grid #2 (the first nested grid, see Chapter 5). To avoid potential problems with derived quantities which required horizontal differentiation, the lateral boundary points of Grid #2 were discarded, and to avoid possible noise due to the upper boundary, the top 5 model levels were discarded.

Recall that friction was neglected in developing the NLB system in Chapter 3. Since friction effects are most dominant near the surface, it would seem wise to eliminate points in the boundary layer. Unfortunately, the boundary layer in this simulation was, at times, several kilometers deep. As a compromise, the bottom 3 model levels of Grid #2 were also discarded. As explained below, this compromise is mitigated by other constraints on the analysis domain.

6.2.1 Interpolation of model data onto the analysis grid

RAMS utilizes the terrain-following vertical coordinate system σ_z, defined by (5.1), while balanced diagnostics are formulated with the Exner function, π, as a vertical coordinate. Thus, the RAMS model output must be vertically interpolated onto constant π surfaces. The horizontal spacing of the RAMS output was retained, and no horizontal interpolation was required.

Once the subset of model data outlined above is obtained, the bottom level was searched to find the minimum π value, and the top level was searched for the maximum π level. This defined the range of π (π_b and π_t, respectively) common to *all* grid columns in the model volume (x,y,σ_z) subset, and determined the bottom and top of the analysis (x,y,π) domain.[1] Once π_b and π_t were determined, a clamped cubic spline $z \rightarrow \pi$ interpolation (Burden et al. 1981) of each field in the data set was performed on each vertical column to place the model data on 16 evenly-spaced constant-π surfaces. The result was an analysis domain, 78 points E-W and 63 points N-S, with a horizontal spacing of 25 km, and 16 π levels, ranging from $\pi_b = 963$ J °K^{-1} kg^{-1} to $\pi_t = 500$ J °K^{-1} kg^{-1}, separated by a constant $\Delta\pi$ of 30.87 J °K^{-1} kg^{-1}. Table 6.1 lists the π levels, their millibar equivalents and a representative geometric height for each level, which was taken from a point near the center of the storm region at 23/1800.

Referring back to Fig. 5.2, which shows the lateral extent of the analysis domain and its underlying topography, it is seen that the highest terrain (and hence the lowest π on the σ_z = 4 level) is found along the western boundary and in the Appalachian, Ozark, and Smoky Mountains. While these areas of higher terrain have little areal extent, they determine the

1. In general, the pressure varies with time on any given π level, In practice, a π_b and a π_t must be determined which are appropriate for the *entire* collection of data sets for *all* times.

analysis level	π (J ^{o}K^{-1} kg^{-1})	pressure (mb)	height (m)
1	963.0	864.3	1387.8
2	932.1	771.3	2369.8
3	901.3	685.6	3360.2
4	870.4	607.0	4356.5
5	839.5	535.0	5361.3
6	808.7	469.3	6375.1
7	777.8	409.6	7396.8
8	746.9	355.5	8425.8
9	716.1	306.7	9462.6
10	685.2	262.9	10514.0
11	654.3	223.8	11586.4
12	623.5	189.0	12686.7
13	592.6	158.3	13828.3
14	561.7	131.3	15017.8
15	530.9	107.7	16257.1
16	500.0	87.4	17555.1

Table 6.1 *The π levels in the analysis domain and their mb equivalents. The fourth column lists, for reference, the associated geometric heights of each surface for a point near the midpoint of the Iowa/Missouri border at 23/180.*

lower boundary of the analysis domain, as no data exists below the surface. Since the region over which the storm occurred has significantly lower terrain, the bottom of the analysis domain is well (~ 1 km) above the surface in the region of greatest interest, making surface effects, such as friction, more justifiably neglected.[2]

6.3 Definitions of balanced winds and related quantities

For the purpose of discussing the results of the balanced analysis, it is useful to define several wind fields. *It shall be understood in the ensuing discussion that the vector winds are*

2. Unfortunately, much of the cold pool generated by the storm is also below the bottom of the analysis domain. This is unavoidable however, since the terrain to the west of the Missouri River, rises rapidly westward in Kansas. The alternative is to create bogus PV and surface data for those regions where the surface pressure is less than that found in the storm environment. This alternative, which introduces uncertainties of its own, was not considered acceptable.

the horizontal winds, unless otherwise stated. (The notational convention introduced in Footnote 1 on page 49 will be maintained here.)

Vector field decomposition can be achieved in a number of different and useful (and confusing!) ways. Here, we are interested mainly in what shall be termed the balanced ($\mathbf{V}_b$) and unbalanced ($\mathbf{V}_u$) winds, which when added together, produce the complete, two-dimensional, vector wind field ($\mathbf{V}_m$), as produced in the model. These components can then be further decomposed into their divergent and nondivergent elements, $\mathbf{V}_\Psi$ and $\mathbf{V}_\chi$ respectively. (Refer back to (3.10) and its accompanying discussion for the definitions of divergent and nondivergent winds.)

For the sake of intercomparison, it is also useful to decompose the *model* winds into their component nondivergent and divergent parts ($\mathbf{V}_{m\Psi}$,$\mathbf{V}_{m\chi}$). Recall from the discussion in Chapter 4 that computation of the nondivergent component of the model winds $\mathbf{V}_{m\Psi}$, via inversion of (4.10), was necessary to determine the lateral boundary conditions for Ψ in the Φ,Ψ solver. A similar Poisson equation, with the vertical vorticity ζ replaced by the horizontal divergence δ, was used to find the divergent component of the horizontal model winds, $\mathbf{V}_{m\chi}$. The sum of the decomposed winds, $\mathbf{V}_{m\Psi} + \mathbf{V}_{m\chi}$, agreed well with the model winds.

Similar to the definition of the ageostrophic winds in the context of geostrophic balance, the (nonlinearly) unbalanced winds are defined as the residual:

$$\mathbf{V}_u = \mathbf{V}_m - \mathbf{V}_b. \tag{6.1}$$

The same approach may be used to define the unbalanced nondivergent winds, $\mathbf{V}_{u\Psi}$, and unbalanced divergent winds, $\mathbf{V}_{u\chi}$. Table 6.2 contains a summary of these definitions.

In a like manner to (6.1), an unbalanced vertical velocity (ω_u) in the Exner function vertical coordinate system may be defined:

$$\omega_u = \omega_m - \omega_b, \tag{6.2}$$

COMPONENTS OF VECTOR WINDS:		
$V_u = V_m - V_b$	$V_{u\chi} = V_{m\chi} - V_{b\chi}$	$V_{u\Psi} = V_{m\Psi} - V_{b\Psi}$
$V_m = V_{m\Psi} + V_{m\chi}$	$V_b = V_{b\Psi} + V_{b\chi}$	$V_u = V_{u\Psi} + V_{u\chi}$
V_m *model wind*	V_b *balanced wind*	V_u *unbalanced wind*
$V_{m\Psi}$ *model nondiv.wind*	$V_{b\Psi}$ *balanced nondiv. wind*	$V_{u\Psi}$ *unbal. nondiv. wind*
$V_{m\chi}$ *model diverg. wind*	$V_{b\chi}$ *balanced diverg. wind*	$V_{u\chi}$ *unbal. diverg. wind*

Table 6.2 *Summary of definitions of the various two-dimensional wind fields used in the discussion of the balanced analysis. See (3.10) for a definition on "divergent" and "nondivergent" in terms of the velocity potential χ and the streamfunction Ψ.*

where ω_b satisfies the both continuity equation, (3.22), for the balanced velocity potential χ_b, and (3.24), the NLB omega equation.

It is also useful to define some bulk measures of the various wind fields. We can define a average kinetic energy per unit mass (KE) associated with the various wind fields:

$$KE_i = \frac{\int_\Omega (\rho/2)\,\vec{V}_i \cdot \vec{V}_i \, d\,\Omega}{\int_\Omega \rho \, d\,\Omega} \qquad \textbf{(6.3)}$$

where Ω represents a volume of integration and ρ the pseudo-density appropriate to the coordinate system. It should be borne in mind that the only true kinetic energy, in the physical sense, is that associated with the total model horizontal winds, $\mathbf{V}_m$. Due to the quadratic nature of (6.3), the sum of the unbalanced and balanced KEs, (KE_Ψ,KE_χ), *does not equal the total* KE_m *computed from the model winds.* In other words, $KE_m \neq KE_\Psi + KE_\chi$ and $KE_u \neq KE_{u\Psi} + KE_{u\chi}$. It is perhaps more correct to think of these quantities as the mass-weighted mean-square value of $\mathbf{V}_i$. These KEs are useful in that they supply a bulk

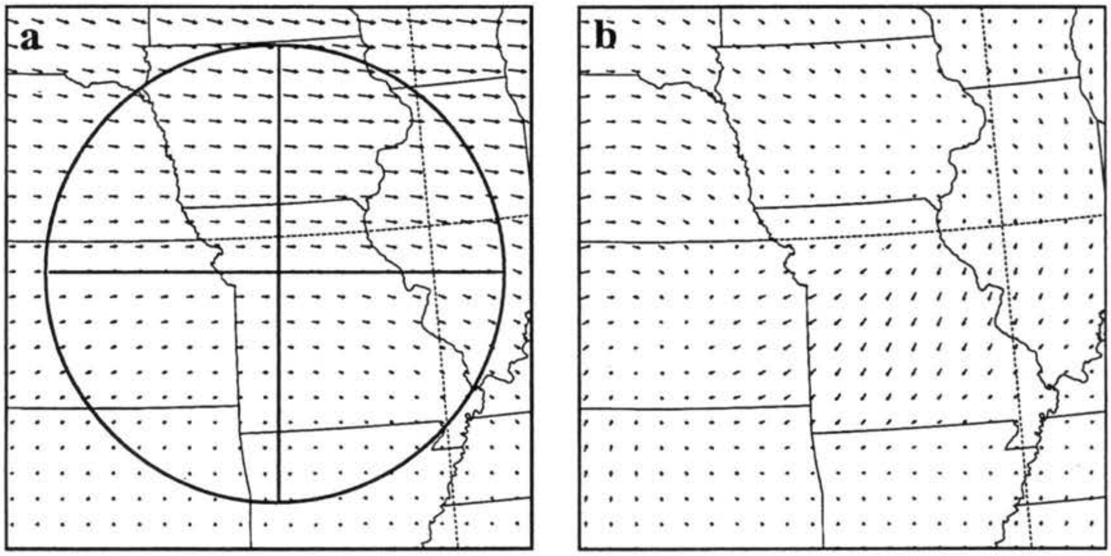

Fig. 6.1. *(a) The model winds at 23/1900 on the 535 mb pressure level. The maximum wind vector represents a speed of 29 m s^{-1}. (b) The unbalanced winds at the same time and level. The maximum wind vector represents a speed of 1.5 m s^{-1}. For comparison, the scaling between a and b is 10:1 (A vector in panel a would be 10 times larger in panel b). The ring in Fig. 6.1a shows the horizontal location of the averaging domain discussed later.*

measure of the relative significance of the various wind fields during the evolution of the simulated MCC.

6.4 Results of the Balanced Analysis

The central assumption implicit in the use of balanced models (e.g., the quasi-geostrophic model) for operational forecasting purposes is that the atmosphere remains quasi-balanced. Of course, this assumption is scale specific, its validity dependent on the scale of interest. The balanced-analysis approach allows for a quantitative verification of the quasi-balance assumption.

Fig. 6.1a shows $\mathbf{V}_m$, the model winds, on the 535 mb pressure surface at 23/1900, just before the first convection occurred. Fig. 6.1b shows $\mathbf{V}_m$, the unbalanced component of the model winds, at the same time and location. (The scale of wind vectors between the two figures is 10:1, i.e., a vector in Fig. 6.1a would appear 10 times larger in Fig. 6.1b). The largest unbalanced wind magnitude in the figure is about 1.5 m s^{-1}, compared to the

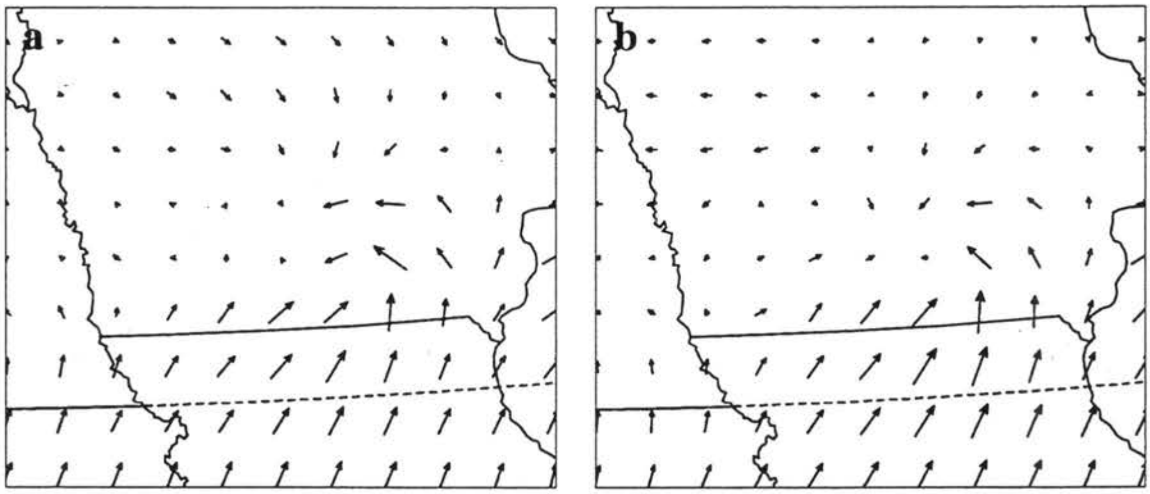

Fig. 6.2. *(a) The storm-relative model winds $\mathbf{V}_m$ and (b) the storm-relative balanced winds $\mathbf{V}_b$ on the 771 mb surface at 23/2200. The maximum wind vector represents a speed of 20 m s^{-1}. Storm motion for this and subsequent figures is U_s = 7 m s^{-1}, V_s = -5 m s^{-1}, unless otherwise stated.*

maximum model winds of almost 29 m s^{-1}. Before convection, the approximation of quasi-balance is obviously well met, at least at this level in the atmosphere.

Fig. 6.2a and b show vector plots at 771 mb of $\mathbf{V}_m$ and the $\mathbf{V}_b$, balanced winds, respectively, at 23/2200, after almost 3 hours of convection. The MCV circulation in south-central Iowa appears clearly in both plots. This should not be surprising, since these strong long-lived cyclonic circulations require a state of cyclostrophic balance in order to maintain temporal coherence (Davis and Weisman 1994). Cyclostrophic balance, a balance between the pressure gradient and centripetal forces, is the most basic balance for curved flow, and as such represents an exact solution to the nonlinear balance equation. Overall, the winds agree quite well, though there are some differences. The major difference between $\mathbf{V}_m$ and $\mathbf{V}_b$ is due to the unbalanced divergent winds, $\mathbf{V}_{u\chi}$, which comprise over 80% of $\mathbf{V}_u$ at this level.

Another feature of interest evident in Fig. 6.2 is the slight anticyclonic turning of $\mathbf{V}_m$, NNE of the MCV, which is not captured in $\mathbf{V}_b$. Recall that the PV was filtered previous to inversion to ensure that the ellipticity condition for NLB equation, PV > 0 was met. From the results of the PE model in Chapter 5 we saw that bands of negative PV were generated to the north of the convective elements. The filtering process by necessity caused these regions to be given very weak positive values of PV. This results in a local biasing of the PV inversion solution towards positive vorticity and represents a fundamental weakness of the balanced model paradigm. Since the PV inversion in a sense represents a double integration, it acts as a smoothing operator and works to mitigate the PV filtering, especially if the regions of negative PV are relatively confined.

PV is a conserved property in the inversion process in the sense that the resulting balanced wind and thermal structure yield the same PV produced by the model. *This does not mean that the same wind and thermal fields are recovered.* Rather, the agreement depends on how well the balance assumption is met. The filtering of negative PV also causes a disagreement, because the *model* fields, $\mathbf{V}_m$ and θ_m no longer agree with the positive-definite PV field used in the inversion. Fig. 6.3a shows the $\mathbf{V}_m$ wind vectors and relative vorticity ζ_m for the 535 mb level at 23/2200, while Fig. 6.3b shows the nondivergent component of the unbalanced winds, $\mathbf{V}_{u\psi}$, and the associated unbalanced vorticity,

$$\zeta_u = \zeta_m - \zeta_b. \quad \textbf{(6.4)}$$

The $\mathbf{V}_{u\psi}$ field shows a definite anticyclonic flow, in agreement with ζ_u in Fig. 6.3b, implying that $\mathbf{V}_b$ is *more* cyclonic than $\mathbf{V}_m$. For PV to be maintained, this would then necessitate that the balanced θ field is *less* stable than the model θ field. Fig. 6.3c shows the difference Brunt-Väisälä frequency,

$$N_u = N_m - N_b. \quad \textbf{(6.5)}$$

where

$$N^2 = -\left(\frac{g}{\theta}\right)^2 \frac{d\theta}{d\pi}. \quad \textbf{(6.6)}$$

As expected, $N_u > 0$ over most of this region, which implies $N_b < N_m$, i.e., the balanced θ field is *less* stable than the model fields.

This disagreement between the model and balanced fields may be the result of a number of factors besides the filtering process. Recall from Chapter 4 that the NLB approximation to

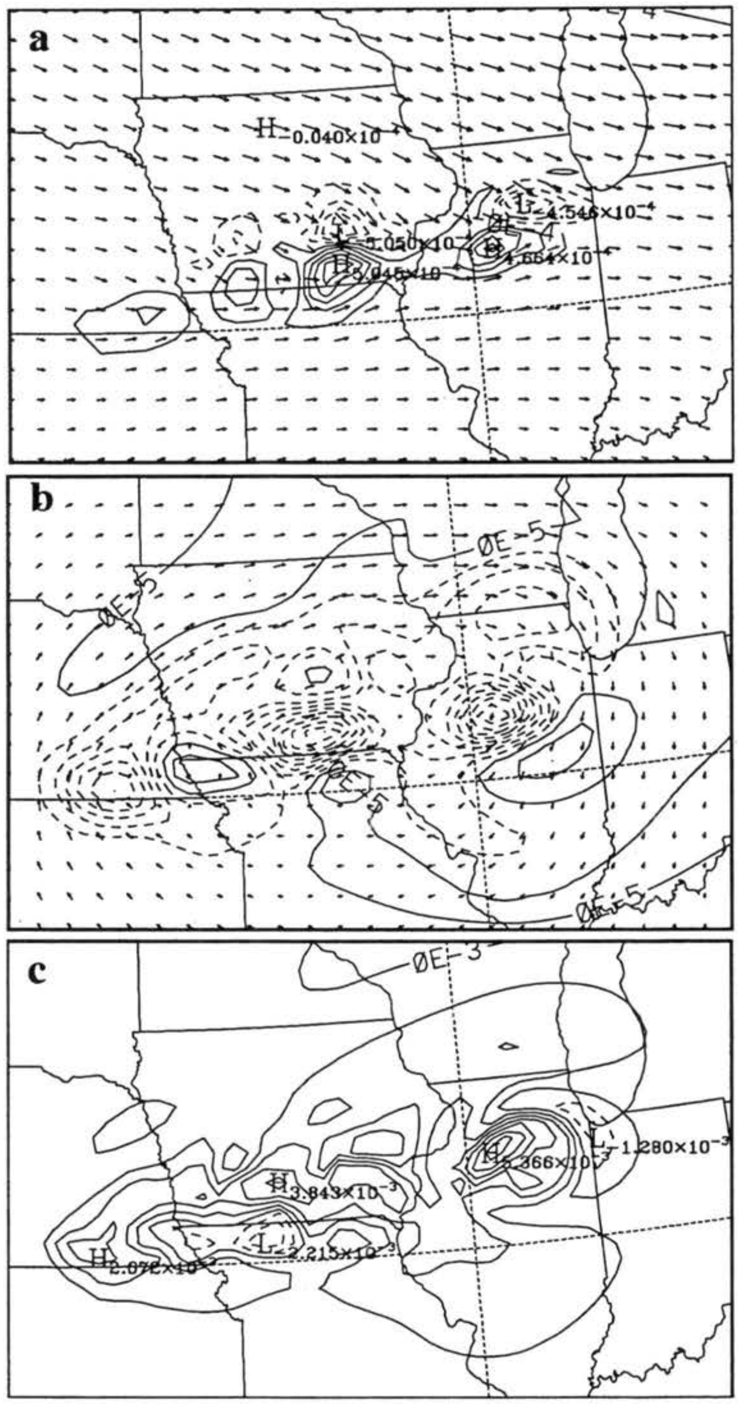

Fig. 6.3. *All plots at 23/2200 on the 535 mb surface. (a) The model winds, V_m, and relative vorticity ζ_m. The maximum wind vector represents a speed of 27 m s^{-1} The contour interval for the vorticity is 1×10^{-4} s^{-1}. (b) The unbalanced nondivergent winds, $V_{u\psi}$, and the associated unbalanced vorticity ζ_u. Here the maximum wind speed is 2.2 m s^{-1} and the contour interval, 0.5×10^{-5} s^{-1}. (c) The difference Brunt-Väisälä frequency N_u as defined by (6.5), contour interval of 8×10^{-4} s^{-1}.*

PV neglected $\partial \mathbf{V}_\chi/\partial z$, the vertical shear of the divergent winds. This resulted from the assumption $\varepsilon = \delta/\zeta << 1$, yet within the region of the convective line, $\varepsilon \sim O(1)$, and the assumption is clearly invalid. Davis and Weisman (1994) indicate that the neglect of this term may be the most significant drawback in simulating MCSs with an NLB model.

The hydrostatic assumption is also included in the NLB PV approximation, eliminating horizontal shear of the vertical winds ($\partial\omega/\partial x$, $\partial\omega/\partial y$). With vertical velocities in the convective updrafts of a few meters per second in close proximity to downdrafts of similar strength, this can also be a poor approximation near the squall line. There is a high spatial correlation between the extrema in ζ_u (Fig. 6.3b), N_u (Fig. 6.3c) and the positive vertical velocity at this level (not shown). In other words, these extrema are located in the region near the updraft and downdraft cores, where the motion is likely nonhydrostatic.

The difference between ζ_m and ζ_b locally exceeds 10%. This difference decreases rapidly with distance to the south but less rapidly to the north. The flow accelerating into the storm from the north has a strong divergent component which increases with height in the lower and midtroposphere. Again, this contribution to PV is neglected in the NLB approximation.

At later times, the model flow still remains largely balanced. Fig. 6.4 shows the wind vectors $\mathbf{V}_b$ and $\mathbf{V}_u$ on the 535 mb surface at 24/0430, when the storm is mature. The slight anticyclonic tendency of the unbalanced winds $\mathbf{V}_u$ (Fig. 6.4b) is still evident. The RIJ shows up well in the northerly component of the balanced winds (Fig. 6.4a) over Iowa. Since it was shown in Chapter 5 that the RIJ is associated with a strongly negative band of PV, the presence of this feature in $\mathbf{V}_b$ is somewhat of a surprise. Davis and Weisman (1994) found a balanced RIJ in their idealized simulations, but their environment contained no component of vorticity orthogonal to the squall line. Evidently the RIJ may be a reasonably balanced phenomenon associated with the circulation about the MCV, even though the dynamics leading to the balance may occur on the fast manifold. $\mathbf{V}_u$ also shows a weak (~ 4 m s^{-1}) jet-like flow along the Iowa/Illinois border. This unbalanced feature is rather atypical in that it was composed largely of $\mathbf{V}_{u\psi}$, the *nondivergent component* of the

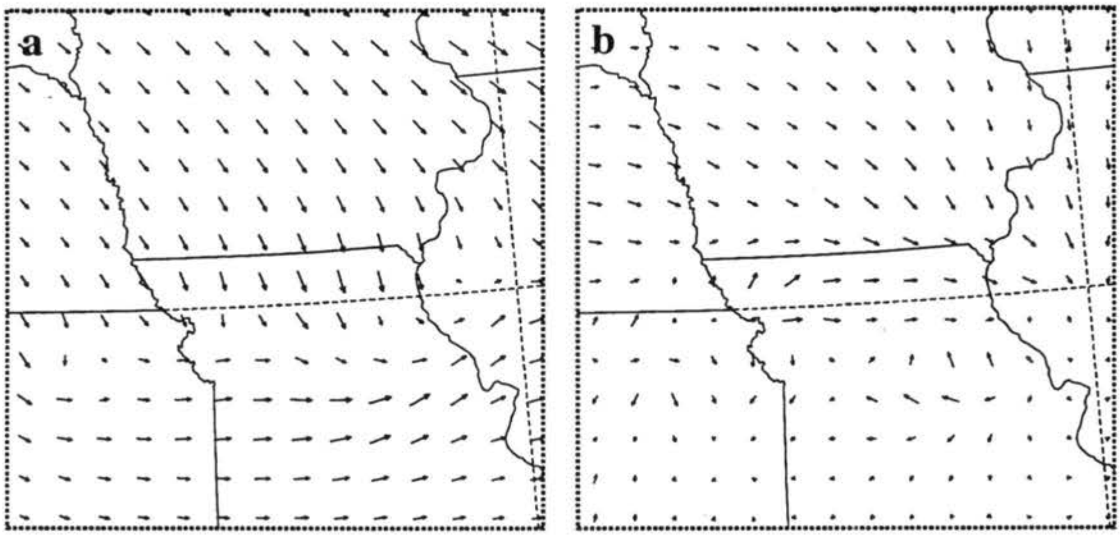

Fig. 6.4. *Both panels at 24/0430 on the 535 mb level. (a) The balanced winds $\mathbf{V}_b$. The maximum wind vector represents a speed of 30 m s^{-1}. (b) The unbalanced winds $\mathbf{V}_u$, maximum speed of 6.7 m s^{-1}.*

unbalanced flow. Though highly speculative, it may be that this jet is a consequence of inertial instability, reinforcing the balanced component of the RIJ.

6.4.1 Bulk characteristics of the unbalanced flow: KE analysis

To gain an understanding of the atmospheric balance of the storm region as a whole before convective initiation, it is useful to look at the ratio of the various volume-averaged quantities, KE_u, $KE_{u\Psi}$, and $KE_{u\chi}$, normalized by KE_m, the volume-average kinetic energy per unit mass. Using the appropriate wind fields, KE in (6.3) was computed at half-hour intervals, in an averaging volume whose horizontal projection is shown in Fig. 6.1a.[3] The (pressure) depth of the volume was that of the analysis domain (refer to Table 6.1). This stationary volume, with a radius of 450 km, was of sufficient horizontal extent to contain most of the vertical motion directly related to the MCC during its lifetime.

Fig. 6.5 shows the time evolution of these quantities. At 23/1900 (-5 hr on the ordinate in the figure), the top curve of the main plot in Fig. 6.5 shows that KE_u is only about 1% the

3. Several volume sizes were tried. Unless stated, the results presented in this section were relatively insensitive to the size of the averaging volume, though of course very large domains showed a smaller amplitude since they included more undisturbed model circulations.

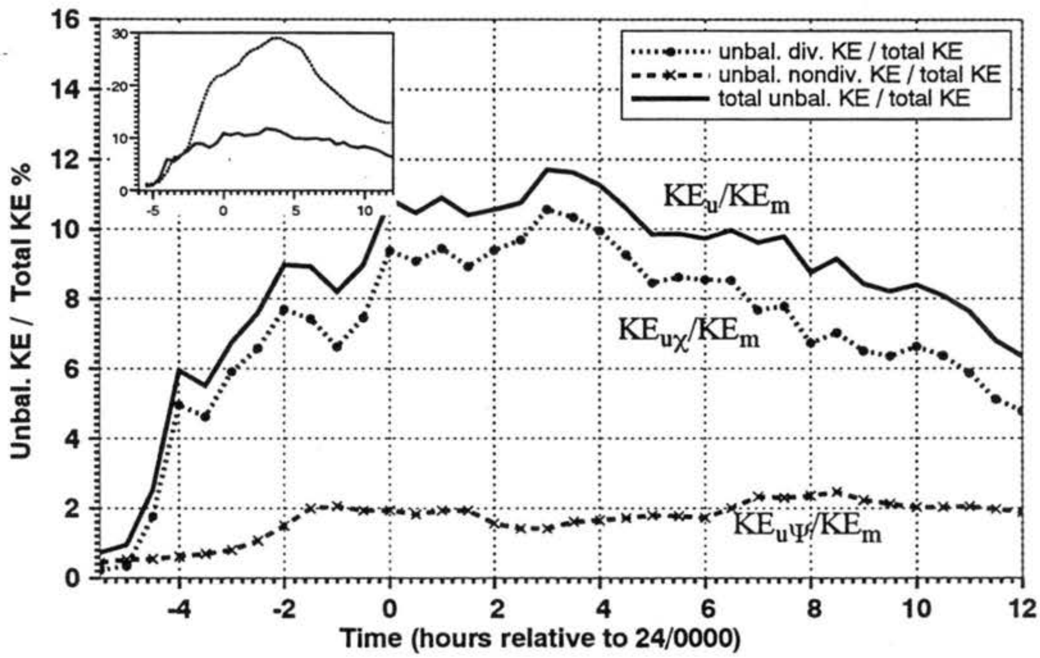

Fig. 6.5. *KE as defined in Eq. (6.3) normalized by the volume-average kinetic energy per unit mass, KE_m. The top (solid line) is KE_u, associated with the total unbalanced flow, $\mathbf{V}_u$. The dotted line with filled circles is $KE_{u\chi}$, associated with the unbalanced divergent flow, $\mathbf{V}_{u\chi}$. The bottom (dashed) line is $KE_{u\psi}$, associated with the unbalanced nondivergent flow $\mathbf{V}_{u\psi}$. The inset plot in the upper-left hand corner displays KE associated with the residual: $\mathbf{V}_R = \mathbf{V}_m - \mathbf{V}_{b\psi}$, i.e., the difference between the model winds and the balanced nondivergent winds. KE_u/KE_m, the top curve in the main figure, is plotted in the inset (bottom curve) for comparison. Note the scale difference on the abcissae. Refer to Fig. 6.1a for the location of the averaging volume.*

magnitude of KE_m, again in good agreement with the quasi-balance assumption. With the onset of convection, the ratio KE_u/KE_m quickly grew to several percent. At the time of maximum extent of the storm, between 24/0200 and 24/0400, KE_u/KE_m reached almost 12%. As the storm dissipated, the ratio slowly fell, decreasingly more or less linearly after 24/0730, when the convection had ceased. By the end of the simulation (24/1200), KE_u/KE_m was still over 6%, several times larger than the pre-convective value at 23/1900.

The dotted (middle) curve in Fig. 6.5, with the filled-circle symbols, shows the evolution of $KE_{u\chi}$ associated with $\mathbf{V}_{u\chi}$, while the dashed (bottom) curve shows $KE_{u\psi}$, associated with the unbalanced nondivergent winds. Throughout the time series, $KE_{u\chi}/KE_m$ closely tracks KE_u/KE_m, both in amplitude and trend. In comparison, $KE_{u\psi}/KE_m$ does increase, but only gradually, exceeding 2% for just a short period (24/0600 → 24/1000) near the end of the storm.

The unbalanced KE evolution shows several interesting features about the bulk flow behavior of the storm, the most obvious of which is that unbalanced flow is largely divergent. A significant pulsing is apparent as a ripple superimposed on the general trend of KE_u/KE_m. Even in the earliest stages of the storm development, from convective initiation to 23/2100, when the mesoscale divergent motions are largely contained within the averaging volume, this pulsing is apparent. This is not present in $KE_{u\psi}/KE_m$ and it is speculated that this higher frequency oscillatory behavior is likely associated with gravity wave motions. A similar pulsing was found in the two-dimensional MCC modeling studies of Tripoli and Cotton (1989).

The energy partitioning for simple harmonic motion oscillates between kinetic and potential energy (Goldstein, 1950). Recall that the data from the PE model represents an instantaneous "snapshot" of the model fields. If the gravity wave energy is dominated by one or 2 dominant modes,[4] the rippling in KE_u/KE_m may be due to the instantaneous phase of these dominant modes at the time they were sampled. It is possible that with a sampling averaged over the period of a buoyancy oscillation, this behavior would not be apparent.

Some balanced models (e.g., Raymond and Jaing 1990) neglect advection by $\mathbf{V}_{b\chi}$, the balanced divergent wind. The inset in the upper-left hand corner of Fig. 6.5 shows the normalized KE associated with the quantity $\mathbf{V}_m$ - $\mathbf{V}_{b\psi}$, the difference between the model winds and the balanced nondivergent winds. This quantity has a maximum approaching 30%. Obviously the balanced divergent flow $\mathbf{V}_{b\chi}$, is an important component of the total balanced winds. (Recall that KE_u is calculated using the residual $\mathbf{V}_m - (\mathbf{V}_{b\psi} + \mathbf{V}_{b\chi})$. This is the top curve in the main figure and also appears for reference in the inset figure as the lower curve.). Any balanced model which neglects advection by $\mathbf{V}_{b\chi}$ will have significant errors in regions of strong convection.

4. Evidence is presented in Section 6.5 that this may be so.

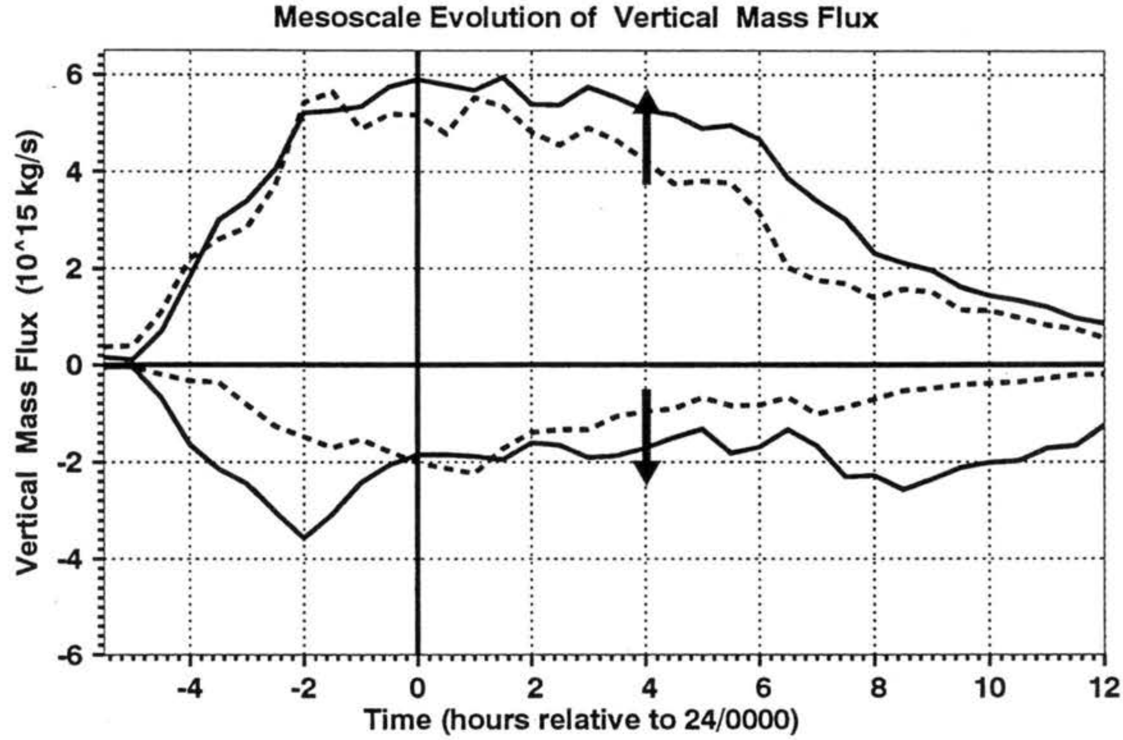

Fig. 6.6. *Area-averaged upward and downward vertical mass flux (10^{10} kg s^{-1}) through the 535 mb surface. The solid lines indicate the fluxes by ω_{mb} and dotted lines, mass fluxes by ω_b. The time axis is the same as Fig. 6.5. The averaging area is indicated on Fig. 6.1a.*

6.4.2 Area-averaged vertical fluxes in the midtroposphere

The area-averaged vertical mass flux through the midtroposphere provides a good bulk measure of the agreement between the model vertical motion, ω_m, and the balanced vertical motion, ω_b. Fig. 6.6 shows the area-averaged upward and downward mass flux through the 535 mb surface as a function of time. What is most apparent in this figure is that the upward flux from both ω_m and ω_b exceeds the downward flux during the almost the entire lifetime of the storm.[5]

The positive vertical mass fluxes, $\phi_{m+} = \overline{\rho\omega}_{m+}$, $\phi_{b+} = \overline{\rho\omega}_{b+}$, are almost identical during the first three hours of convection, with ϕ_{b+} actually exceeding ϕ_{m+} between 23/2200 and 23/2300. After 23/2300, ϕ_{m+} exceeds ϕ_{b+} for the duration of the simulation. The largest values of both ϕ_{m+} and ϕ_{b+} occur between 24/0000 and 24/0130, and then decrease only gradually until around 24/0600, when the convective line rapidly begins to weaken.

The period of maximum storm extent, at around 24/0230, does *not* correspond with the greatest positive vertical mass flux. At this time, the convective updrafts are weaker, although they have greater areal coverage than 2 hours earlier. By this time, surface temperatures have started their diurnal downward trend, lowering CAPE values. Also, the thermal stabilization of the midtroposphere and the strengthening mesohigh near the tropopause both act to dampen upward vertical motion.

It is interesting to note that the *unbalanced* upward mass flux,

$$\phi_{u+} = \phi_{m+} - \phi_{b+},$$

increases from 24/0100 onward until 24/0700, well into the dissipating stage of the MCC. During this time, the stratiform region of the storm is enlarging. Concurrently, below the stratiform region, the rear inflow is developing as precipitation evaporates into the dry mid-level air. This broad region of cooling modifies the mean vertical profile of the heating function, $Q(z)$. A change in heating function, $dQ(z)/dt$, has been shown to produce gravity waves (Emanuel 1983; Mapes 1993; see also the discussion in Section 6.5.2). The increase in both ϕ_{u+} and the unbalanced downward flux, ϕ_{u-}, correlates well with the development of a much more complex $Q(z)$. By 24/0800, $Q(z)$ is dominated by evaporative cooling and ϕ_{u+} slowly decreases as the waves propagate out of the averaging domain (look ahead to Fig. 6.8d for plots of area-averaged $Q(z)$). Fig. 6.7 shows ω_m, ω_b, and ω_u at the 535 mb level at 24/1000. The dashed (negative) contours in panels (a) and (b) show the remnant updrafts from the convection in Kansas at western end of the line. The ω_m field in

---

5. It should be noted that as the storm matured, a large anvil cloud developed to the north and east of the convective line as a result of the considerable westerly shear above 7000 m. The evaporative cooling of over -10° C h^{-1} below this anvil cloud forced mesoscale downdrafts. Due to the easterly dislocation of these downdrafts relative to the convective updrafts, an increasingly large amount of diabatically-forced downward motion occurred outside the averaging domain after 24/0700. Before this time, almost all the vertical motion directly induced by diabatic processes occurred within the domain. This effect can be seen in the decreasing magnitude of ϕ_{b-} in Fig. 6.8 after 24/0700.

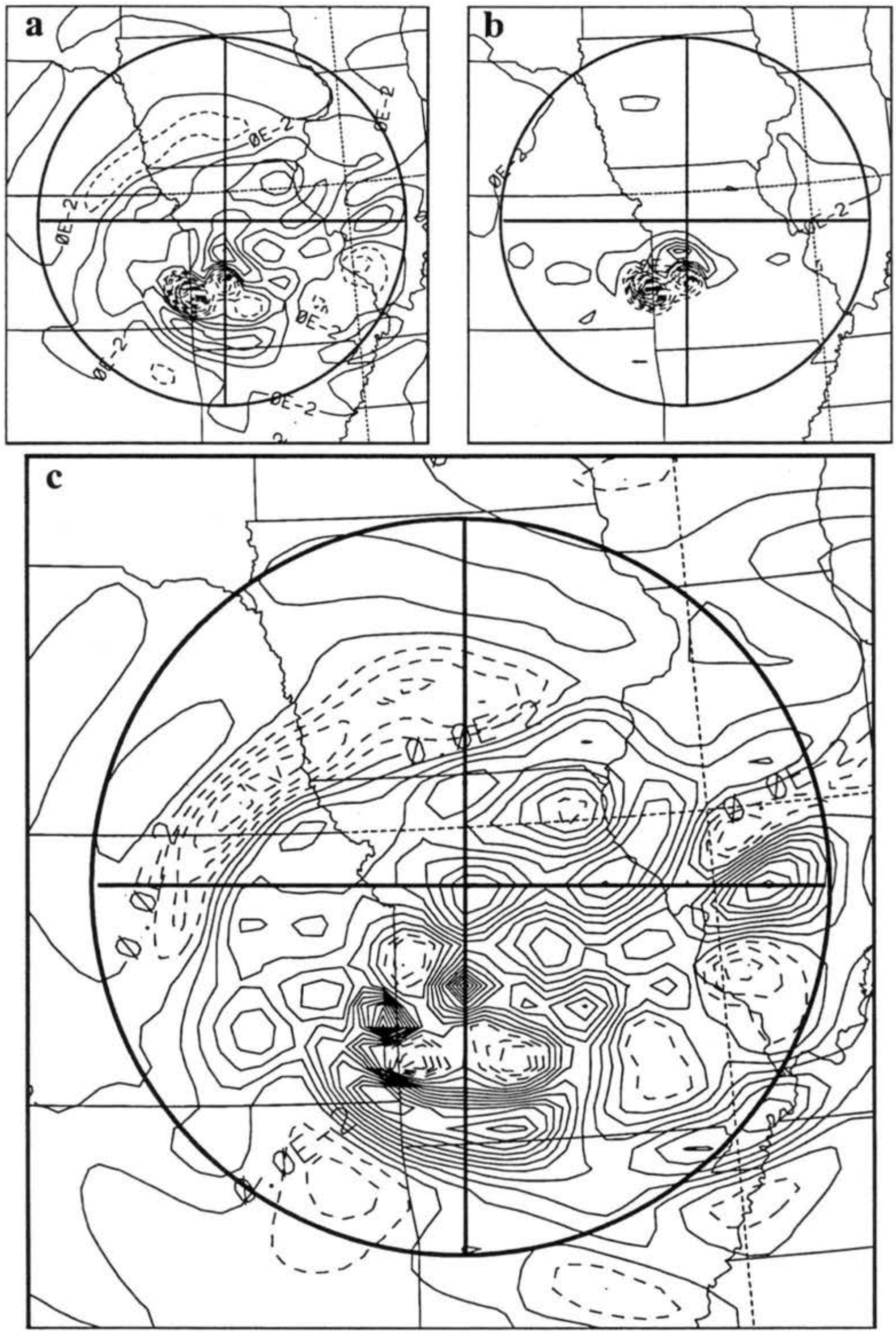

Fig. 6.7. *All plots at 535 mb and 24/1000. (a) Model vertical motion, ω_m, and (b) the balanced vertical motion, ω_b, and (c) the unbalanced vertical motion, $\omega_u = \omega_m - \omega_b$. The contour level in panels a and b is $2.5 \times 10^{-3}\ m^2\ {}^\circ K^{-1}\ s^{-3}$, and for panel c, $1 \times 10^{-3}\ m^2\ {}^\circ K^{-1}\ s^{-3}$. The ring shows the boundary of the averaging domain.*

panel (a) shows a periodic structure superimposed over large-scale subsidence (solid contours indicate negative vertical motion), while ω_m in panel (b) reveals only the decaying updraft and a related region of trailing subsidence. In Fig. 6.7c, ω_u reveals even more clearly the very periodic gravity-wave nature of the unbalanced vertical motion. Note that some of the wave pattern is now SE of the averaging domain.

The downward mass fluxes in Fig. 6.6, ϕ_{m-} and ϕ_{b-}, show considerably less consistency than their positive counterparts. The downward model mass flux, ϕ_{m-}, rapidly increases from the time of the first convection until 23/2200, corresponding to the brief period when $\phi_{b+} > \phi_{m+}$. After this time, ϕ_{m-} dramatically weakens, remaining more or less constant through the rest of the storm lifetime. By contrast, ϕ_{b-} gradually increases in magnitude from the time of first convection until 24/0130 and then slowly returns to near zero by the end of the simulation. The time evolution of ϕ_{b-} generally resembles a smaller amplitude, inverse image of its positive counterpart ϕ_{b+}.

The foregoing discussion suggests that the dynamics forcing upward motion within the averaging domain are different from those which drive the downward motion. The relatively close agreement between ϕ_{m+} and ϕ_{b+} indicates that the main driving process for *updraft* motion, latent heat release resulting from cloud microphysical processes, has a significant component of balanced motion and is well-represented in the NLB ω-equation. By contrast, the inconsistency between ϕ_{m-} and ϕ_{b-} indicates that the dynamics driving *downward* motion within the averaging domain are poorly represented in that equation. The location of the balanced downdrafts causing the modest ϕ_{b-} seen in Fig. 6.6 correlate well with the evaporative cooling behind, and to the east, of the convective line. The quite different behavior of ϕ_{m-} indicates that the PE model is responding to more than the direct diabatic forcing felt by the balanced ω equation.

The difference between ϕ_{m+} and ϕ_{m-} graphically illustrates an important aspect of the so called "compensating subsidence" (i.e., that downward motion necessary to maintain continuity in a large-scale integrated sense):

Mass flux locally forced in buoyantly-driven updrafts results in downward motion on a much greater scale.

The difference between ϕ_{m-} and ϕ_{b-} highlights another point:

The mechanisms by which compensating subsidence occur are largely fast manifold processes not *contained in balanced model theories, which exclude gravity and acoustic wave motion.*

As mentioned in Chapter 1, the nature of compensating subsidence has lately received attention in several studies (e.g., Bretherton and Smolarkiewicz 1989; Nicholls et al. 1991; Mapes 1993). Emanuel (1983) has shown that linear gravity waves, when averaged over a wavelength, do not transport heat or modify the mean state of their supporting medium implying that linear gravity waves are *not* the agents of mass adjustment due to convection. Results of Bretherton and Smolarkiewicz (1989) and Nichols et al. (1991), for a non-rotating atmosphere at rest, have shown that the disturbances forced by the initiation or termination of an imposed heating function (i.e., a non-zero dQ/dt as discussed above) have the propagation mode associated with gravity waves. Therefore, results from gravity-wave theory are applicable (Mapes 1993). The predicted *horizontal* gravity-wave propagation speed for a wave with vertical wavenumber m,

$$c_x = N/m, \tag{6.7}$$

is indeed found by Nichols et al.

Mapes also notes that, unlike classical linearly-superimposed gravity waves, these propagating "buoyancy bores" *do not* have a spatial or temporal periodicity and *do* leave a permanent net horizontal displacement in the fluid through which they propagate. These bores then must transport (rearrange) mass in a stratified fluid, and evidently represent the agents of compensating subsidence, enabling the fluid to recover a state of mass equilibrium. Because of their gravity wave-like nature, these bores would not be encompassed by balanced models. This may explain the differing behavior of ϕ_{m-} and ϕ_b in Fig. 6.6.

The neglect (filtering) of gravity wave oscillations by balanced models is equivalent to the assumption that $c \rightarrow \infty$ in (6.7), i.e., that gravity waves radiate away to infinity immediately, leaving behind only the slow-manifold, balanced flow. However, the volume integral of (3.22), the continuity equation, must be satisfied, and the compensating subsidence must almost immediately occur in a more *global* sense, being spread over a much larger domain. The midtropospheric ω_b does seem to show evidence of weak subsidence across a very large region of analysis domain which is superimposed on the direct diabatically-induced vertical motion.

Mapes showed that the passage of this buoyancy bore causes what he terms "area contraction", i.e., a large-scale low-level convergence. This modification of a large region surrounding an MCS would be favorable to new MCS formation, perhaps leading to "gregarious convection", This transient *is not* represented in the NLB model, and demonstrated another potential limitation of balanced modeling of phenomena driven by conditional instability.

In an infinite, inviscid, nonrotating domain, the PE solution might be expected to asymptotically approach the balanced result, as the buoyancy bore radiates off to infinity, leaving no trace of itself in the winds or temperature structure of the fluid. Gravity waves in a rotating fluid, however, become modified (deformed) as they propagate away from their source, the length scale over which this occurs being the Rossby radius (or "radius of deformation"), λ_R. The irreversible, horizontal displacement of the fluid (see Mapes 1993, Fig. 1) caused by the passage of the bore implies a vertically varying, horizontal motion which in turn, requires a balancing horizontal temperature gradient (Gill 1982). The buoyancy required by the balancing horizontal thermal structure comes from the bore itself. Hence, the bore becomes, in a sense, absorbed, as it propagates outward, leaving energy behind in the adjustment process.

The rotational dynamics which scale with λ_R are contained in the NLB equation set. This suggests a length scale or "*e*-folding" length governing the balanced compensating subsidence in the balanced ω equation.

6.4.3 Averaged Divergence Profiles.

Before leaving the discussion of the divergent flow, it is instructive to consider some vertical profiles of the average horizontal mass-flux divergence,

$$\overline{D}_i(z) = \frac{\int \nabla \cdot \rho \vec{V}_i \, dA}{\int dA} \qquad i = m, b \tag{6.8}$$

for each of the levels in the averaging volume. Fig. 6.8 shows such 2-hour time-average profiles centered at 24/2000, 24/0400, and 24/0800. The solid line in each panel is the model mass-flux divergence, $\overline{D}_m$, and the dashed line, $\overline{D}_b$, the mass-flux divergence associated with the balanced wind.

The first 2 times (24/0000 and 24/0400) reveal several of the same features. As expected, both $\overline{D}_m$and $\overline{D}_b$ show convergence at lower levels, with divergence in the upper half of the troposphere. The level of maximum convergence (~2500 m) is the same for both $\overline{D}_m$and $\overline{D}_b$. $\overline{D}_b$ consistently shows a level of maximum divergence somewhat lower and weaker than $\overline{D}_m$. $\overline{D}_b$ also shows weaker convergence at the lowest level throughout the convective portion of the storm. In general however, the balanced divergence and model divergence profiles at 24/0000 and 24/0400 are in good agreement and show strong similarities to observed MCS divergence profiles (e.g., Fig. 2 of Mapes 1993 and Fig. 12 of Cotton et al. 1989).

At 24/0800 (Fig. 6.8c), $\overline{D}_m$and $\overline{D}_b$ show much poorer agreement. By this time, the latent heating has largely ceased, with the exception of 2 confined regions near the decadent squall line. The average heating function, $\overline{Q}(z) = \overline{d\theta/dt}$, (Fig. 6.8d) has changed significantly from 24/0400 to 24/0800. The level of maximum convergence for the model flow has moved upward to 5000 m from 2500 m earlier. $\overline{D}_m$ is now positive (divergent) at the lowest level while $\overline{D}_b$ shows its strongest convergence there. The source air for the balanced updrafts is still being drawn from the lowest few levels, while the model is entraining air from somewhat higher levels. The model surface wind fields (below the bottom of

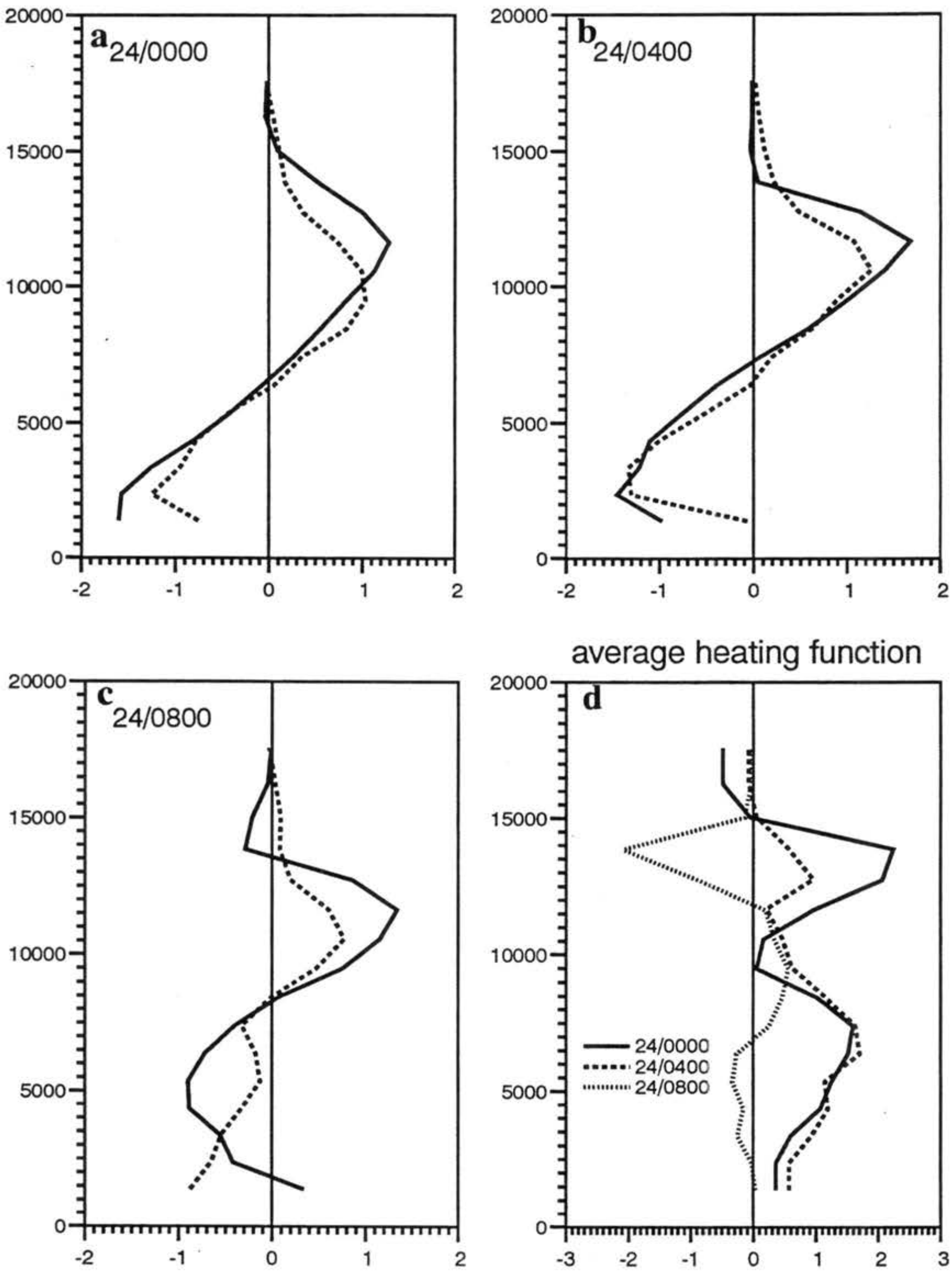

Fig. 6.8. *2 hour average horizontal mass flux divergence profiles (10^{-5} kg m^{-3} s^{-1}) at (a) 24/0000, (b) 24/0400, and (c) 24/0800. In each of the figures the solid line is the mass flux divergence from the model, while the dashed line is the balanced mass flux divergence. The vertical axis is meters AGL. (d) The area-averaged heating function, $Q(z)$ ($^{\circ}$C h^{-1}), for the same 3 times as the divergence profiles.*

the balanced-analysis domain) have a strong flow of relatively cool air away from the storm.

Throughout the evolution of the MCC, $\mathbf{V}_b$ showed a systematic tendency to have a lower level of maximum divergence relative to $\mathbf{V}_m$. While the divergence profiles show a very pronounced maximum in $\overline{D}_m$ which remains at a height of about 11500 m, $\overline{D}_b$ shows a less pronounced maximum at about 10000 m. In the PE model, the detrainment from the updrafts occurred over a very thin level, just at the tropopause, creating the sharply-peaked maximum of $\overline{D}_m$. This difference could have important cumulative consequences, which will be discussed further in the next section.

6.5 Some aspects of the unbalanced flow.

In Section 6.4 we considered the behavior of the balanced flow and its agreement relative to the flow produced by the PE model. It was seen that the balanced flow to a large degree dominated the mesoscale circulations, throughout the lifetime of the MCC. In this section we will examine some of the characteristics of $\mathbf{V}_u$, the unbalanced component of $\mathbf{V}_m$.

6.5.1 Advection by the unbalanced wind

Wind vectors of $\mathbf{V}_u$ and contours of PV at 24/0700 are shown for the 189 mb level in Fig. 6.9. The region of PV ≤ 0 is indicated by the hatching. Recall from the conceptual model of convective PV modification in Chapter 2 that a negative PV anomaly is expected near the tropopause. The 189 mb level, is at about 11500 m, the level of maximum $\mathbf{V}_m$ divergence in the profiles in Fig. 6.8. Inspection of the wind vectors in Fig. 6.9 reveals that $\mathbf{V}_u$ is dominated here by its divergent component, $\mathbf{V}_{u\chi}$. This height consistently shows the poorest agreement between $\mathbf{V}_m$ and $\mathbf{V}_b$, throughout the lifetime of the MCC.

The component of $\mathbf{V}_u$ up the PV gradient indicates that the unbalanced flow is doing a considerable amount of the horizontal PV advection. This unbalanced advection of PV suggests prognostic balanced models, even those which advect with a divergent as well as nondivergent balanced wind, might systematically under-predict the horizontal extent of

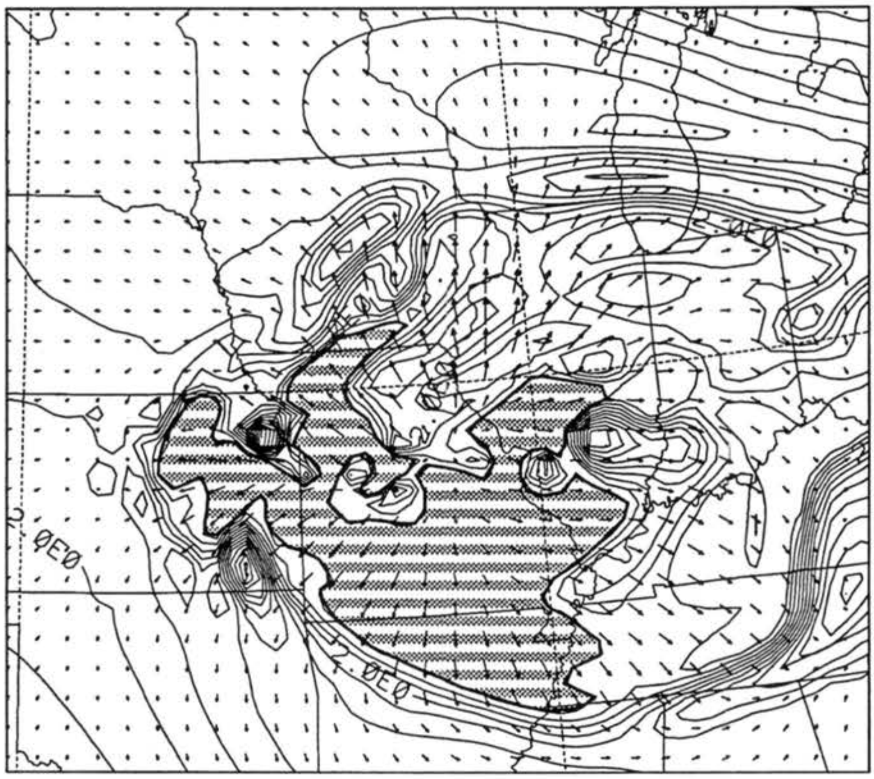

Fig. 6.9. *V_u, the unbalanced winds and PV at 189 mb, 24/0700. The maximum wind vector is 14.8 m s^{-1}, and the positive PV is contoured at 0.5 PVU increments. The negative PV is denoted by the horizontal hatching.*

the negative anomaly aloft, compared to PE models. While $\mathbf{V}_u$ does contain a periodic, gravity wave-like structure, averaging the unbalanced PV flux divergence computed with the *unfiltered* PV field ($\nabla \cdot q\mathbf{V}_u$) over the entire region of the area of the PV perturbation at this level revealed a PV tendency of about -0.3 PVU h^{-1}. This suggests that a consistent under-prediction of this flux could lead to substantial cumulative errors in PV distribution.

Near the tropopause, convection-induced PV tendencies are dominated by advection, i.e., the nonadvective flux term on the r.h.s. of (2.5) is small. Therefore, PV, like water substance, acts as a more or less conservative property at this level. Indeed, the strong PV gradient in Fig. 6.9 is co-located with the cloud boundary at this level. Hence, one might expect not-inconsequential advection of cloud material by $\mathbf{V}_u$ as well. Through radiative processes, under-prediction of the anvil-cloud extent by balanced predictive models could have a feedback on the large-scale energy balance of the surrounding environment.

The tropopause region also has, in the horizontally area-averaged sense, a large $\mathbf{V}_{u\Psi}$, as compared to other levels. This is likely the result of the PV > 0 constraint to ensure ellipticity in the Φ,Ψ solver. This region of negative PV is also inertially unstable, an instability whose dynamics are not encompassed within the NLB system. Since the hatching in Fig. 6.9 represents that region where PV is artificially forced to be just slightly positive, one would expect $\mathbf{V}_{b\Psi}$ to be more cyclonic over this entire region than $\mathbf{V}_{m\Psi}$ and this is the case.

6.5.2 Use of NLB diagnostics as a gravity wave filter

A consequence of neglecting divergent motion in NLB is that the resulting balanced model does not "see" gravity waves, a fact reinforced by the discussion in Sections 6.4.2 and 6.4.3 and borne out in the periodic structure of ω_u over Iowa in Fig. 6.7c. Historically, balance approximations were referred to as filtering approximations, as they "filtered" out behavior (e.g., gravity waves, acoustic waves, Lamb waves) deemed undesirable in a numerical model (Haltiner and Williams 1980; Holton 1992). The elimination of this "non-meteorological" noise motivated the quotations of Charney in Chapter 1.

As seen in Fig. 6.7c, the subtraction of a balanced field from its PE model counterpart provides a residual or unbalanced field, dominated by fast-manifold gravity wave-type motions.[6] Before the divergent motions become complicated by interfering waves of differing wavelengths, the filtering capacity is quite evident, even in the unbalanced horizontal winds. Fig. 6.10a shows $\mathbf{V}_{u\chi}$ at 24/2200 on the 685 mb surface. The gray shading on this plot indicates broad regions of weak unbalanced positive mesoscale vertical motion[7]. Fig. 6.10b shows δ_u, the unbalanced divergence corresponding to $\mathbf{V}_{u\chi}$. Away from the

6. It has already been noted that the concepts "fast manifold" and "slow manifold" are, at best, heuristically defined. Even with this ambiguity as a buffer, it is probably not correct to equate "fast-manifold", "gravity waves" and "unbalanced flow", as defined here. The residual fields being called "unbalanced flow" also inherently contain the cumulative errors from discretization and interpolation in addition to the errors resulting from numerical solution technique, the approximate boundary conditions, and the neglect of vertical shear of divergent flow in the NLB PV approximation. Another possibility is that the residual nondivergent flow seen in the unbalanced fields may also be "balanced" at a more sophisticated level of approximation than NLB.

7. Some strong convective downdrafts do exist within the shaded regions, which denote only the general mesoscale vertical velocity pattern.

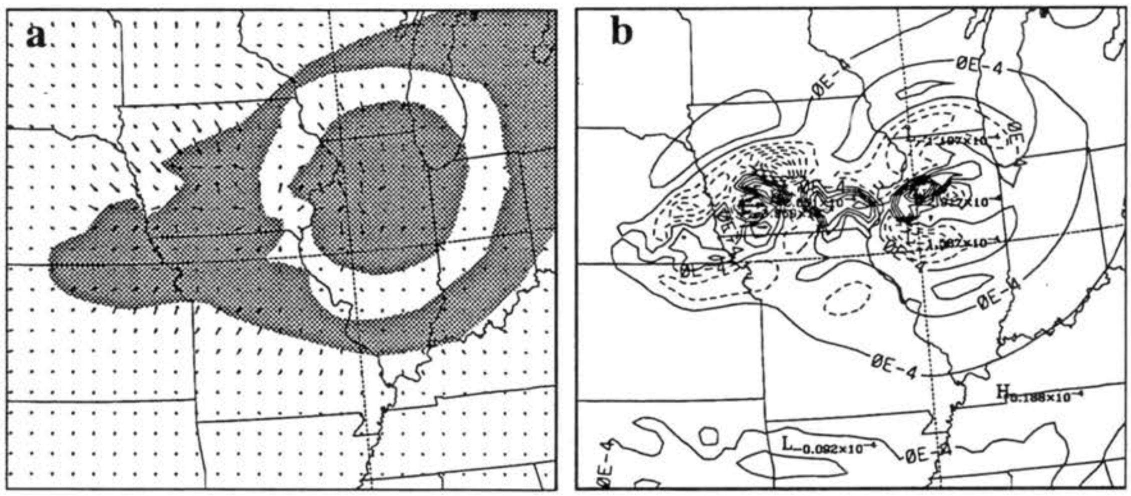

Fig. 6.10. *(a) The divergent component of the unbalanced winds* $\mathbf{V}_{u\chi}$ *(23/2230) at 685 mb. The maximum wind vector length represents 6.5 m* s^{-1}*. The gray shading indicates regions of unbalanced positive mesoscale vertical motion in* ω_u *(some negative vertical motion associated with the convective downdrafts exist in the shaded region). (b) The divergence field associated with* $\mathbf{V}_{u\chi}$*. Contours for the divergence are* 8×10^{-5} s^{-1}*.*

convective region of the storm, the mesoscale vertical motion, $\mathbf{V}_{u\chi}$ and δ_u all show a radially symmetric pattern of what appears to be gravity-wave induced divergent flow. The center of this wave pattern is over Illinois, and is related to the first convective pulse, which occurred over eastern Iowa between 23/1900 and 23/2030. The quasi-radial vertical motion pattern shows some deformation from symmetry as the wave pattern differentially advects eastward in the horizontal sheared flow ($+\ \partial u/\partial y$) across Iowa and N Illinois.

$\mathbf{V}_{u\chi}$ has its largest values close to the convective line, where the NLB system systematically produces less mid-level convergence than the model (see Fig. 6.8). At this time, 3 hours after convection has started, the divergence and difference vertical motion fields seem to be dominated by a few vertical modes. At later times, as the storm has matured, and several interfering gravity wave modes are present at finite amplitude, these fields become much more complex and very difficult to interpret.

An even clearer example can be obtained from Fig. 6.11 which shows ω_u at 23/2200 (same time as Fig. 6.10) on the 607 mb surface. The contouring has been limited to the range $-0.5 \times 10^{-3} \rightarrow 5 \times 10^{-3}$ $m^2 s^{-3}$ °K^{-1} to emphasize the periodic motion. At this time, the mesoscale ω_u is the combination of two superimposed nearly radially-symmetric wave

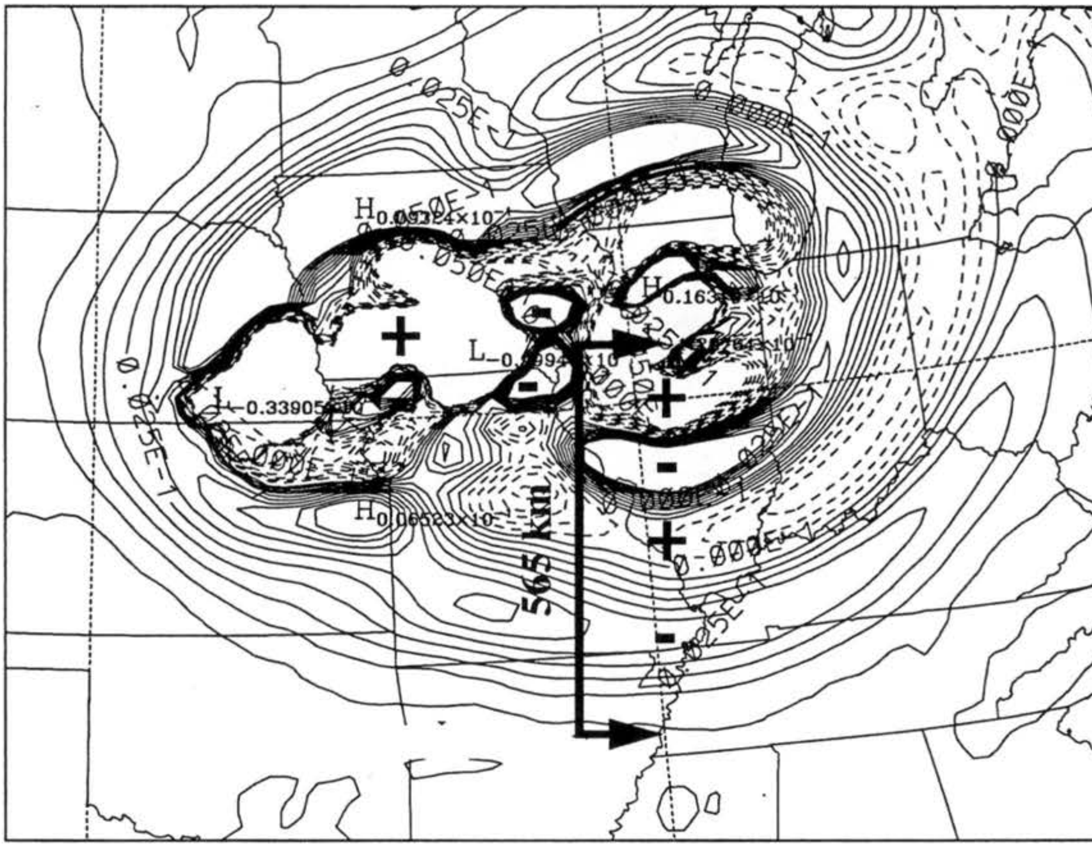

Fig. 6.11. *The unbalanced vertical velocity* ($\omega_b = \partial\pi/\partial t$) *at 23/2200 on the 607 mb surface. The contour level is* $5 \times 10^{-4}\ m^2\ s^{-3}\ {}^{\circ}K^{-1}$. *The contouring has been limited to the range* $-5 \times 10^{-3} \rightarrow 5 \times 10^{-3}$ *to emphasize the wave-like vertical motion at distances well removed from the convective region. The "+" and "-" signs denote regions of upward and downward motion, respectively. (In the* π *vertical coordinate, positive values imply negative vertical motion.) The bold double ended arrow indicates the approximate distance the leading wave-front has propagated in the three hour period since convection began.*

patterns. The western source has not been in existence as long and as a result the first outgoing wave has not propagated out as far as the eastern pattern.

The filtering ability of the balanced analysis is useful in comparing some aspects of the unbalanced flow behavior to that predicted by fast-manifold dynamics. An example is the problem of convective mass adjustment or compensating subsidence touched upon in Section 6.4.2.

Mapes (1993) theorized that a heating profile, typical of tropical MCSs, given by

$$Q(z) = Q_0 [\sin(\pi z/H) + \sin(2\pi z/H)/2], \tag{6.9}$$

would produce a divergence profile of the form:

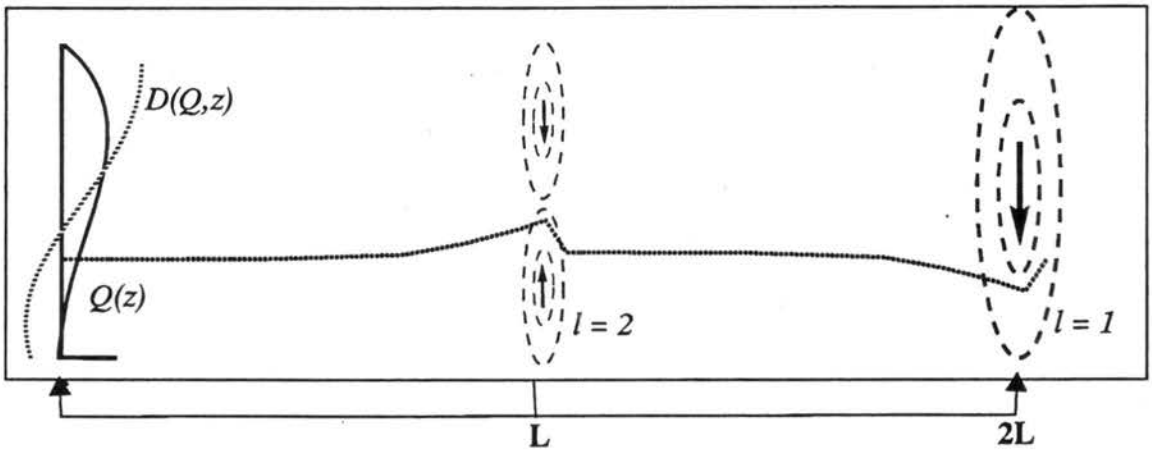

Fig. 6.12. *Schematic depiction of the results of Mapes (1993). The plot on the left shows the heating function Q(z) (solid) and the resulting divergence profile D(Q,z) (dotted). After a propagation time τ, the bores have traveled L and 2L respectively. The dashed line indicates the relative displacement of a surface in the lower half of the domain.*

$$D(Q, z) = \frac{-\pi\rho Q_0}{HN^2}[\cos(\pi z/H) - \cos(2\pi z/H)/2]. \qquad \textbf{(6.10)}$$

In (6.9) and (6.10) $\pi \approx 3.14159$, N is the Brunt-Väisälä frequency, and H is the depth of the domain. A sketch of *Q(z)* and *D(z)* appear to the far left in Fig. 6.12. The shape of the idealized divergence, *D(z)*, agrees quite well with the lower two thirds of the "early-MCC" divergence profile in Fig. 6.8a.

Switching on Q in a stratified atmosphere should result in a gravity wave motion corresponding to two lowest-order vertical modes. The gravest mode, of vertical wave number 1/2 (Mapes's $l = 1$ bore), resulting from the first term in (6.9) would be a half sine wave of negative vertical motion: $-w_0\sin(\pi z/H)$. while the second mode, with vertical wave number 1 (l = 2) would consist of an up-and-down couplet.

The phase and group speed of a linear gravity wave are given by (6.7), where the vertical wavenumber $m = H\pi/\mathrm{n}$, H is the height of the domain, n is a positive integer, and N is Brunt-Väisälä frequency. Mapes' $l = 2$ bore, with twice the wavenumber of the $l = 1$ bore, would travel only half as fast. Using the equations developed by Bretherton and Smolarkiewicz (1989), Mapes calculated the displacement of a surface, $\Delta z(r,t)$, for the radially-symmetric case. His results are summarized in Fig. 6.12. After a propagation time τ, the bores have traveled L and $2L$, where $L = c_2\tau$, c_2 being the propagation speed of the higher order bore. Using $N = 10^{-2}\ s^{-1}$ and $c = 50\ m\ s^{-1}$, Mapes found $2L$ to be about 550 km (see his Fig 4). The horizontal dotted line in Fig. 6.12 depicts the deformation of a surface somewhat below the vertical midpoint of the domain.

The clear gravity wave pattern in Fig. 6.11 permits an application of this theory to the PE simulation. From Fig. 6.11 we can see that, to the south, the leading edge of the storm-induced vertical motion is about 565 km from the center of the wave pattern. The convection has been active for about 3 hours, giving a propagation speed of 51 m s^{-1}. The Brunt-Väisälä frequency on the 607 mb surface south of the storm region at 23/2200 is an almost constant $1.42 \times 10^{-2}\ s^{-1}$. Using these values in (6.7), the inverse vertical wave number m^{-1} = 3584 m, giving a value for H of 11.3 km. From Fig. 5.6a, the tropopause height in the southern end of the cross-section can be estimated from the PV gradient as about 11 km, which agrees very well with the computation of H above. The vertical motion depicted in Fig. 6.12 closely matches that along the heavy line in Fig. 6.11, with subsidence from about 300 km south to 565 km south, and a rapid shift to positive vertical motion north of the 300 km point.

The wave structure closer to the storm is perhaps due to higher wavenumber oscillations with slower propagation speeds. Mapes comments that the storm-averaged divergence vertical profiles from several different MCS observations showed significant higher wavenumber ($l > 3$) structure in the lower levels. Considering that the work of Mapes was highly idealized, with horizontally homogeneous initial conditions and no shear, topography or Coriolis force, the close agreement with this PE simulation of an MCS is remarkable.

6.6 The Rossby Radius Revisited

In the first part of chapter 2, a modified definition of the Rossby radius,

$$\lambda_R = \frac{C_N}{(\zeta + f)^{1/2}(2VR^{-1} + f)^{1/2}}$$

(Eq. 2.1) was introduced. Cotton et al. (1989) proposed this as a metric to determine the dynamic size (and implicitly, the relative state of balance) of an MCC.

From the above results, a Rossby radius for the first mode can be computed. The form of λ_R (2.1) reduces to the more familiar result (Gill 1982)

$$\lambda_R = C_N/f, \tag{6.11}$$

in the absence of significant relative vorticity. This form has the clear interpretation as the distance a wave would travel during the rotational timescale $1/f$. Using (6.11), $\lambda_R = 509$ km and 255 km for the first 2 modes respectively.

This would be a deformation radius appropriate to the large scale storm environment. Near the storm where the vorticity is significantly perturbed, λ_R would likely be smaller. As noted in Chapter 2, the application of (2.1) to an MCC is not straight forward. The results of the simulation presented in Chapter 5 indicated that an MCC has several important structures, each having a relevant length scale. The vorticity can also vary by several hundred percent, even in somewhat radially shaped features. Still, (2.1) may be applied, at least heuristically, with some guidance from the balanced analysis.

Several of the features within the MCC are clearly balanced. For example, the MCV in Fig. 6.2 which formed early in the storm has R = 100 km, and $\zeta = 1.5 \times 10^{-4}\ \mathrm{s}^{-1}$ as an average over the storm-relative circulation. Using $f = 1.0 \times 10^{-4}\ \mathrm{s}^{-1}$ and $V = 10\ \mathrm{m\ s}^{-1}$, $\lambda_R = 138$ km for the n =1 mode and $\lambda_R = 69$ km for the second mode[8]. This result is not surprising, being implied by the good agreement between $\mathbf{V}_m$ and $\mathbf{V}_b$ in Fig. 6.2. Conversely, the large upper-level anticyclone depicted in Fig. 6.9- has $\zeta < -f$. Therefore, λ_R, in the sense of (2.1), is undefined, a reasonable result in light of the fact that the region is inertially unstable.

8. In these calculations we have assumed that c_n as calculated for the large scale environment obtains. In fact, within the region of the vortex, the Brunt-Väisälä frequency, N, has been increased by about 30% over the surrounding environment. If we calculate the phase speed in this saturated region using the moist Brunt-Väisälä frequency, N_m in. (2.3), as done by Chen and Frank (1993), the resultant c_n is more or less that for the large scale.

Typical values for the mature storm as a whole, inferred from, say, Fig. 5.21 might be R = 250 km, $\zeta = 1.5 \times 10^{-4}\ s^{-1}$, $f = 1.0 \times 10^{-4}\ s^{-1}$, $V = 15\ m\ s^{-1}$. Assuming the phase speeds above are appropriate, $\lambda_R = 214$ km for the gravest mode and $\lambda_R = 107$ km for the second vertical mode. The circulations attributable to the MCC certainly exceed 200 km in scale. This analysis would also suggest that vertical modes greater than n = 1 would be strongly modified before they could propagate away from the storm, while the first mode would radiate a significant amount of energy well away from the MCC. These λ_R calculations, while imprecise, further support the conclusion that the MCC in this study is, to a large extent, a balanced system.

Chapter 7: Summary and Conclusions

7.1 Introduction and Review

In Chapter 1, the MCC was shown to be a phenomenon occuring worldwide, though preferentially in certain locations. These favored locations frequently provide a large-scale environment apparently conducive to MCC formation, though case studies reveal that a wide spectrum of atmospheric conditions can produce MCCs and MCSs. MCCs, by definition, share certain structural and temporal features. Beyond the definition criteria, however, MCCs typically show a common organizational structure and evolution which cannot be directly attributed to the environment in which they evolve. This suggests that their evolution is governed by a set of physical laws which apply similarly to ensemble convective heating in a variety of mesoscale environments.

Much of what is considered "meteorologically significant" atmospheric motion can be described by a subset of the primitive equations, generically termed "balanced models". These balanced models, while several in number and of varying complexity and completeness, have a common defining attribute. They neglect "fast manifold" behavior; those atmospheric motions, typified by gravity and acoustic waves, which have short timescales and often exhibit oscillatory behavior. While this fast manifold behavior is ubiquitous, it generally represents transient responses to changes in the energetic balance of the atmosphere. The more permanent, "slow-manifold" atmospheric motions tend to be vortical in nature, especially if their environment is rotating.

In the middle latitudes, MCCs represent the extreme case of a large-amplitude energetic perturbation to the background environment. While substantial transients are expected (and observed), a separate class of non-radiating, balanced motions also evolve. These motions, and the altered thermal structure which balances them, are conveniently contained in a single quantity, the PV.

In Chapter 3, a balanced model, the NLB equation set, was described. This model can be used to invert the PV and recover the rotational component of the balanced motion and the balanced mass field. A further application of the NLB approximation, along with the vertical vorticity equation and the thermodynamic equation, resulted in a diagnostic equation for the vertical velocity, and, as well, a method for diagnosing the horizontal divergent motions which are "slaved" to it by the constraint of continuity.

In Chapter 5 a PE simulation of an observed MCC was discussed. This simulation agreed well with surface, upper-air and satellite observations and ground-based radar plots. It produced many of the features frequently associated with MCCs: A leading line of vigorous convection, a trailing region of less intense stratiform rainfall, mesoscale convectively-induced vortices in the lower troposphere, a descending rear-to-front flow, and a large anticyclone at upper levels.

The intent of the PE simulation was to provide a well-resolved data set, typical of that which might be observed in an MCC in nature. This simulation, by nature of the PE model, contained both the transient, fast-manifold and slow-manifold responses to the convective heating. The balanced diagnostic method described in Chapters 3 and 4 was used in Chapter 6 to analyze the simulation and separate its balanced and unbalanced flows.

7.2 Conclusions

The work in Chapter 6 was an attempt to answer the question:

Does the MCC represent a balanced fluid-dynamical system?

The answer to that question is, to a large extent, *yes*, at least for this case. The nondivergent component of the PE model winds was found to consist, to a great degree, of balanced flow, $\mathbf{V}_{b\psi}$. Further, this was not a state which was achieved after some period of adjustment. Rather, the nondivergent winds, throughout the MCC lifetime, from initial convection to dissipation, remained in a nearly balanced state. This almost "instantaneous adjustment" was also observed by Davis and Weisman (1994) in their balanced diagnosis of an idealized squall line and associated MCV. This is related to the fact that the rapidly-evolving curved flow in the PE simulation is to first order, a response to the pressure-gradient force (i.e. a generalized cyclostrophic balance). This balance is contained within the NLB system and the PV field.

Perhaps more surprisingly, the storm-induced divergent model winds also remained balanced to a good degree, though certainly less so than the nondivergent flow. The analysis in Section 6.4.1 showed that during the MCC life-cycle, $\mathbf{V}_{u\chi}$ increased considerably from preconvective values, gradually decreasing after cessation of convection.

Gravity waves, induced by the intense heating, consist almost entirely of divergent flow which is, by definition, unbalanced. The good agreement between model and balanced upward vertical mass flux, together with the periodic wave-like appearance of ω_u and $\mathbf{V}_{u\chi}$ and the known filtering characteristics of the balance model, suggests that the bulk of the three-dimensional unbalanced divergent motion may be attributed to gravity waves.

Within the averaging volume, the greatest disparity between the model and balanced circulations was found in the downward vertical motion. Both ϕ_{b-} and ϕ_{m-}, the integrated downward mass fluxes, were considerably smaller than their upwards counterparts, indicating that the compensating subsidence for both ϕ_{b+} and ϕ_{m+} occurred over an area much greater than the averaging volume.

The magnitude of ϕ_{b-} grew and dwindled in proportion to the areal extent of the precipitating cloud. The balanced downdrafts correlated well with the locations of evaporative diabatic cooling, dissipating as the precipitation, and hence evaporative cooling, ceased. These factors indicate that, for this situation, diabatic cooling was the primary mechanism forcing *localized* downward motion in the balanced ω equation. As expected from balanced model theory, a more general, almost domain-wide, subsidence was superimposed on these localized mid-level downdrafts. For most of the storm lifetime, the base of the precipitating cloud was largely below the averaging level. This would locally result in the net upward mass flux for the diabatically-dominated ω_b seen within the averaging domain.

The downward mass flux in the PE model exceeded ϕ_{b-} by a factor of 2 at almost all times during the lifetime of the simulated MCC. This indicates that the process of mass adjustment due to convective heating is largely dominated by unbalanced fast-manifold processes, such as gravity waves, a theory supported by recent research on the convective adjustment process. This transient process, not captured in the balance system, is probably important in generating new convection.

Several of the features, such as the MCV and RIJ, seen in the MCC simulation were found to be comprised largely of $\mathbf{V}_{b\psi}$. This agrees with other recent work investigating balanced flows in MCSs. The poorest agreement between $\mathbf{V}_{b\psi}$ and $\mathbf{V}_{m\psi}$ was found in the upper-level anticyclone, in the outflow region of the storm. This region, dominated by a thin, but widespread, sheet of negative PV, was inertially unstable. The balanced model would not be expected to perform well there, given the constraints placed on it. $\mathbf{V}_{m\chi}$ and $\mathbf{V}_{b\chi}$ were also inconsistent, with a significant component of unbalanced horizontal advection occurring there.

The RIJ was another location which showed a small, but significant, component of $\mathbf{V}_{u\psi}$. The reasons for this are not well understood, but it is hypothesized that local inertial instability may be involved.

The balanced analysis was found to be a good filter of gravity waves. Removal from ω_m of the balanced vertical motion directly forced by diabatic effects revealed a residual ω_u of highly periodic nature. Inspection of the unbalanced vertical motion fields at early times in the storm clearly revealed a radially-symmetric wave pattern. As the storm matured, the structure of ω_u became quite complex.

The relatively simple unbalanced wave structure excited during genesis of the MCC was found to agree well with current research investigating mass adjustment to heating profiles typical of MCSs. The ω_u and divergence fields showed strong evidence of the predicted domination by vertical waves 1 and 2.

Using the phase speeds obtained in the gravity-wave analysis, the Rossby radii for these 2 lowest-order modes were calculated from both the more standard formula of (6.11) for the large-scale environment and the modified definition of (2.1) for the local, storm-perturbed region. This analysis revealed that the MCV within the storm was larger than λ_R for all vertical waves with n > 2. The λ_R for the mature storm as an ensemble also predicted a good degree of balance with $\lambda_R^{n=1}$ scaling similarly to the MCC. The Rossby radius computed for the large-scale, unperturbed environment, which might be the appropriate metric for the genesis period of the MCC, found that $\lambda_R^{n=1}$ and $\lambda_R^{n=2}$ were both larger than the nascent storm. At this time, a considerable amount of energy would be lost from the storm-scale circulations by radiation of gravity waves.

7.3 Future Work

It is often tempting to overgeneralize the results of a particular case study. To determine the applicability of the results presented above to MCCs in general, and other MCSs, it would be useful to apply the balanced analysis used in this dissertation to other MCC simulations. In particular it would be illuminating to analyze storms developing in differing environments and at different latitudes.

This study focused on the motion-related aspects of MCCs and balance. A wealth of information can also be obtained from a detailed analysis and comparison of the balanced and model potential temperature and geopotential fields. This would help clarify some of the more poorly understood aspects of adjustment to balance.

The role that inertial instability played in the evolution of this PE simulation is not clear. Further analysis of the PE model results may clarify some of the effects that inertial instability and associated conditional symmetric instability (CSI) may have had in the amplification and/or dissipation of the RIJ.

The technique of piecewise potential vorticity inversion discussed in Davis and Emanuel (1991) and Davis (1992) could be used to determine the relative importance and radius-of-influence attributable to the individual pieces of the convectively-induced PV structure. This approach would be useful to determine dynamic importance of the thin, yet horizontally large, negative anomaly near the tropopause.

It also be interesting to extend the PE simulation and balanced analysis for another several hours. This would allow transient fast-manifold effects to decay further and would shed some light on the part balanced dynamics play in the compensating subsidence process.

The results found in this study present a picture of the "signature" an MCC leaves in its environment after the decay of transients. This information is useful in parameterizing the effects of MCCs and MCSs as sub-grid scale phenomena in general circulation and climate models.

References

Allen, J. S., 1991: Balance equations based on momentum equations with global invariants of potential enstrophy and energy. *J. Phys. Oceanogr.*, **21**, 265-276.

Anthes, R. A., Y.-H. Kuo, S. G. Benjamin, and Y.-F. Lin, 1982: The evolution of the mesoscale environment of severe local storms: Preliminary modeling results. *Mon. Wea. Rev.*, **110**, 1187-1213.

Anthes, R. A. and T. N. Carlson, 1983: Conceptual and numerical models of the evolution of the environment of severe local storms. *Proceedings of the First Sino-American Workshop on Mountain Meteorology.* E.R. Reiter, ed., Science Press, Boston.

Arakawa, A and W. H. Schubert, 1974: Interaction of a cumulus cloud ensemble with the large-scale environment, Part 1. *J. Atmos. Sci.*, **31**, 674-201.

Arfken, G. B., 1985: *Mathematical Methods for Physicists.* Academic Press, Orlando, 985 pp.

Augustine, J. A. and K. W. Howard, 1988: Mesoscale convective complexes over the United States during 1985. *Mon. Wea. Rev.*, **116**, 685-701.

Augustine, J. A. and K. W. Howard, 1991: Mesoscale convective complexes over the United States during 1986 and 1987. *Mon. Wea. Rev.*, **119**, 911-919.

Baer, F., 1977: Adjustment of initial conditions required to suppress gravity oscillations in nonlinear flows. *Beitr. Phys. Atmos.*, **50**, 350-366.

Baer, F. and J. J. Tribbia, 1977: On complete filtering of gravity modes through nonlinear initialization. *Mon. Wea. Rev.*, **105**, 1536-1539.

Bartels , D. L. and R. A. Maddox, 1991: Midlevel cyclonic vortices generated by mesoscale convective systems. *Mon. Wea. Rev.*, **119**, 104-118.

Bernstein, B. C. and R. H. Johnson, 1994: A dual-doppler study of an OK-PRESTORM heat burst event. *Mon. Wea. Rev.*, **122**, 259-273.

Biggerstaff, M. I., and R. A. Houze, Jr, 1991a: Kinematic snd precipitation structure of the 10-11 June 1985 squall line. *Mon. Wea. Rev.*, **119**, 3034-3065.

Biggerstaff, M. I., and R. A. Houze, Jr, 1991b: Midlevel vorticity structure of the 10-11 June 1985 squall line. *Mon. Wea. Rev.*, **119**, 3066-3078.

Blackadar, A. K., 1957, Boundary layer wind maxima and their significance for the growth of nocturnal inversions. *Bull.. Amer. Meteor. Soc.*, **38**, 282-290.

Bleeker, W., and M.J. Andre, 1951: On the diurnal variation of precipitation, particularly over the central U.S.A., and its relation to large-scale orographic circulation systems. *Quart. J. Roy. Meteor. Soc.*, **77**, 260-271.

Bosart, L. F., and F. Sanders, 1981: The Johnstown flood of July 1977. A long-lived convective storm. *J. Atmos. Sci.*, **38**, 1616-1642.

Brandes, E. A., 1981: Fine structure of the Del City -Edmond tornadic mesocirculation. *Mon. Wea. Rev.*, **109**, 635-647.

Brandes, E. A. 1984: Vertical vorticity generation and mesocyclone sustenance in tornadic thunderstorms: The observational evidence. *Mon. Wea. Rev.* **112**, 2253-2269.

Brandes, E. A. 1990: Evolution and structure of the 6-7 May 1985 mesoscale convective system and associated vortex. *Mon. Wea. Rev.*, **118**, 109-127.

Brandes, E. A. and C. L. Ziegler, 1993: Mesoscale downdraft influences on vertical vorticity in a mature convective system. *Mon. Wea. Rev.*, **121**, 1337-1353.

Bretherton , C. S., and P. K. Smolarkiewicz, 1989: Gravity waves, compensating subsidence, and detrainment around cumulus clouds. *J. Atmos. Sci.* , **46**, 740-759.

Bretherton, C. S., and C. Schär, 1993: Flux of potential vorticity substance : A simple derivation and a uniquencess property. *J. Atmos. Sci.*, **50**, 1834-1836.

Brody, F. C., 1987: An excessive rainfall event caused by the interaction of a convectively-induced upper-level vort. max., a front, and an outflow boundary. *Nat. Wea. Dig.* **11**, 37-41.

Burden, R. L., D. J. Faires, and A. C. Reynolds, 1981: *Numerical Analysis*. Prindle, Weber & Schmidt, Boston, 598 pp.

Burgess, D. W., and B. F. Smull, 1990: Doppler radar observations of a bow echo associated with a long-track severe windstorm. Preprints, *16th Conf. on Severe Local Storms*, Kananaskis Park, Alberta, Canada, Amer. Meteor. Soc. 203-208.

Charney, J. G., 1948: On the scale of atrmospheric motions. *Geofys. Publ.*, **17**, No 2, 1-17.

Charney, J. G., 1955: The use of primitive equations of motion in numerical prediction. *Tellus*, **7**, 22-26.

Charney, J. G., 1962: Integration of the primative and balance equations. *Proc. Symp. Numerical Weather Prediction*, Tokyo, 131-152.

Charney, J. G. and M. F. Stern, 1962: On the stability of internal baroclinic jets in a rotating atmosphere., *J. Atmos. Sci.* **19**, 159-172.

Chen, S. S., and W. M. Frank, 1993: A numerical study of the genesis of extratropical convective mesovortices. Part I: Evolution and dynamics. *J. Atmos. Sci.*, **50**, 2401-2426.

Chen, S., and W. R. Cotton, 1988: The sensitivity of a simulated extratropical mesoscale convective system to longwave radiation and ice-phase microphysics. *J. Atmos. Sci.*, **45**, 3897-3910.

Cotton, W. R., R. L. George, P. J. Wetzel, and R. L. McAnelly, 1983: A long-lived mesoscale convective complex,. Part I: the mountain-generated component. *Mon. Wea. Rev.*, **111**, 1893-1918.

Cotton, W. R., and R. A. Anthes, 1989: *Storm and Cloud Dynamics.*, Academic Press, New York, 880 pp.

Cotton,W. R., M.-S. Lin, R. L. McAnelly, and C. J. Tremback, 1989: A composite model of mesoscale convective complexes. *Mon. Wea. Rev.* **117**, 765-783.

Daley, R., 1980: On the optimal specification of the initial state for deterministic forecasting. *Mon. Wea. Rev.*, **108**, 1719-1735.

Danielsen, E. F., 1990: In defense of Ertel's potential vorticity and its general applicibility as a meteorological tracer. *J. Atmos. Sci.*, **47**, 2103-2020.

Danielsen, E. F., R. S. Hipskind, S. E. Gaines, G. W. Sachse, G. L. Gregory, and G. F. Hill, 1987: Three-dimensional analysis of potential vorticity associated with tropopause folds and observed variations of ozone and carbon monoxide. *J. Geophys. Res.*, **92**, 2103-2111.

Davis, C. A., and K. A. Emanuel, 1991: Potential vorticity diagnostics of cyclogenesis. *Mon. Wea. Rev.*, **119**, 1929-1953.

Davis, C. A., 1992: Piecewise potential vorticity inversion. *J. Atmos. Sci.* **49**, 1397-1411.

Davis, C. A., M. L. Weisman, B. Skamarock, J. Klemp, 1993: Balanced dynamics of simulated long-lived mesoscale convective systems. Preprints, *Ninth Conference on Atmospheric and Oceanic Waves and Stability,* San Antonio, Amer. Meteor. Soc.

Davis, C. A. and M. L. Weisman, 1994: Balanced dynamics of mesoscale vortices in simulated convective systems. *J. Atmos. Sci.*, **15**, 2005-2030.

Durran, D. R. and J. B. Klemp, 1982: On the effects of moisture on the Brunt-Väisälä frequency. *J. Atmos. Sci.*, **39**, 2152-2158.

Eady, T. E., 1949: Long waves and cyclone waves. *Tellus*, **1**, 33-52.

Eliassen, A., 1949: The quasi-steady equations of motion. *Geophys. Publ.*, **17**, 1-44.

Emanuel, K. A, 1979: Inertial instability and mesoscale convective systems. Part 1: Linear theory of inertial instability in rotating viscous fluids. *J. Atmos. Sci.*, **36**, 2425-2449.

Emanuel, K. A., 1982: Inertial instability and mesoscale convective systems. Part II: Symmetric CISK and baroclinic flow. *J. Atmos. Sci.*, **39**, 1080-1097.

Emanuel, K. A., 1983: Elementary aspects of the interaction between cumulus convection and the large-scale environment. *Mesoscale Meteorology: Theories, Observation and Models*, D. K. Lilly and T. Gal-Chen, Eds., D. Riedel, 551-575.

Emanuel, K., 1986: An air-sea interaction theory for tropical cyclones. Part I: Steady-state maintenance. *J. Atmos. Sci.*, **43**, 585-604.

Ertel, H., 1942: Ein neuer hydrodynamischer Wirbelsatz. *Meteor. Z.*, **59**, 277-281

Fjørtoft, R., 1962: On the integration of a system of geostrophically balanced prognostic equations. *Proc. Int. Symp. Numerical Weather Prediction*, Tokyo, Meteor. Soc. Japan, 153-159.

Fortune, M. A., W. R. Cotton, and R. L. McAnelly, 1992: Frontal-wave-like evolution in some Mesoscale Convective Complexes. **120**, 1279-1300.

Frank, W. M., 1983: The cumulus parameterization problem. *Mon. Wea. Rev.*, **111**, 1859-1871.

Fritsch, J. M., and C. F. Chappell, 1980: Numerical prediction of convectively driven mesoscale pressure systems. Part 1: A cumulus parameterization. *J. Atmos. Sci.* **44**, 3787-3799.

Fritsch, J. M., J. D. Murphy, and J. S. Kain, 1994: Warm-core vortex amplification over land. *J. Atmos. Sci.* (in press).

Fujita, T. T., 1971: Proposed Characterization of tornadoes and hurricanes by area and intensity. SMRP Res. Paper No. 91, Department of Geophysical Sciences, University of Chicago.

Fujita, T. T., 1978: Manual of Downburst Identification for Project Nimrod. Satellite and Mesometeorology Research Paper No. 156, Department of Geophysical Sciences, University of Chicago, 104 pp.

Gallus, W. A. Jr, and R. H. Johnson, 1991: Heat and Moisture budgets of an intense midlatitude squall line. *Mon. Wea. Rev.*, **48**, 122-146.

Gamache, J, F. and R. A. Houze, Jr, 1982: Mesoscale motions associated with a tropical squall line. *Mon. Wea. Rev.*, **110**, 118-135.

Gamache, J, F. and R. A. Houze, Jr, 1985: Further analysis of the composite wind and thermodynamic structure of the 12 September GATE squall line. *Mon. Wea. Rev.*, **113**, 1241-1259.

Gent, P. R., and J. C. McWilliams, 1983: Consistent Balanced models in bounded and periodic domains. *Dyn. Atmos. Oceans*, **7**, 67-93.

Gent, P. R., J. C. McWilliams, and C. Snyder, 1994: Scaling analysis of curved fronts: Validity of the balance equations and semi-geostrophy. *J. Atmos. Sci.*, **51**, 160-163.

Gill, A. E., 1982: *Atmosphere-Ocean Dynamics*. Academic Press, New York, 662 pp.

Goldstein, H., 1950: *Classical Mechanics*. Addison-Wesley Publ. Co. Reading, MA., 399 pp.

Gossard, E. E., and W. H. Hook, 1975: *Waves in the Atmosphere*. Elsevier Scientific Publishing Company. Amsterdam, 456 pp.

Gray, W. M. and C. W. Landsea, 1992: African rainfall as a precursor of hurricane-related destruction on the U.S. East Coast. *Bull. Amer. Meteor. Soc.* **73**, 1352-1364.

Haltiner, G. J., and R. T. Williams, 1980: *Numerical Prediction and Dynamic Meteorology*. 2nd ed. Wiley and Sons, 477 pp.

Haynes, P. H., and M. E. McIntyre, 1987: On the evolution of vorticity and potential vorticity in the presence of diabatic heating and frictional or other forces. *J. Atmos. Sci.*, **44**, 828-841.

Haynes, P. H., and M. E. McIntyre, 1990: On the conservation and impermeability theorems for potential vorticity. *J. Atmos. Sci.*, **47**, 2021-2030.

Hertenstein, R. F. A. and W. H. Schubert, 1991: Potential vorticity anomalies associated with squall lines., **119**, *J. Atmos. Sci.*, 1663-1672.

Holton, J. R., 1992: *An Introduction to Dynamic Meteorology*. Academic Press, New York, 507 pp.

Hoskins, B. J., 1975: The geostrophic momentum approximation and the semi-geostrophic equations. *J. Atmos. Sci.*, **32**, 233-242.

Hoskins, B. J., 1990: Theory of extratropical cyclones. *Extratropical Cyclones: The Eric Palmén Memorial Volume*, C. Newton and E Holopainen, Eds. Amer. Meteor. Soc., 63-80.

Hoskins, B. J., and I. Draghici, 1977: The forcing of ageostrophic motion according to the semi-geostrophic equations and in an isentropic coordinate model. *J. Atmos. Sci.*, **34**, 1859-1867.

Hoskins, B. J., I. Draghici and H. C. Davies, 1978: A new look at the ω-equation. *Quart. J. Roy. Meteor. Soc.*, **104**, 31-38.

Hoskins, B. J. , M. E. McIntyre, and A. W. Robertson, 1985: On the use and significance of isentropic potential vorticity maps. *Quart. J. Roy. Meteor. Soc.*, **111**, 877-946.

Houze, R. A. Jr., B. F. Smull, and P. Dodge, 1990: Mesoscale organization of springtime storms in Oklahoma. *Mon. Wea. Rev.*,**118**, 613-654.

Iversen, T., and T. E. Nordeng, 1984: A hiearchy of nonlinear filtered models-numerical solutions. *Mon. Wea. Rev.*, **112**, 2048-2059.

Jiang, H. and D. J. Raymond, 1994: Simulation of a mature mesoscale convective complex using a nonlinear balance model. (accepted for publication, *J. Atmos. Sci*).

Johns, R. H., and W. D. Hirt, 1987: Derechos: widespread convectively induced windstorms. *Wea. Forecasting*, **2**, 32-49.

Johnson, R. H., and P. J. Hamilton, 1988: The relationship of surface pressure features to the precipitation and airflow structure of an intense midlatitude squall line. *Mon. Wea. Rev.*, **116**, 1444-1472.

Johnson, R. H., S. Chen, and J. J. Toth, 1989: Circulations associated with a mature-to-decaying midlatitude mesoscale convective sytem. Part I: Surface features - heat bursts and mesolow development. *Mon. Wea. Rev.*, **117**, 945-959.

Johnson, R. H., W. A. Gallus, and M. D. Vescio, 1990: Near-tropopause verttical motion within the trailing stratiform region of a midlatitude squall line. *J. Atmos. Sci.*, **47**, 2200-2209.

Johnson, R. H., and D. L. Bartels, 1992: Circulations associated with a mature-to-decaying midlatitude mesoscale convective system. Part II: Upper level features. *Mon. Wea. Rev.*, **120**, 1301-1320.

Kane, R. J. Jr., C. R. Chelius and J. M. Fritsch, 1987: Precipitation characteristics of mesoscale convective systems. *J. Climate Appl. Meteor.*, **26**, 1345-1357.

Klemp, J. B. and R. Rotunno, 1983: A study of the tornadic region within a supercell thunderstorm. *J. Atmos. Sci.*, **40**, 359-377.

Kuo, H. L., 1965: On the formation and intensification of trropical cyclones through latent heat release by cumulus convection. *J. Atmos. Sci.*, **22**, 40-63.

Kuo, H. L., 1974: Further studies of the parameterization of hte influence of cumulus convection on large-scale flow. *J. Atmos. Sci.*, **31**, 1232-1240.

Laing, A.G. and J. M. Fritsch, 1993a: Mesoscale convective complexes over the Indian monsoon region. *J. Climate,* **6**, 911-919.

Laing, A.G. and J. M. Fritsch, 1993b: Mesoscale convective complexes in Africa. *Bull. Amer. Meteor. Soc.*, **121**, 2254-2263.

Lait, L. R., 1994: An alternative form for potential vorticity. *J. Atmos. Sci.*, **51**, 1754-1759.

Leary, C.A. and E. M. Rappaport, 1987: The lifecycle and internal structure of a midlatitude mesoscale convective complex. *Mon. Wea. Rev.* **115**, 1503-1527.

Leith, C. E., 1980: Nonlinear normal mode initilization and quasi-geostrophic theory. *J. Atmos. Sci.*, **37**, 958-968.

Lemon, L. R. and C. A. Doswell, 1979: Severe thunderstorm evolution and mesocyclone structure as related to cyclogenesis. *Mon. Wea. Rev.*, **107**, 1184-1197.

Lilly, D. K., 1983: Stratified turbulence and mesoscale variability of the atmosphere. *J. Atmos. Sci.*, **40**, 749-761.

Lorenz, E. D., 1960: Energy and numerical weather prediction. *Tellus*, **12**, 364-373.

Lorenz, E. D.,1986: On the existance of a slow manifold. *J. Atmos. Sci.*, **43**, 1547-1557.

Machenhauer, B., 1977: On the dynamics of gravity oscillations in a shallow water model, with application to normal mode initialization. *Beitr. Phys. Atmos.*, **50**, 253-271.

Maddox, R. A., 1980: Mesoscale convective complexes., *Bul. Amer. Meteor. Soc.*, **61**, 1374-1387.

Mapes, B. E., 1993: Gregarious tropical convection. *J. Atmos. Sci.*, **50**, 2026-2037.

McAnelly, R. L., and W. R. Cotton, 1986: Meso-β scale characteristics of an episode of meso-*a* scale convective complexes. *Mon. Wea. Rev.*, **114**, 1740-1770.

McAnelly, R. L., and W. R. Cotton, 1989: The precipitation lifecycle of mesoscale convective complexes over the central United States. *Mon. Wea. Rev.*, **117**, 784-808.

McBride, J. L. and R. Zehr, 1981: Observational analysis of tropical cyclone formation. Part II: Comparison of non-developing versus developing systems. *J. Atmos. Sci.*, **38**, 1132-1151.

McNider, R. T., and R. A. Pielke, 1981: Diurnal boundary-layer development over sloping terrain. *J. Atmos. Sci.*, **38**, 2198-2212.

McWilliams, J. C., and P. R. Gent, 1980: Intermediate models of planetary circulations in the atmosphere and ocean. *J. Atmos. Sci.*, **37**, 1657-1678.

McWillians, J. C., 1985: A uniformly valid model spanning the regimes of geostrophic and isotropic, stratified turbulence. *J. Atmos. Sci.*, **42**, 1773-1774.

Means, L. L., 1990: A study of the mean southerly wind maximum in low levels associated with a period of summer precipitation in the Middle West. *Bull. Amer. Meteor. Soc.*, **35**, 166-170.

Meitín, J. G., and J. B. Cunning, 1985: The Oklahoma-Kansas Preliminary Regional Exteriment for STORM-Central (OK-PRE-STORM), Volume 1. Daily operations summary. NOAA Tech. Memo. ERL ESG-20, Department of Commerce, Weather Research Program, Boulder, CO, 313 pp.

Menard, R. D., and J. M. Fritsch, 1989: A mesoscale convective complex-generated warm core vortex. *Mon. Wea. Rev.*, **117**, 1237-1261.

Merritt , J. H. and L. M. Fritsch, 1984: On the movement of the heavy precipitation areas of mid-latitude mesoscale convective complexes. Preprints. *Tenth Conference on Weather Analysis and Forecasting*. Amer. Meteor. Soc. , 529-536.

Miller, D. and J. M. Fritsch, 1991: Mesoscale convective complexes in the western Pacific region. *Mon. Wea. Rev.*,**119**, 2978-2992.

Moncrieff, M. W. and M. J. Miller, 1976: The dynamics and simulation of tropical cumulonimbus and squall lines. *Quart. J. Roy. Meteor. Soc.*, **102**, 373-394.

Montgomery, M. T., and B. F. Farrell, 1992: Polar low dynamics: *J. Atmos. Sci.*, **49**, 2484-2505.

Montgomery, M. T., and B. F. Farrell, 1993: Tropical cyclone formation. *J. Atmos. Sci.*, **50**, 285-310.

Nachamkin, J. E., R. L. McAnelly, and W. R. Cotton, 1994: An observational analysis of a developing mesoscale scale complex. *Mon. Wea. Rev.*, **122**, 1168-1188.

Nicholls, M.E., R. A. Pielke, and W. R. Cotton, 1991: Thermally forced gravity waves in an atmosphere at rest. *J. Atmos. Sci.*, **48**, 2561-2572.

Ogura, Y. , and Y.-L. Chen, 1977: A life history of an intense mesoscale convective storm in Oklahoma. *J. Atmos. Sci.*, **34**, 1458-1476.

Ogura, Y. , and M.-T. Liou, 1980: The structure of a midlatitude squall line: A case study. *J. Atmos. Sci.*, **37**, 553-567.

Olsson, P. Q. and W. R. Cotton, 1994: Diagnosis of balanced flow evolution in mesoscale convective systems using the nonlinear balance system. Preprints, *Sixth Conference on Mesoscale Processes.* Portland, Amer. Meteor. Soc.

Ooyama, K., 1982: Conceptual evolution of the theory and modeling of the tropical cyclone. *J. Meteor. Soc. Japan*, **60**, 369-380.

Pielke, R. A., 1984: *Mesoscale Meteorological Modeling.* Academic Press, New York, 612 pp.

Pielke, R. A., W. R. Cotton, R.L. Walko, C. J. Tremback, W. A. Lyons, L. D. Grasso, M. E. Nicholls, M. D. Moran, D. A. Wesley, T. J. Lee, and J. H. Copeland , 1992: A comprehensive meteorological modeling system-RAMS. *Meteorol. Atmos. Phys.* **49**, 69-91.

Pitchford, K. L., and J. London, 1962: The low-level jet as related to nocturnal thunderstorms over the midwest United States. *J. Appl. Meteor.*, **1**, 43-47.

Purdom, J. F. W., 1982: Subjective interpretation of geostationary satellite data for nowcasting. *Nowcasting*, K. Browning, Ed. Academic Press, 149-166.

Raymond, D. J. , 1983: Wave-CISK in mass flux form. *J. Atmos. Sci.*, **40**, 2561-2572.

Raymond, D. J. and H. Jiang, 1990: A theory for long-lived mesoscale convective systems. *J. Atmos. Sci.*, **47**, 3067-3077.

Raymond, D. J., 1992: Nonlinear balance and potential vorticity thinking at large Rossby number. *Quart. J. Roy. Meteor. Soc.*, **118**, 987-1015.

Reed, R. J., 1955: A study of a characteristic type of upper-level frontogenesis *J. Met.*, **12**, 226-237.

Reed, R. J. , and E. F. Danielsen, 1959: Fronts in the vicinity of the troposphere. *Arch. Met. Geophys. Biokl.*, **11**, 1-17.

Riehl, H. L., Cruz, M. and C. Muster, 1973: Precipitation characteristics during the Venezuela rainy season. *Quart. J. Roy. Meteor. Soc.*, **99**, 1117-1133.

Riley, J. J., R. W. Metcalf and M. A. Weissman, 1981: Direct numerical simulations of homogeneous turbulence in density-stratified fluids. *Proc. AIP Conf., No. 76, Nonlinear Properties of Internal Waves*, Bruce J. West, Ed., La Jolla, AIP 79-112.

Rossby, C. G., 1938: On the mutual adjustment of pressure and velocity distributions in certain simple current systems. *J. Marine Res.*, **1**, 15-27.

Rotunno, R., 1981: On the evolution of thunderstorm rotation. *J. Atmos. Sci.*, **109**, 577-586.

Rotunno, R. and J. B. Klemp, 1985: On the rotation and propagation of simulated supercell thunderstorms. *J. Atmos. Sci.*, **42**, 371-292.

Rotunno, R., and K. Emanuel, 1987: An air-sea interaction theory for tropical cyclones, part II: Evolutionary study using a nonhydrostatic axisymmetric numerical model. *J. Atmos. Sci.*, **45**, 463-485.

Schmidt, J. M., and W. R. Cotton, 1989: A High Plains squall line associated with severe surface winds. *J. Atmos. Sci.*, **46**, 281-302.

Schmidt, J. M., 1992: Numerical and observational investigations of long-lived, MCS-induced, severe surface wind events: The Derecho. Department of Atmospheric Science Paper No. 479. Colorado State Unviersity, Fort Collins, CO. 196 pp.

Schreiber, W. E., 1986: Case studies of thunderstorms initiated by radar-observed convergence lines. *Mon. Wea. Rev.*, **114**, 2256-2266.

Schubert, W. H. and B. T. Alworth, 1987: Evolution of potential vorticity in tropical cyclones. *Quart. J. Roy. Meteor. Soc.*, **113**, 147-162.

Schubert, W. H., J. J. Hack, P. L. SilvaDiaz, and S. R. Fulton, 1980: Geostrophic adjustment in an axisymmetric vortex. *J. Atmos. Sci.*, **37**, 1464-1484.

Schubert, W. H, and J. J. Hack, 1982: Inertial stability and tropical cyclone development. *J. Atmos. Sci.*, **39**, 1687-1697.

Schubert, W. H., S. R. Fulton, and R. F. A. Hertenstein, 1989: Balanced atmospheric response to squall lines. *J. Atmos. Sci.*, **46**, 2478-2483.

Shapiro, L. J., and M. T. Montgomery, 1993: A three-dimensional balance theory for rapidly rotating vortices. *J. Atmos. Sci*, **50**, 3322-3349.

Segal, M. and R. W. Arrit, 1992: Nonclassical mesoscale circulations caused by surface sensible heat-flux gradients. *Bull. Amer. Meteor. Soc.*, **73**, 1593-1603.

Sellers, W. D., 1965: *Physical Climatology*. University of Chicago Press, Chicago, 272 pp.

Skamarock, W. C., M. L. Weisman and J. B. Klemp, 1994: Three-dimensional evolution of simulated long-lived squall lines. *J. Atmos. Sci.*, **51**, 2563-2584

Smull, B. F., and R. A. Houze, Jr., 1985: A midlatitude squall line with a trailing region of stratiform rain. *Mon. Wea. Rev.*, **113**, 117-133.

Smull, B. F., and R. A. Houze, Jr., 1987a: Dual-Doppler radar analysis of a midlatitude squall line with a trailing region of stratiform rain. *J. Atmos. Sci.*, **44**, 2128-2148.

Smull, B. F., and R. A. Houze, Jr., 1987b: Rear inflow in squall lines with trailing stratiform precipitation. *Mon. Wea. Rev.*, **115**, 2869-2889.

Snyder, C., W. C. Skamarock, and R. Rotunno, 1991: A comparison of primative-equation and semigeostrophic simulations of baroclinic waves. *J. Atmos. Sci.*, **48**, 2179-2194.

Srivastava, R. C., T. J. Matejka and T. J. Lorello, 1986: Doppler radar study of the trailing anvil region associated with a squall line. *J. Atmos. Sci.*, **43**, 356-377.

Stensrud, D. J., and R. A. Maddox, 1988: Opposing mesoscale circulations: a case study. *Wea. Forecasting*, **3**, 189-204.

Stephens, G. L. and P. J. Webster, 1980: Tropical upper-tropospheric extended clouds: Inferences from MONEX. *J. Atmos. Sci.*, **37**, 1521-1541.

Tennekes, H., 1978: Turbulent flow in two and three dimensions. *Bull. Amer. Meteor. Soc.*, **59**, 22-28.

Thompson, P. D., 1983: A history of numerical weather prediction in the United States. *Bull. Amer. Meteor. Soc.*, **64**, 755-769.

Tollerud, E. I. and S. K. Esbensen, 1985: A composite life cycle of nonsquall mesoscale convective systems over the tropical ocean. Part I: Kinematic fields. *J. Atmos. Sci.*, **42**, 823-837.

Tremback, C. J. and R. Kessler, 1985: A surface temperature and moisture parameterization for use in mesoscale numerical models. Preprints, *7th AMS Conference on Numerical Weather Prediction*, June 17-20, Montreal, Quebec, Canada. Amer. Meteor. Soc.., 355-358.

Tripoli, G., and W. R. Cotton, 1989: A numerical study of an observed orogenic mesoscale convective system. Part II: Analysis of governing dynamics. *Mon. Wea. Rev.*, **117**, 301-324.

Vautard, R., and B. Legras, 1986: Invariant manifolds, quasi-geostrophy, and initialization. *J. Atmos. Sci.*, **43**, 565-584.

Velasco, I., and J.M. Fritsch, 1987: Mesoscale convective complexes in the Americas. *J. Geophys. Res.*, **92**, 9599-9613.

Wakimoto, R. M., 1985: Forecasting dry microburst activity over the High Plains. *Mon. Wea. Rev.*, **113**, 1131-1143.

Weisman, M. L., J. B. Klemp, and R. Rotunno, 1988: Structure and evolution of numerically simulated squall lines. *J. Atmos. Sci.*, **45**, 1990-2013.

Weisman, M. L., 1992: The role of convectively generated rear-inflow jets in the evolution of long-lived mesoconvective systems. *J. Atmos. Sci.*, **49**, 1826-1847.

Weisman, M. L., W. C. Skamarock, J. B. Klemp and C. Davis, 1992: THe generation of mesoscale convective vortices in the evolution of long-lived mesoscale convective systems. Preprints, *Ninth Conference on Atmospheric and Oceanic Waves and Stability,* San Antonio, Amer. Meteor. Soc. 234-237.

Weisman, M. L., 1993: The genesis of severe long-lived bow echoes. *J. Atmos. Sci.*, **50**, 645-670.

Weissbluth, M. J., and W. R. Cotton, 1993: The representation of convection in mesoscale models. Part I: Scheme fabrication and Calibration. *J. Atmos. Sci.*, **50**, 3852-3872.

Wetzel, P. J., W. R. Cotton, and R. L. McAnelly, 1983: A long-lived mesoscale convective complex, II, Evolution and structure of the mature complex. *Mon. Wea. Rev.*, **111**, 1919-1937.

Xu, Q., 1994: Semibalance model - Connection between geostrophic-type and balanced-type models., *J. Atmos. Sci.*, **51**, 953-970.

Yanai, M., S. Ebsbensen, and J. Chu, 1973: Determination of bulk properties of tropical cloud clusters from large-scale heat and moisture budgets. *J. Atmos. Sci.*, **36**, 53-72.

Zhang, D., L., and J. M. Fritsch, 1987: Numerical Simulation of a meso-β scale structure and evolution of the 1977 Johnstown Flood. Part II: Inertially stable warm-core vortex and the mesoscale convective complex. *J. Atmos. Sci.*, **44**, 2593-2612.

Zhang, D., L., and J. M. Fritsch, 1988: A numerical investigation of a convectively generated, inertially syable, extratropical warm-core mesovortex over land. Part I: Structure and evolution. *Mon. Wea. Rev.*, **116**, 2660-2687.

Zhang, D., L., K. Gao and D. B. Parsons, 1989: Numerical simulation of an intense squall line during 10-11 June 1985 PRE-STORM. Part 1: Model verification. *Mon. Wea. Rev.*, **117**, 960-994.

Zipser, E., J., 1982: Use of a conceptual model of the life-cycle of mesoscale convective systems to improve very-short-range forecasts. *Nowcasting*, Academic Press, New York. 191-204